Mathematical Model Selection for InSAR Deformation Time Series

O. Ku

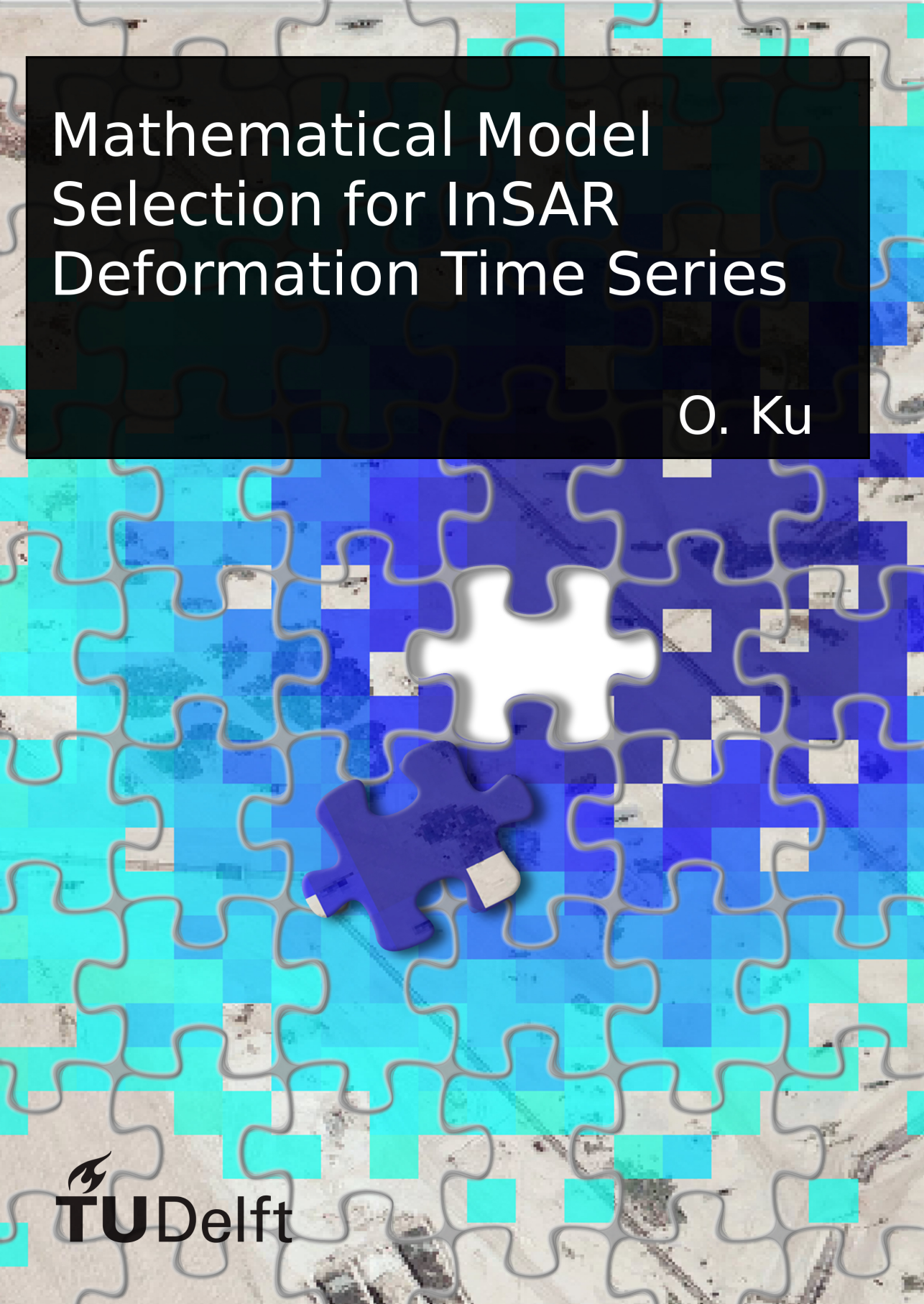

TU Delft

Mathematical Model Selection for InSAR Deformation Times Series

MSc. Geosciences and Remote Sensing
Thesis

Ou Ku

Supervisors:

Prof. dr. ir. R. F. Hanssen	Delft University of Technology, promotor
Dr. L. Chang	Delft University of Technology

Co-reader:

Dr. ir. F. C. Vossepoel	Delft University of Technology

Ou Ku
October, 2017
Department of Geosciences and Remote Sensing (GRS)
Faculty of Civil Engineering and Geosciences
Delft University of Technology

Keywords: Satellite Radar Interferometry, Spatio-temporal Deformation Modeling, Hydrocarbon Production

Preface

During my bachelor study in Central South University, Changsha, P. R. China, I was introduced to the satellite radar interferometry technique for the first time. Using this technique, one is able to measure the ground motion with millimeter precision from space, without any in-situ survey on the ground. The lectures given by Professor Z. Li inspired me to continue studying about this technique.

The MSc study at the Delft University of Technology (TUDelft) offered me a precious opportunity to be involved into the top-front of radar interferometry. I learned much from the talented and enthusiastic professors, colleagues and classmates here. I feel that I was trained in professional knowledge, but also the critical way of thinking, and the passion of exploring the unknown. All I have learned here resulted in this thesis, which I hope can contribute to the current radar interferometry technique.

I am very grateful for the support from many people and organizations during my study. I would like to thank my daily supervisor Ling Chang and my supervisor Ramon Hanssen, for their guidance and help. Ling spent countless hours on brainstorming the ideas with me, and even more time on reviewing the drafts. Without her help, this thesis would never have been possible. Ramon's knowledge and creativity continuously inspired me. I learned much from his critical but constructive feedback, and will always be grateful for that.

Furthermore, I would like to express my appreciation to the Climate Institute of TU Delft, who offered me a scholarship which supported the first two years of my MSc study.

The data used in the case study of the thesis are provided by SkyGeo. I would like to thank all my friends and colleagues at SkyGeo, with whom I had many interesting discussions. Special thanks to Hanno, Vincent, and Mehrdad, who helped me with my grammar; Quintus, who is always willing to offer his advice; Shaoqing, who gave me much encouragement.

I would like to thank all my friends from Delft Fellowship, with whom I spent many unforgettable days. It was such a blessing to meet all of you.

Thanks to my mom, for your support and love during my study in the Netherlands, and your understanding for my absence of long time.

Finally, thanks to Jingwen, who makes both the cover of this thesis as well as my life colorful.

Ou Ku
Delft, October 2017

Abstract

Satellite radar interferometry (InSAR) techniques can monitor the ground deformation with millimeter precision. With Time-series InSAR (TInSAR) methodology, the ground deformation time series can be derived from InSAR observations. One of the important ways to analyze the InSAR deformation time series is to parameterize the InSAR deformation time series with deformation models.

The previous ways of modelling InSAR deformation time series are usually point-wise, i.e. they focus on the deformation models of single InSAR measurement points. The deformation model of each point is either assumed to be a linear function of time, or is selected from the predefined alternative models. The point-wise modeling methodologies can well interpret the deformation behavior of each point, but is limited on modeling the spatial deformation patterns.

In this study, we design and implement methodologies to model the spatio-temporal deformation patterns, based on given spatial smoothness information of the deformation. We introduce a work flow to digest the spatial smoothness information from external sources, and use the information to improve the functional and stochastic model. We also propose a model selection methodology based on hypothesis testing to select the the most probable spatio-temporal deformation model from given potential models. The spatio-temporal deformation modeling methodology is applied to the simulated data, as well as the real InSAR measurements. We apply the spatio-temporal deformation methodology to study the deformation in a hydrocarbon production field in California, and successfully detect the instantaneous uplifting and subsiding events. Based on the simulation and real case study, we conclude that given proper contextual information, spatio-temporal deformation modeling is able to derive the deformation model in both temporal and spatial domain, and has a good performance on parameterizing the non-linear deformation behavior in the temporal domain.

Nomenclature

List of acronyms

BLUE	Best Linear Unbiased Estimation
DEM	Digital Elevation Model
DePSI	Delft implementation of Persistent Scatterer Interferometry
DIA	Detection, Identification and Adaption
DInSAR	Differential Interferometric SAR
DS	Distributed Scatterer
ERS	European Remote-Sensing Satellite
GNSS	Global Navigation Satellite System
GPS	Global Positioning System
LOS	Line-Of-Sight
LSE	Least Squares Estimation
MDV	Minimally Detectable Value
MHT	Multiple Hypothesis Testing
OMT	Overall Model Test
PS	Persistent Scatterer
PSI	Persistent Scatterer Interferometry
Radar	Radio Detection And Ranging
Radarsat	Canada's Radar Earth Observation Satellite
RMS	Root Mean Square
SAR	Synthetic Aperture Radar
SBAS	Small Baseline Subset Method
SLC	Single Look Complex
SRTM	Shuttle Radar Topography Mission
TerraSAR-X	German Radar Earth Observation Satellite
VCM	Variance Covariance Matrix

List of symbols

cm	Centimeter
km	Kilometer
m	Meter
mm	Millimeter
rad	Radian
yr	Year
A	Design matrix
B	Baseline
C	Complex phasor
$\mathbb{C}$	Cluster
D	Amplitude dispersion; Magnitude of outlier
d	Pseudo observations
$D\{\cdot\}$	Dispersion operator
$E\{\cdot\}$	Expectation operator
e	Residual between model and observation
$\mathscr{F}(\cdot)$	Fourier Transform operator
$\mathscr{F}^{-1}(\cdot)$	Inverse Fourier Transform operator
G	Design matrix of regualrization
H_0	Null hypothesis
H_j	An alternative hypothesis
m	Number of observations
n	Number of unknown parameters
o	Reference epoch
p	InSAR measurement point
Q	Variance-covariance matrix
q	Degree of freedom (dimension)
R	Number of ground targets
r	Reference point
$\mathbb{T}$	Ground target
T	Test statistics
$\mathbb{T}$	Test ratio
t_b	Epoch where breakpoints occur
t_s	Epoch where steps occur
t_ϵ	Epoch where outliers occur
v	Deformation velocity
$W\{\cdot\}$	Phase wrapping operator

x	Unknown parameters
$\underline{y}$	Observations
z	Variogram
α	Level of significance;
	Angle between two-satellite baseline and horizontal direction
β	Exponents of atmospheric magnitude
δv	Velocity change after a breakpoint
ϵ	Epoch where outlier occurs
γ	Power of test (discriminatory power)
λ	Wavelength of radar;
	Noncentrality parameter;
	Wavelength of atmospheric signal
μ	Non-linear deformation
σ	Standard deviation
Ψ	Unwrapped SLC phase
ψ	Wrapped SLC phase
ϕ^w	Wrapped interferometric phase
ϕ	Unwrapped interferometric phase
∇_{MDV}	Minimal detectable value
$\triangle$	Magnitude of step

Contents

1

Introduction

1.1. Motivation

Satellite radar interferometric techniques can provide deformation time series of ground targets. The deformation time series can be parameterized in order to detect the spatial and temporal pattern/change. In this work, we focus on the improvement of the parameterization of deformation time series, given relevant contextual knowledge.

1.2. Background

Satellite radar interferometric techniques (InSAR, Interferometric Synthetic Aperture Radar) has evolved into an important geodetic tool in the last few decades (Massonnet, 1994; Bamler and Hartl, 1998; Hanssen, 2001a). InSAR techniques do not require an in-situ survey and can monitor the ground deformation in all weather condition, with high spatial resolution, medium temporal resolution, in a large scale. It has been applied to measure various deformation phenomena of earth surface, such as earthquakes (Massonnet et al., 1993), groundwater flow (Amelung et al., 1999; Abidin et al., 2005), ice motion (Goldstein et al., 1993; Gray et al., 1999), and land slides (Rott et al., 1999) and so on.

The inherent limitations of InSAR technique is the decorrelation effect mainly caused by three factors (Hanssen, 2001a; van Leijen, 2014; Samiei Esfahany, 2017): 1) the disturbance of atmospheric noise (atmospheric decorrelation), 2) the change of ground scattering characteristics (temporal decorrelation), and 3) the different imaging geometries due to the satellite repeat orbits are too far apart (geometric decorrelation). These limitations have been overcome by the development of the time-series InSAR (TInSAR) methodologies, which use a stack of radar acquisitions of the same area. The typical methodologies of TInSAR are *Persistent Scatterer Interferometry* (PSI) method (Usai, 1997; Usai and Hanssen, 1997; Ferretti et al., 1999a, 2000c), the *Small BAseline Subset* (SBAS) method (Berardino et al., 2002; Mora et al., 2003), and hybrid methods (Lanari et al., 2004; Hooper, 2008; Ferretti et al., 2011). These approaches are based on assumptions regarding the spatial and/or temporal smoothness of the deformation signal, and derive the deformation time series based on InSAR phase observations.

1

The TInSAR methodologies have evolved in the last decade (Berardino et al., 2004; Ketelaar, 2009; Ferretti et al., 2011; van Leijen, 2014), and have been applied to study the deformation phenomena of a large variety of objects, for instance volcano region(Usai et al., 2003; Hooper et al., 2007; Papoutsis et al., 2013), earthquakes (Lanari et al., 2010), permafrost (Bell et al., 2008; Chen et al., 2012), oil/gas production activities (Ketelaar, 2009), flooding risk (Dixon et al., 2006), mining activities (Caro Cuenca et al., 2013), and civil infrastructures (Zeni et al., 2011; Chang et al., 2014). The ground deformation behavior is represented by the deformation time series of InSAR measurement points.

When interpreting the InSAR deformation time series, two basic components can be recognized: the component caused by the deformation phenomena, which is known as the *deformation signal*, and the component contributed by other effects, such as topographic residual or atmospheric residual, which is recognized as *noise*.

TInSAR methodologies provides deformation time series for all InSAR measurement points, on all observation epochs. However, interpreting the deformation time series point by point, epoch by epoch, may not always be an optimal way to study the deformation behavior based on InSAR deformation time series. Because 1) To numerically analyze the InSAR deformation time series, the parameterization is required. 2) The InSAR observation per epoch is not purely signal without any noise. Therefore interpreting InSAR deformation time series epoch by epoch may result into interpreting noise. 3) In case of a large volume of InSAR measurement points, point-wisely analyzing deformation time series may lead to a large computational effort. Due to 1), 2) and 3), we attempt to explore an efficient and systematic strategy to parameterize the InSAR deformation time series.

By applying parameterization, one assumes that the deformation signal of interest exists in the deformation time series, and follows a certain deformation model. All the differences between this deformation model and the deformation signal are interpreted as noise. The parameter(s) of the deformation model can be estimated from the deformation time series. Then the deformation behavior can be interpreted by the deformation model parameters. In this way, one does not need to interpret the deformation of all InSAR measurement points at all epochs.

A common way to parameterize the deformation time series is to assume that the deformation of every InSAR measurement point is a linear function of time, and estimate the deformation velocities for every point (Teunissen, 2003b, 2006; Caro Cuenca, 2012). However, for some points with a non-linear component in their deformation time series, the linear deformation model may misinterpret the non-linear deformation component as noise. To better parameterize their temporal behavior of a single InSAR measurement point, the *kinematic time series modeling* (i.e. deformation modeling) method has been proposed, which selects the optimal deformation model for an InSAR measurement point from the predefined most probable models (Chang and Hanssen, 2015;

Chang, 2015). The model selection is based on the theory of *multiple hypothesis testing* (Teunissen, 2000b). This method has been successfully applied on monitoring civil infrastructure (Chang et al., 2014; Chang, 2015).

In some cases, besides InSAR observations, one may also have apriori information on the spatial smoothness of deformation signal. This information is acquired from external sources,i.e. from *expert knowledge experience* or *extra observations*. They describes the spatial similarities of the deformation behavior of InSAR measurement points. For instance, one may know that several InSAR measurement points follow the same deformation model because they locate on the same building. This contextual information on spatial smoothness have not been properly utilized for deformation time series modeling, since the existing modeling methods, such as kinematic time series modeling, tend to model the deformation for each single InSAR measurement point. This thesis will focus on the improvement of the InSAR deformation time series modeling, given information on the spatial smoothness of deformation signal.

1.3. Problem statement

The kinematic time series modeling method has a good performance on modeling the deformation time series of a single InSAR measurement point. However, it is limited on taking into account the spatial smoothness between InSAR measurement points. This smoothness results into spatial correlation between InSAR measurement points.

The spatial correlation can be recognized from two aspects in InSAR deformation time series modeling. 1) From the stochastic model aspect, some certain types of noise in the InSAR measurements, e.g. atmospheric noise, are spatially correlated (Hanssen, 2001a; Samiei-Esfahany and Hanssen, 2013). When modeling the deformation time series per InSAR measurement point, the spatial correlation of noise cannot be specified by the stochastic model. 2) From the functional model aspect, the deformation behavior may show spatial correlation, e.g. in a deformation bowl, the variation of deformation velocity may follow a spatial model (Ketelaar, 2009). This spatial variation cannot be parameterized in the functional model, if the InSAR measurement points are treated to be independent.

As a result, when modeling InSAR deformation time series per InSAR measurement point, the apriori stochastic model will be defective, because of ignoring the spatially correlated noise, and the functional model will not be able to represent the spatial behavior of deformation. If the apriori knowledge on the spatial smoothness is not available, modeling deformation point by point will be the only option. However when correct information on the spatial smoothness is given, modeling the InSAR deformation time series per InSAR measurement point is no longer an optimal way to parameterize the deformation behavior. In this case, to extract reliable geometrical information from InSAR observations, the spatial smoothness information should be integrated.

1

1.4. Research objectives

In order to resolve the research problem mentioned in section 1.3, this study focuses on developing and demonstrating methodologies for deformation modeling, particularly in the spatial domain. The main research question is defined as:

How to optimally digest spatial smoothness information of the presumed deformation signal in the mathematical model, to estimate the spatio-temporal deformation of InSAR measurements points, and assess the quality of the results?

In the scope of this main question, three research questions are considered:

1. *What is the optimal functional model and stochastic model?*
   The first research question focuses on the parameterization of deformation time series of all InSAR measurement points. The functional model refers to the (linearized) spatio-temporal relationship between the deformation time series computed by TInSAR and the (unknown) deformation parameters. The stochastic model is expressed as a variance-covariance matrix (VCM), which describes the noise of the InSAR observations. To design the optimal functional and stochastic model, we use the Gauss-Markov model to describe the functional and stochastic relations (Gauss, 1809), and we use hypothesis testing to determine the optimal functional model.

2. *How to digest spatial smoothness information?*
   The estimation of the spatio-temporal deformation relies on the apriori information on the spatial smoothness of the deformation signal. We recognize the spatial similarities between InSAR measurement points based on the contextual information on the spatial smoothness of the deformation signal. The methodology of digesting contextual information will be developed in this study.

3. *How to assess quality of results?*
   The quality of the modeling results can be assessed from two aspects: 1) *Precision*, which represents the fit of deformation model to the InSAR data. 2) *Reliability*, which represents the imperfection of the chosen model.

1.5. Research limitations

This study will neither address any of the TInSAR data processing techniques (Berardino et al., 2004; Ferretti et al., 2011; Hooper, 2008; van Leijen, 2014; Samiei Esfahany, 2017), but rather focus on the post-processing techniques, using the output of the TInSAR processing chain. We will also not focus on improving the deformation modeling of every single InSAR measurement point (Chang, 2015; Chang and Hanssen, 2016), but a better model of the deformation behavior for the whole area of interest, taking into account the spatial smoothness information. The contextual information on the spatial smoothness

of InSAR measurements will be used to aid the spatio-temporal deformation modeling. However, this study will not focus on how to acquire contextual information, but focus on how to digest it when it is given, and import this information into deformation modeling.

1.6. Thesis roadmap

Chapter 2 gives a review of radar interferometry and the mathematical methodologies used in this study. The InSAR principle and the existing TInSAR methodologies will be introduced. Also, the linear model estimation method will be presented.

Chapter 3 focuses on the theory of *spatio-temporal deformation modeling*. We propose a modeling method to select the optimal spatio-temporal model for the deformation of the area of interest. We provide a generic way to introduce the spatial smoothness information into deformation modeling. The methodology of quality assessment is introduced.

Chapter 4 applies the spatio-temporal deformation modeling method to simulated data and assesses its performance, given different kinds of spatial smoothness information.

Chapter 5 applies the spatio-temporal deformation modeling method to real InSAR measurements, and analyzes the deformation over a hydrocarbon production area.

The conclusions, contributions, and recommendations for future research are presented in Chapter 6.

An overview of the road map of this thesis is shown in Fig. 1.1.

1

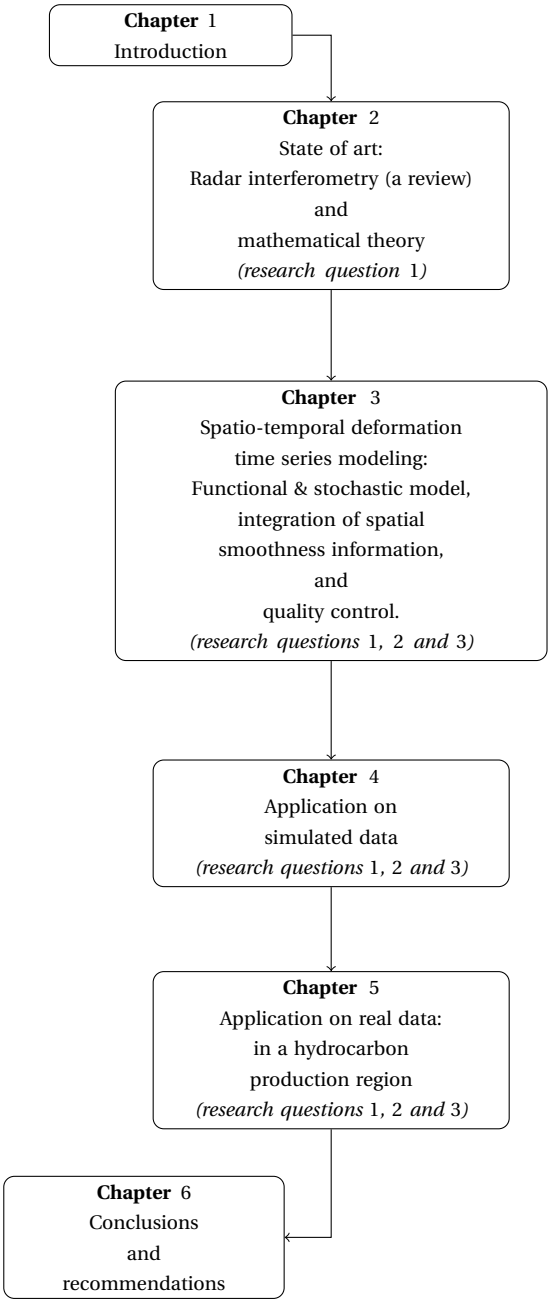

Figure 1.1: Thesis roadmap

2

State of the Art

This chapter introduces the background knowledge on radar interferometric techniques (InSAR), and basic estimation theory used in this study. Section 2.1.1 provides a brief review of InSAR, and particularly introduces time-series InSAR technique. Section 2.2 presents an introduction to the mathematical methodology used for deformation modeling.

2.1. SAR interferometry

SAR Interferometry (InSAR), including time-series InSAR (TInSAR) techniques, such as the Persistent Scatterer Interferometric (PSI) method (Ferretti et al., 2000c, 2001), the Small BAseline Subset (SBAS) method (Berardino et al., 2002) and the hybrid methods (Lanari et al., 2004; Hooper, 2008; Ferretti et al., 2011) are among the rapidly developing new technologies for Earth observation from space since the late 20th century. This section briefly introduces the InSAR principle in Section 2.1.1, and focuses on the TInSAR methodologies in Section 2.1.2.

2.1.1. InSAR principle

A radar image can be acquired by a side-looking radar sensor, which can be mounted on a ground based, airborne or spaceborne platform. The radar sensor transmits a radar signal/pulse to the ground objects, and measures the complex return of the backscattered pulses (See Fig. 2.1(a), adapted from Bamler and Hartl (1998)). A single complex return creates raw data, i.e. a so-called real aperture radar (RAR) image. Due to the limitation of the antenna (aperture) size, the RAR images usually have a very coarse resolution. Exploiting the fact that every ground target reflects many radar pulses during the sensor trajectory, the raw data are subsequently combined (or focused) by signal processing techniques in order to artificially build a long antenna and create a Synthetic Aperture Radar (SAR) image with much higher resolution (Bamler and Schättler, 1993; Cumming and Wong, 2005; Massonnet and Souyris, 2008).

Every pixel in a SAR image is associated with a resolution cell on Earth, sampled in the azimuth (i.e. flight direction) and slant-range coordinate system. Each pixel of an

2

SAR image records the signal information in the form of single-look complex (SLC). Together these pixels form an SLC image. The value of every pixel in an SLC can be expressed as a complex phasor C,

$$C = \mathrm{Re}(C) + j\,\mathrm{Im}(C) = A\exp(j\psi), \tag{2.1}$$

where j is the imaginary unit. $\mathrm{Re}(C)$ and $\mathrm{Im}(C)$ denote the real and imaginary parts of the complex phasor C. A represents the amplitude of C, which measures the magnitude of the radar reflection. ψ is the fractional phase of the received radar signal. The amplitude A can be computed by

$$A = \sqrt{\mathrm{Re}(C)^2 + \mathrm{Im}(C)^2}. \tag{2.2}$$

The SLC phase ψ mainly has four components,

$$\psi = W\{\Psi^{\mathrm{range}} + \Psi^{\mathrm{atmo}} + \Psi^{\mathrm{scat}} + \Psi^{\mathrm{noise}}\}, \tag{2.3}$$

where $W\{\cdot\}$ is the modulo-2π wrapping operator, and ψ is the wrapped SLC phase. Ψ^{range} is the range-dependent phase. The "range" refers to the distance between the radar sensor and the effective phase center of the resolution cell on the ground. Ψ^{atmo} is the phase delay caused by atmosphere. Ψ^{scat} is the scattering phase that is related to the distribution of all scatterers within a resolution cell. Ψ^{noise} is the noise-related phase, caused by system or thermal noise which is dependent on sensor specifications.

Interferometric SAR (InSAR) exploits the phase differences between two SLC (SAR) images to get the information about the position or the displacement of the ground objects. The interferometric process refers to the complex conjugate multiplication between two SLC images. It results into a complex image, known as an *interferogram*. To create an interferogram, one of the two SLCs (slave image) will be coregistered to the other SLC (master image). If C^{master} and C^{slave} are a pair of coregistered master and slave SLC, the interferogram I_{MS} can be computed by

$$I_{\mathrm{MS}} = C^{\mathrm{master}}(C^{\mathrm{slave}})^* = A^{\mathrm{master}}A^{\mathrm{slave}}\exp j(W\{\psi^{\mathrm{master}} - \psi^{\mathrm{slave}}\}), \tag{2.4}$$

where A^{master} and A^{slave} are the amplitude of the master and the slave SLC, respectively. The operator * denotes the complex conjugate. ψ^{master} and ψ^{slave} are respectively the SLC phase of the master and slave image. Considering Eq. (2.3), the interferometric phase of a pixel in the interferogram can also be written as the summation of the same four components

$$\phi^{w}_{\mathrm{intf}} = W\{\psi^{\mathrm{master}} - \psi^{\mathrm{slave}}\} = W\{\phi^{\mathrm{range}} + \phi^{\mathrm{atmo}} + \phi^{\mathrm{scat}} + \phi^{\mathrm{noise}}\}, \tag{2.5}$$

where ϕ^{w}_{intf} is the wrapped interferometric phase. The four unwrapped components, i.e. ϕ^{range}, ϕ^{atmo}, ϕ^{scatter} and ϕ^{noise}, are contributed by the differences of four components in the master and the slave, i.e. the range, atmospheric delay, scattering phase, and interferometric noise component, respectively

The atmospheric phase ϕ^{atmo} is the result of the difference between the atmospheric phase components in master and slave acquisitions. It has been studied by Goldstein (1995); Zebker et al. (1997); Massonnet and Feigl (1998); Hanssen (2001a); Ding et al. (2008) and Liu (2012).

The scattering phase ϕ^{scatter} is induced by the difference in scattering phase between the master and slave acquisitions. This difference degrades the interferometric coherence, known as *decorrelation*. It has been studied by Zebker and Villasenor (1992); Hanssen (2001a).

The interferometric noise phase ϕ^{noise} is due to different noise contributions comes from the system thermal noise and processing-induced noise (Samiei Esfahany, 2017).

When monitoring ground deformation using InSAR, one wants to extract deformation component from InSAR observation. The deformation is related to the ground target moving away/toward the satellite between the master and slave acquisition. This movement is one of the contributions to the change of slant-range. Therefore the deformation should be derived from ϕ^{range}, and the other components in ϕ^{w}_{intf} will be considered as noise. The phase component ϕ^{range} can be further decomposed into three components: 1) the flat earth phase ϕ^{flat}, the topographic phase ϕ^{topo} and the deformation phase ϕ^{defo}. ϕ^{range} can be written into the summation of the three components, as (Hanssen, 2001a; Samiei Esfahany, 2017)

$$\phi^{\text{range}} = \phi^{\text{flat}} + \phi^{\text{topo}} + \phi^{\text{defo}}. \tag{2.6}$$

To derive the deformation component ϕ^{defo} from ϕ^{range}, we investigate InSAR imaging geometry as shown in Fig. 2.1(b), which is adapted from Bamler and Hartl (1998).

As shown in Fig. 2.1(b), in a repeat-pass InSAR imaging, the SAR sensor at height H_{sat} acquires the master and slave from different positions in space and at different times, forming a spatial baseline B, which can be decomposed into two orthogonal components: 1) $B_{\parallel}$ in the satellite's line of sight (LOS) direction, which represents the parallel baseline, and 2) $B_{\perp}$ in the orthogonal direction of the LOS direction, which represents the perpendicular baseline. The baseline orientation angle α is the angle between B and the horizontal plane. Satellite radar looks at ground surface with a looking angle θ, and θ_{inc} is the incidence angle of radar signal w.r.t. the reference ellipsoid surface. The ground object has an elevation of H w.r.t. the reference ellipsoid. Three components of range-dependent phase ϕ^{range} can be computed:

- **Flat earth phase ϕ^{flat}**: This phase component is the effect of a reference surface, and exclusively depends on the viewing geometry. It can be approximated based on the so-called far-field approximation (Zebker and Goldstein, 1986; Hanssen, 2001a), as:

  $$\phi^{\text{flat}} = \frac{4\pi}{\lambda} B_{\parallel} = \frac{4\pi}{\lambda} B \sin(\theta - \alpha), \tag{2.7}$$

  where λ is the wavelength of radar signal.

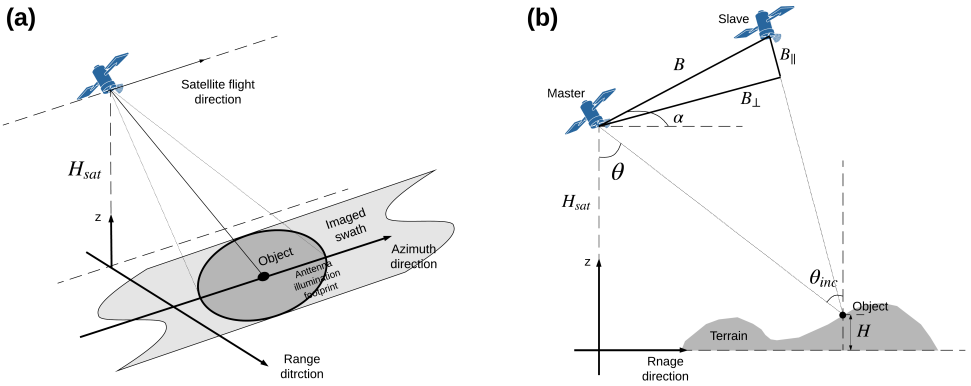

Figure 2.1: (a) SAR and (b) repeat-pass InSAR imaging geometry, adapted from Bamler and Hartl (1998). (a): The satellite at height H_{sat} moves along the azimuth direction, and the on-board radar transmits radar signal along the range direction, forming a footprint of a single purse. As the satellite flying, a swath along the azimuth direction can be imaged. (b): Two SAR sensors, master and slave are at a distance, i.e. baseline B, which can be decomposed into the parallel baseline $B_\parallel$ along the LOS direction, and the perpendicular baseline $B_\perp$ perpendicular to the LOS direction. The angle between the baseline B and the horizontal plane is defined as the baseline orientation angle α. The incidence angle θ_{inc} is the incidence angle of radar signal w.r.t. the reference ellipsoid surface. The ground object has an elevation of H w.r.t. the reference ellipsoid.

- **Topographic phase ϕ^{topo}**: This component is the effect of the surface height above the reference surface. Similar to the flat earth component, it solely depends on the viewing geometry, and can be computed as (Zebker and Goldstein, 1986; Hanssen, 2001a):

$$\phi^{\text{topo}} = \frac{-4\pi}{\lambda} \frac{B_\perp}{R\sin(\theta_{inc})} H, \tag{2.8}$$

  where R is the distance from the ground target to the satellite sensor of the master acquisition.

- **Deformation phase ϕ^{defo}**: This component is the effect of the displacement between the acquisitions of master and slave. It can be computed as

$$\phi^{\text{defo}} = \frac{-4\pi}{\lambda} D_{\text{LOS}}, \tag{2.9}$$

  where D_{LOS} is the deformation along radar LOS direction.

InSAR processing estimates the LOS deformation D_{LOS} from the interferometric phase ϕ^{w}_{intf}. In the processing, the apriori information (e.g. external DEM, precise orbit data) are required. Also, proper algorithms (e.g. corregistration, filtering and phase unwrapping algorithms) need to be applied. Many researchers have been working on InSAR processing methods, see the examples as Goldstein et al. (1988); Lee et al. (1994); Bamler and Hartl (1998); Kampes and Usai (1999); Hanssen (2001a); Ferretti et al. (2007);

Sandwell et al. (2011). Note that detailed explanation of InSAR processing steps is beyond the scope of this study.

2.1.2. Time-series InSAR techniques

As introduced in Section 1.2, the application of InSAR on deformation monitoring can be limited by three factors (Hanssen, 2001a; van Leijen, 2014; Samiei Esfahany, 2017): 1) the disturbance of atmospheric noise (atmospheric decorrelation), 2) the change of ground scattering characteristics (temporal decorrelation), and 3) the different imaging geometry due to the satellite repeat orbits are too far apart (geometric decorrelation). To cope with these limitations, the *time-series InSAR* (TInSAR) methodologies have been developed, which systematically exploit a number of interferograms from the same area.

TInSAR methodologies separate the atmospheric effect by *stacking methods* (Sandwell and Price, 1998; Wright et al., 2001; Lyons and Sandwell, 2002), based on the fact that atmospheric effects are mostly uncorrelated temporally, but correlated spatially (Hanssen, 2001a). Based on these spatio-temporal characteristics, the atmospheric effects can be separated from other signals. And in this way the atmospheric decorrelation can be mitigated.

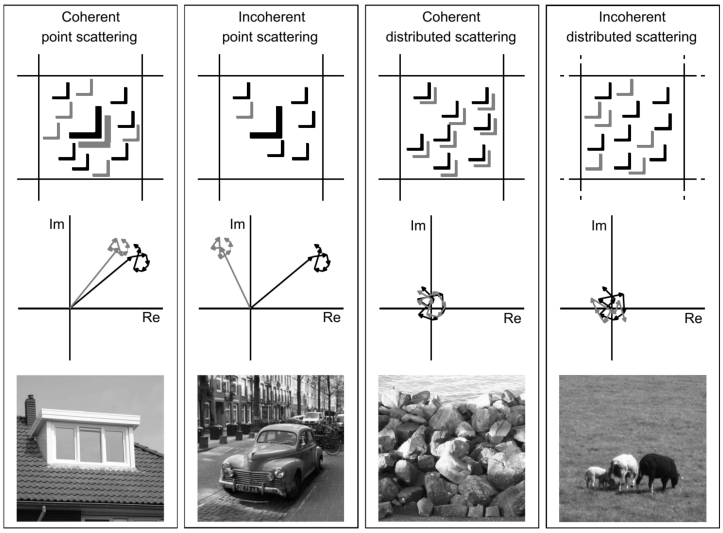

Figure 2.2: Point scattering versus distributed scattering in case of coherence or incoherence. Top) Scattering objects within a resolution cell at two acquisitions (indicated by the black and gray reflecting objects). A large object corresponds to a strong reflection, whereas the small objects represent weak reflections. Middle) Phasors for the two acquisitions (again in black and gray). Bottom) Examples of scattering objects. Adapted from van Leijen (2014).

There are in general two ways to cope with the temporal and geometric decorrelation: one is to discriminate the pixels which are minimally affected by decorrelation effects, and exclusively analyze these pixels. Another way is to include the pixels affected by decorrelation, and reduce/filter the decorrelation effect. These two ways lead to two different kinds of TInSAR methodologies, optimized towards two types of pixels with different scattering mechanisms: one is the *persistent scatterer* (PS) which is a predominant *point scatterer* within a resolution cell, and its scattering characteristics are coherent in time. The other one is the *distributed scatterer* (DS), which does not contain a dominant point scatterer, but a large number of small scattering objects in a resolution cell. DS is affected by the decorrelation effects, and may show incoherent. van Leijen (2014) illustrates the PS and DS in coherent/incoherent cases, see Fig. 2.2. In general, the TInSAR methodologies 1) exclusively analyze coherent point scatterers, i.e. PS, or 2) use proper methodologies to process DS and mitigates the decorrelation effects, or 3) apply a hybrid approach of 1) and 2).

The details of TInSAR processing methodologies are not within the scope of this study. Here we demonstrate the three key steps of TInSAR methodologies:

- **Pixel selection**. The pixels, i.e. PS or DS which will be processed by TInSAR methodologies are selected in this step. A PS-pixel is commonly selected based on two criteria: 1) the spatial and/or temporal amplitude variation of the pixel (Ferretti et al., 2001; Kampes and Adam, 2004), and 2) the spatial and/or temporal phase variation of the pixel (Ferretti et al., 2001; Hooper et al., 2004; Kampes and Hanssen, 2004; Kampes and Adam, 2006; Hanssen et al., 2008). A DS-pixel is often selected by estimating the spatial coherence or spatial phase consistency (Touzi et al., 1999; Hooper, 2008). The selected pixels can be recognized as the *InSAR measurements points*, which will be analyzed to extract the deformation signal.

- **Phase unwrapping**. The interferometric phase merely contains the phase fraction of the (actual) absolute phase, as it is wrapped in 2π, see Eq. (2.5). The *phase unwrapping* process is to reconstruct the absolute phase via estimating the number(s) of phase ambiguity. From an estimation point of view, the unwrapping problem is inherently ill-posed, and hence the solution is non-unique (Ferretti et al., 2000b; Samiei Esfahany, 2017). As a consequence, it is impossible to solve the unwrapping problem without any apriori knowledge or assumption about the signal of interest. The common unwrapping methods usually apply assumptions on the spatio-temporal deformation behavior of nearby PS-pixels (or arcs) (Ferretti et al., 2001; Adam et al., 2003; Kampes, 2005; Hooper, 2006; van Leijen, 2014), e.g. the difference between the phase of two adjacent pixels is not more than half a wave cycle (Goldstein et al., 1988; Bamler and Hartl, 1998). The result of phase unwrapping is the unwrapped time-series per InSAR measurements point, w.r.t. the reference point and the same reference epoch (the same master).

- **Atmospheric-signal mitigation**. The effects of the atmospheric signal, i.e. the *atmospheric phase screen* (APS), need to be mitigated for all the interferograms in an InSAR stack. The most common approach of APS estimation is presented in Ferretti et al. (2000c), which is adopted by Berardino et al. (2002); van Leijen (2014). By this method, the topographic phase and deformation phase are estimated and subtracted from the time series of the unwrapped interferometric phase. A high-pass filter is applied on the residuals of time series per point to acquire the atmospheric and other noises, because the atmospheric delay is a high-frequency signal in the temporal domain. Then the APS per interferogram is estimated using an interpolation method such as Kriging (Krige, 1951), since the atmospheric signal is a low-frequency signal in the spatial domain. In this way, the atmospheric signal is mitigated.

Using TInSAR, the time series of the unwrapped deformation phase can be generated. In order to detect the spatial and temporal patterns/changes, the deformation time series need to be parameterized. The theory of parameterization of InSAR deformation time series will be discussed in Section 2.2.

2.2. Mathematical methodology

In this section, we focus on the mathematical methodology of modeling the InSAR deformation time series. Given InSAR measurements, the unknown deformation model parameters can be estimated based on certain mathematical criteria. This section provides a brief review of the mathematical methodology used for InSAR deformation time series modeling.

2.2.1. Least-squares estimation

To investigate the signal of interest of a certain object, e.g. the deformation of a point target, one usually needs to build a mathematical model to describe the behavior of the signal of interest. This process is the so-called 'modeling' of the signal of interest. To perform modeling, one can usually follow a typical 5-step procedure: (Tarantola, 2005): 1) define parameters, 2) build a functional model, 3) acquire measurements and build a stochastic model, 4) estimate parameters, 5) assess quality.

At the start of modeling, one should define which parameters to use to form up the model. The model should have a sufficient number of parameters to describe the signal. On the one hand, if a model does not contain enough parameters, it will lose the description of some details of the signal. On the other hand, if a model contains too many parameters, it will result into an overestimation. Excluding the unnecessary parameters may cause losing certain details of the signal, but as long as the model still captures the main signal behavior, this sacrifice can be considered acceptable. According to the prin-

ciple of Ockham's razor (Jefferys and Berger, 1992), the model with fewest parameters that still explains the observation equally well should be preferred.

Suppose we define n unknown parameters to describe the signal, then a parameter vector $x = \begin{bmatrix} x_1 & x_2 & \cdots & x_n \end{bmatrix}^T$ is built to represent all unknown parameters.

2

After the parameters are defined, the *functional model* is built to define a quantitative relation between the defined parameters and the measurements, as in

$$E\{\underline{y}\} = f(x), \tag{2.10}$$

where $E\{.\}$ expresses the expectation operator. The vector $\underline{y}$ is the vector of the measurements. The function f defines the mathematical relation between $E\{\underline{y}\}$ and x. If f represents a linear relation, Eq. (2.10) can also be written as (Gauss, 1809; Markoff, 1912):

$$E\{\underline{y}\} = Ax, \tag{2.11}$$

where A is the so-called "design matrix" with the size of $m \times n$. In case of a nonlinear functional model, f should be linearized. This linearization is usually achieved based on Taylor's theorem (Taylor, 1717).

The *measurements* $\underline{y}$ in Eq. (2.11) are acquired by performing observations on the physical process related to the signal of interest x and m measurements, as $\underline{y} = \begin{bmatrix} \underline{y}_1 & \underline{y}_2 & \cdots & \underline{y}_m \end{bmatrix}^T$[1].

The underline of $\underline{y}$ indicates that the measurements are contaminated by stochastic noise. The behavior of the noise can be described by the stochastic model, i.e. an $m \times m$ Variance Covariance Matrix (VCM) Q_{yy}, which can be written as:

$$D\{\underline{y}\} = Q_{yy} = \begin{bmatrix} \sigma_{11}^2 & \cdots & \sigma_{1m}^2 \\ \vdots & \ddots & \vdots \\ \sigma_{m1}^2 & \cdots & \sigma_{mm}^2 \end{bmatrix}, \tag{2.12}$$

where $D\{.\}$ denotes the dispersion operator. The diagonal elements of Q_{yy} are the measurements' noise, and the off-diagonal elements are the covariances between the measurements' noise.

Then the *parameter estimation* should be performed to estimate the unknown parameters. This requires us to solve Eq. (2.11), which provides the relation between $E\{\underline{y}\}$ and x. However Eq. (2.11) cannot always be solved straightforwardly by multiplying A^{-1}, since the design matrix A is not always a square matrix, i.e. when the number of the measurements m equals to the number of the unknown model parameters n. When $m > n$, the problem is well-posed. When $m < n$, the problem is ill-posed. In this study,we will focus on the well-posed problem.

[1] Note that in this chapter, the notations $\{1 \ldots m\}$ indicates the order of all measurements, but not the epochs of acquisitions as in Chapter 3. When the vector $\underline{y}$ represents the InSAR deformation measurements, it indicates the InSAR deformation time series of one or more InSAR measurement points.

In the over-determined situation, an approximate solution to Eq. (2.11) is obtained by the *Best Unbiased Linear Estimation* (BLUE) (Gauss, 1809; Markoff, 1912), as in:

$$\boxed{\underline{\hat{x}} = (A^T Q_{yy}^{-1} A)^{-1} A^T Q_{yy}^{-1} \underline{y},} \tag{2.13}$$

where $\underline{\hat{x}}$ is the BLUE of the unknown parameters x, which meets the following criteria:

- The estimator $\underline{\hat{x}}$ is a linear function of the measurements ("Linear" criterion).
- The expectation of $\underline{\hat{x}}$ equals to the true value ("Unbiased" criterion):

$$E\{\underline{\hat{x}}\} = x, \forall x. \tag{2.14}$$

- Among all linear and unbiased estimators, the BLUE $\underline{\hat{x}}$ minimizes the residual sum of squares (Least-Squares, LS) among all linear and unbiased estimators ("Best" criterion):

$$\| A\underline{\hat{x}} - \underline{y} \|^2_{Q_{yy}^{-1}} = \min, \tag{2.15}$$

  where $\| A\underline{\hat{x}} - \underline{y} \|^2_{Q_{yy}^{-1}}$ denotes the weighted norm $(A\underline{\hat{x}} - \underline{y})^T Q_{yy}^{-1} (A\underline{\hat{x}} - \underline{y})$.

After the BLUE $\underline{\hat{x}}$ is computed, *quality control* is required to evaluate the quality of the estimation. For example, the precision of the estimated parameters can be used as an indicator to assess the quality, given by

$$Q_{\hat{x}\hat{x}} = (A^T Q_{yy}^{-1} A)^{-1}. \tag{2.16}$$

where $Q_{\hat{x}\hat{x}}$ is the VCM of $\underline{\hat{x}}$. Its diagonal elements indicate the variances of the corresponding parameters in $\underline{\hat{x}}$, while the off-diagonal elements represents the covariances between the elements of $\underline{\hat{x}}$.

2.2.2. Constrained least-squares estimation

In Section 2.2.1, we derived the BLUE $\underline{\hat{x}}$ based on Eq. (2.13). This means that $\underline{\hat{x}}$ is estimated fully based on the measurements $\underline{y}$. In some situations, observations from external sources are also available, besides $\underline{y}$. These extra observations can provide information on the functional or stochastic behavior of the unknown parameter x. A way to formalize and exploit this knowledge of the model is to subject the least-squares estimation results to the external information, by using *constrained least-squares estimation*.

The functional behavior of x given by apriori information can be expressed by:

$$E\{\underline{d}\} = g(x), \tag{2.17}$$

where $\underline{d}$ is the vector of *pseudo observations*. The knowledge of $\underline{d}$ is acquired from external information and not from real measurements as $\underline{y}$ in Eq. (2.10). The function g

defines the relation between the unknown model parameters x and the expectation of extra observations $\underline{d}$. When Eq. (2.17) is linear, it can be written into

$$E\{\underline{d}\} = Gx, \tag{2.18}$$

where the matrix G is the design matrix of the functional model. In case that Eq. (2.17) is non-linear, it can be linearized into Eq. (2.18) using Taylor's theorem.

Similar as Eq. (2.12), the uncertainties of the extra observations $\underline{d}$ are defined by:

$$D\{\underline{d}\} = Q_{dd}, \tag{2.19}$$

where Q_{dd} is the VCM of the extra observations.

With the constraints given by Eqs. (2.18) and (2.19), we estimate the unknown parameter x following the three criteria of BLUE (see Section 2.2.1), but also subjected to the estimation with external information. Therefore, one needs to choose whether the estimation should have a better fit to the observations $\underline{y}$, or the estimation is more subjected to the constraint (Eq. (2.18)). One way to do this is to give a regularization parameter (Tikhonov, 1963; Tikhonov et al., 1977). Another way is to determine this balance based on the given VCMs, i.e. Q_{yy} and Q_{dd}. The "Best" criterion in Eq. (2.15) will be defined as:

$$\|A\underline{\hat{x}} - \underline{y}\|^2_{Q^{-1}_{yy}} + \|G\underline{\hat{x}} - \underline{d}\|^2_{Q^{-1}_{dd}} = \min, \forall \underline{x}, \tag{2.20}$$

where $\underline{\hat{x}}$ denotes the class of all linear and unbiased estimators. In Eq. (2.20), $\|A\underline{\hat{x}} - \underline{y}\|$ and $\|G\underline{\hat{x}} - \underline{d}\|$ denotes the residuals of functional model to the observations $\underline{y}$ and the pseudo observations $\underline{d}$. The VCMs Q_{yy} and Q_{dd} serve as the metrics of weight in Eq. (2.20). Based on Eq. (2.20), the BLUE $\underline{\hat{x}}$ is subjected to the pseudo observations, and can be written as

$$\boxed{\underline{\hat{x}} = (A^T Q^{-1}_{yy} A + G^T Q^{-1}_{dd} G)^{-1} (A^T Q^{-1}_{yy} \underline{y} + G^T Q^{-1}_{dd} \underline{d}).} \tag{2.21}$$

The constrained least-squares estimation allows one to import the extra information on the functional model. If the apriori knowledge on the signal of interest is available, e.g. given the difference of deformation velocities of two InSAR measurement points equals to the value $\underline{v}_0$ and its variance σ^2_0, then the least-squares estimation can be subjected to this contextual information. If the contextual information is correct, then taking into account this information into modeling can help one to derive more physical realistic model.

In the particular case of modeling InSAR deformation time series, the constrained least-squares estimation imports extra information to the functional and stochastic model of deformation. Taking into account the correct contextual information can improve the modeling results.

2.3. Summary

In this chapter, we reviewed the InSAR principle and the mathematical methodologies for InSAR deformation modeling. We introduced the generic TInSAR processing procedure, and presented the modeling theory based on least-squared estimation and constrained least-squared estimation. In Chapter 3 we introduce the functional and stochastic model of modeling InSAR deformation time series.

3

Spatio-Temporal Deformation Modelling

TInSAR processing derives the deformation time series of InSAR measurements points. To study the deformation behavior of a large area with a huge number of InSAR measurement points, analyzing the InSAR deformation time series point-by-point is inefficient. As mentioned in Section 2.2.1, the deformation behavior, which is the physical phenomenon of interest in this study, can be represented by a set of deformation model parameters, e.g. deformation velocities. These parameters can be estimated from the InSAR deformation time series, given certain apriori knowledge and assumptions.

In this chapter, a spatio-temporal modeling algorithm of InSAR deformation time series is introduced.

3.1. Point-wise deformation modeling

A number of temporal deformation models can be suggested by using apriori information to describe the deformation behavior of an InSAR measurement point. Choosing the "optimal" model among these remains a challenge. In this study, hypothesis testing is applied to select the optimal model of an InSAR measurement point among all possible models. This process is referred to as *point-wise deformation modeling* (Chang and Hanssen, 2016). In Section 3.1.1, the functional model of the point-wise modeling is introduced. In 3.1.2 we introduce how to build up the stochastic model. In 3.1.3, the theory of selecting optimal model using hypothesis testing method is introduced.

3.1.1. Functional model

Given $m+1$ SLC acquisitions, using TInSAR processing, the InSAR measurement points are selected and their deformation time series with m epochs can be established w.r.t. the same reference point r and the same reference epoch o. Then for an InSAR measurement point p, the InSAR observations representing the deformation time series can be written as:

$$\underline{y}^p = \begin{bmatrix} \underline{y}^p_1 & \underline{y}^p_2 & \cdots & \underline{y}^p_m \end{bmatrix}^T, \tag{3.1}$$

where the vector $\underline{y}^p$ is an $m \times 1$ vector representing the deformation time series of point p, where $\underline{y}^p_i$, $i \in [1, m]$ is the deformation of p at the epoch i, w.r.t. the reference epoch o

and the reference point r.

Conventionally, the deformation time series of p can be represented by a linear function of time (Teunissen, 2003a, 2006; Caro Cuenca, 2012), as in:

$$E\{\underline{y}_i^p\} = t_i \cdot v^p, \tag{3.2}$$

where t_i is the temporal baseline of the ith epoch w.r.t. the reference epoch o, and v^p is the deformation velocity of InSAR measurement point p. Eq. (3.2) is also referred to as "constant velocity function", which is sufficient to facilitate phase unwrapping efficiently.

However, due to the potential combination of driving mechanisms, the constant velocity function may not be adequate for all the InSAR measurement points. When non-linear components exist in the deformation time series of p, then the expectation of $\underline{y}_i^p$ can be written as:

$$E\{\underline{y}_i^p\} = t_i \cdot v^p + \mu_i^p, \tag{3.3}$$

where μ_i^p represents the non-linear deformation of InSAR measurement point p at the ith epoch, w.r.t the reference epoch o and reference point p[1]. The term μ_i^p can be formulated in different forms due to the combination of different driving mechanisms of deformation, e.g. temperature variation (Chang et al., 2014), ground water extraction (Sinclair, 1982) or gas production (Ketelaar, 2009). To describe the deformation behavior, a *library of canonical functions* (Chang, 2015; Chang and Hanssen, 2016) can be established. These canonical functions can be used as basic "building blocks" to describe any type of deformation behavior. The canonical functions are listed as below:

- **Breakpoint function**. For some cases, the deformation velocity v^p may not be a constant value along time, but have several different values for specific time spans. This deformation behavior is observed when the ground motion is directly coupled to the production volumes of water or hydrocarbons (Ketelaar, 2009). The velocity changes between two time spans are referred to as the "breakpoint" (Chang et al., 2014). To describe the deformation behavior, one can regard the deformation velocity v^p as the velocity before any breakpoint occurs, and model the deformation velocity change w.r.t v_p after every breakpoint appear. For instance, if only one breakpoint occurs at the bth epoch in the deformation time series of p, as shown in Fig. 3.1, the breakpoint function can be expressed as:

$$\mu_i^p(\delta v^p) = \begin{cases} 0, & t_i < t_b \\ \delta v_1 (t_i - t_b), & t_i \geqslant t_b \end{cases}, \tag{3.4}$$

  where $\mu_i^p(\delta v^p)$ is the contribution of the breakpoint function to the nonlinear deformation term μ_i^p in Eq. (3.3). Before the bth epoch no breakpoint exist, therefore

[1] Note that the non-linear deformation component μ_i^p is an unknown deterministic parameter, and should not be confused with a stochastic error component of the measurements.

the velocity change equals to 0. The term δv_1 indicates the velocity change after the breakpoint at the bth epoch. The term t_b is the temporal baseline for the bth epoch w.r.t. the reference epoch o.

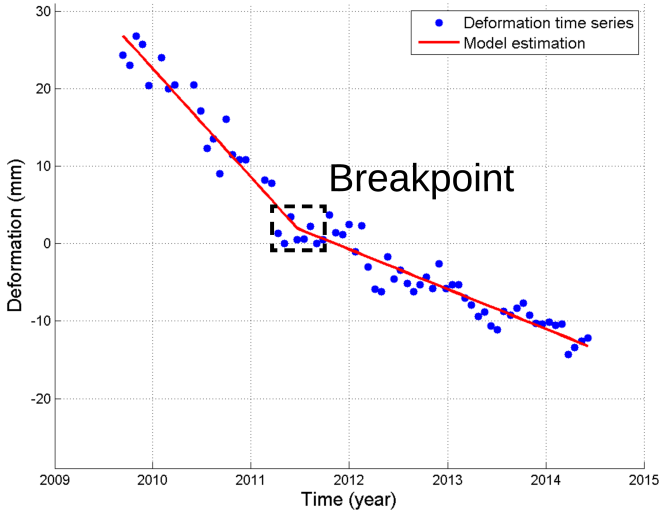

Figure 3.1: An example of the breakpoint function. The blue dots indicate the deformation times series computed with TInSAR processing. The red line is the estimated deformation model with both constant velocity function and breakpoint function. One breakpoint occurs at the June 8th of 2011. The deformation time series are derived from actual Radarsat-2 SAR data with 5.6cm wavelength.

Now we extend Eq. (3.4) to the case of multiple breakpoints. Given n_b breakpoints which occur at epoch $[b_1, b_2, ..., b_{n_b}]$, where $n_b \in [1, m-2]$ since the breakpoint cannot occur at the first and the last epoch of the time series. Then the breakpoint function can be written as:

$$\mu_i^p(\delta v^p) = \begin{cases} 0, & t_i < t_{b_1} \\ \delta v_1 (t_i - t_{b_1}), & t_{b_1} \leqslant t_i < t_{b_2} \\ \delta v_1 (t_{b_2} - t_{b_1}) + \delta v_2 (t_i - t_{b_2}), & t_{b_2} \leqslant t_i < t_{b_3} \\ \cdots \\ \delta v_1 (t_{b_2} - t_{b_1}) + \cdots + \delta v_{n_b} (t_i - t_{b_{n_b}}), & t_{b_{n_b-1}} \leqslant t_i < t_{b_{n_b}}, \end{cases} \tag{3.5}$$

where $[\delta v_1, \delta v_2, \cdots, \delta v_{n_b}]$ are the velocity changes of the n_b time spans after the first breakpoint occurs.

- **Step function**. Sometimes the instantaneous events or unwrapping errors may

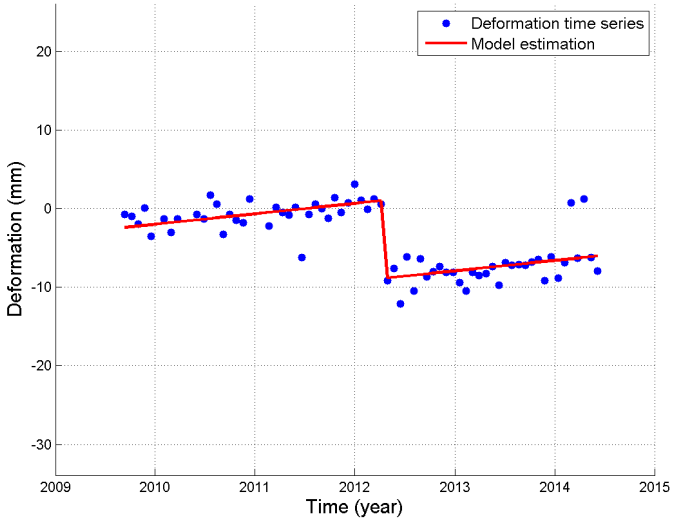

Figure 3.2: An example of the step function together with constant velocity function. The blue dots indicates the deformation times series computed with TInSAR processing. The red line is the estimated deformation model with both constant velocity function and step function. One step occurs at May 1st, 2012. The deformation time series are derived from Radarsat-2 SAR data with 5.6*cm wavelength.*

reveal themselves as jumps in deformation time series. In this situation a step function can be introduced. If one step occurs at the sth epoch in the deformation time series, as shown in Fig. 3.2 the step function is

$$\mu_i^p(\triangle^p) = \mathbb{H}(t_i, t_s)\triangle^p, \tag{3.6}$$

where $\mu_i^p(\triangle^p)$ is the contribution of the step function to the nonlinear deformation term μ_i^p in Eq. (3.3). The term t_s is the temporal baseline of the sth epoch w.r.t. the reference epoch o. The scalar $\triangle_s^p$ represents the step magnitude at the sth epoch of InSAR measurement point p. The Heaviside step function $\mathbb{H}$ (Weisstein, 2008) is written as

$$\mathbb{H}(t_i, t_s) = \begin{cases} 0, & t_i < t_s \\ 1, & t_i \geqslant t_s \end{cases}, \tag{3.7}$$

where the value of the Heaviside step function $\mathbb{H}(t_i, t_s)$ can only be either 0 or 1.

Now we extend Eq. (3.6) to multiple steps situation. Given n_s steps which occur at epoch $[s_1, s_2, ..., s_{n_s}]$, where $n_s \in [1, m-2]$ since the step cannot occur at the first and the last epoch of the time series. Then the step function can be expressed as

$$\mu_i^p(\triangle^p) = \mathbb{H}(t_i, t_{s_1})\triangle_{s_1}^p + \mathbb{H}(t_i, t_{s_2})\triangle_{s_2}^p + \cdots + \mathbb{H}(t_i, t_{s_{n_s}})\triangle_{s_{n_s}}^p, \tag{3.8}$$

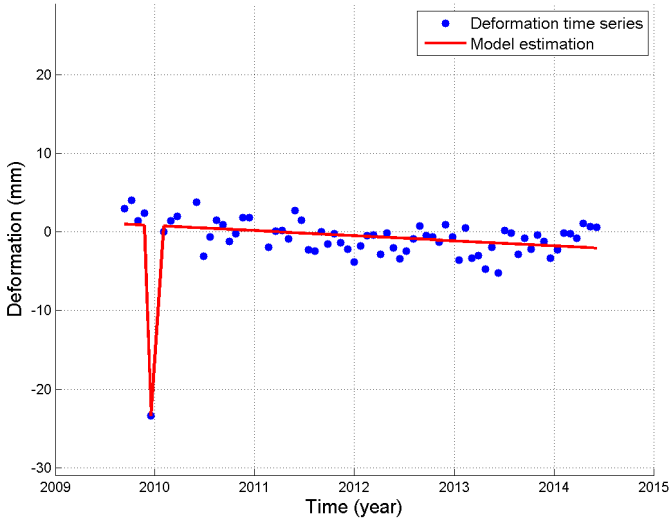

Figure 3.3: An example of the outlier function together with constant velocity function. The blue dots indicates the deformation times series computed with TInSAR processing. The red line is the estimated deformation model with both constant velocity function and outlier function. One step occurs at Dec 22nd, 2009. The deformation time series are derived from Radarsat-2 SAR data with 5.6*cm wavelength.*

where $[\triangle^p_{s_1}, \triangle^p_{s_2}, \cdots, \triangle^p_{s_{n_s}}]$ are the magnitude of all steps occurring in the deformation time series of InSAR measurement point p.

- **Outlier function**. A jump can also exist at a single epoch in the time series, which is referred to as the "outlier function" in this study. The outlier function does not only describe errors in the deformation time series, e.g. unwrapping errors, but can also represent the instantaneous offset due to actual physical events. Given n_ϵ outliers at the epoch $[\epsilon_1, \epsilon_2, ..., \epsilon_{n_\epsilon}]$ in the deformation time series of the InSAR measurement point p, the offset function can be written as

$$\mu^p_i(D^p) = \mathbb{K}(t_i, t_{\epsilon_k}) D^p_i, \tag{3.9}$$

where $\mu^p_i(D^p)$ represents the contribution of the outlier function to the nonlinear deformation term μ^p_i in Eq. (3.3), and D_{p_i} is the magnitude of the outlier at epoch i. $\mathbb{K}(t_i, t_\epsilon)$ is the Kronecker delta (Kaplan, 1952) as in

$$\mathbb{K}(t_i, t_\epsilon) = \begin{cases} 1, & t_i = t_\epsilon, \\ 0, & else \end{cases}, \tag{3.10}$$

where the outliers occur at epoch t_ϵ and $n_\epsilon \in [0, m-2]$ is the total number of outliers.

- **Sinusoid function**. When studying the deformation over peatland and permafrost area, the sinusoid function (Kampes, 2005; van Leijen and Hanssen, 2008) can be applied to describe the deformation, (Brown and Kupsch, 1974; Wu et al., 2002; Glaser et al., 2004) as in

$$\mu_i^p(S^p, C^p) = \sin(2\pi t_i) \cdot S^p + (\cos(2\pi t_i) - 1) \cdot C^p, \tag{3.11}$$

  where $\mu_i^p(S^p, C^p)$ is the contribution of the sinusoid function to the nonlinear deformation term μ_i^p in Eq. (3.3). The coefficients S^p and C^p represents the seasonal periodic deformation with the amplitude $\sqrt{(S^p)^2 + (C^p)^2}$. Note that t_i here has the unit of year.

- **Exponential function**. For post-seismic deformation (Savage et al., 2003), landslides (Montgomery et al., 1998) or soil settlement or compaction (Verruijt and Van Baars, 2007), an exponential function may be the optimal parameterization,

$$\mu_i^p(\kappa^p, \beta^p) = (1 - \exp(-\frac{t_i}{\beta^p})) \cdot \kappa^p, \tag{3.12}$$

  where $\mu_i^p(\kappa^p, \beta^p)$ is the contribution of the exponential function to the nonlinear deformation term μ_i^p in Eq. (3.3). The term κ^p scales the function, and the characteristic time β^p is associated with the decreasing relaxation in time.

  The exponential function is a non-linear function of time. Therefore it needs to be linearized by Taylor expansion (Taylor, 1717) in order to estimate the parameters (Teunissen, 1989). Such nonlinear least squares estimation is prone to a biased estimation, i.e. $E\{\underline{\hat{x}}\} \neq x$, due to the neglect of the second- and higher-order terms of Taylor expansion. Therefore, in some cases, the piecewise linear model can be considered as an alternative approach.

Based on the library of canonical functions, the nonlinear term μ_i^p in Eq. (3.3) can be expressed as one particular canonical function, or the combination of several canonical functions in the library. Therefore one needs to decide the optimal model to parameterize the deformation behavior of the InSAR measurement point p. The hypothesis testing can be applied to make this decision, which will be introduced in Section 3.1.3.

3.1.2. Stochastic model

When no priori knowledge about the noise in the observations $\underline{y}^p$ is available, we can start to build a simple stochastic model as

$$D\{\underline{y}^p\} = Q^p = \sigma^2_{\text{VUW}} R_{yy}, \tag{3.13}$$

where Q^p is the $m \times m$ VCM of the deformation time series at all epochs of InSAR measurement point p. The diagonal entries represent the variances of $\underline{y}^p$, and the off-diagonal entries describe the covariances, i.e. the correlated noises. The stochastic model consists of a variance of unit weight σ^2_{VUW} and a cofactor matrix R_{yy}. If we assume all InSAR measurements to be equal weighted and independent, then $R_{yy} = I$, where I is an diagonal unit matrix. The variance of unit weight σ^2_{VUW} can be fixed from experience, e.g. 9 mm^2 for TerraSAR-X, or 25 mm^2 for RADARSAT-2 (Ketelaar, 2009; Chang et al., 2014).

An alternative way to build the stochastic model of $\underline{y}^p$ is based on apriori information on the two major components of the InSAR measurement noise: the *Scattering noise* and the *Atmospheric noise*, (Hanssen, 2001a) which are introduced as below:

- *Scattering noise* is a combination of the thermal noise, the scattering mechanism, and the resampling/coregistration errors. The scattering noise has been well-studied in the InSAR community (Marinkovic et al., 2008; Ferretti et al., 2007). Given InSAR measurement point p, we use σ_ψ to represent the phase standard deviation caused by scattering noise in the SLC phase observations of point p. According to previous studies (Ferretti et al., 2001), the standard deviation σ_ψ is assumed to have a strong correlation with the normalized amplitude dispersion D_a, as in

$$D_a = \frac{\sigma_a}{\mu_a} \approx \sigma_\psi, \tag{3.14}$$

  where D_a is the normalized amplitude dispersion of p. The terms μ_a and σ_a are respectively the temporal mean and standard deviation of the amplitude time series of p. The phase standard deviation is in rad, and is converted to meters as:

$$\sigma_n = \frac{\lambda}{4\pi}\sigma_\psi, \tag{3.15}$$

  where σ_n is the standard deviation in meters, and λ is the radar wavelength. The scattering noise in the SLC observations of InSAR measurement point p is considered to be independent between each other (Ferretti et al., 2001; Marinkovic et al., 2008). However for $\underline{y}^p$, which is the InSAR observations on deformation time series , each of its elements, i.e. $\underline{y}^p_i$ is the double difference between the SLC observation of point p at the ith epoch w.r.t. the reference epoch o and the reference point r. Therefore the scattering noise in $\underline{y}^p$ is correlated between epochs, due to sharing the same reference epoch and reference point. Then the scattering noise component in the full matrix VCM of $\underline{y}^p$ will be:

$$Q^p_{\text{scat}} = \begin{bmatrix} \sigma^2_{\text{scat}}(1o,pr) & \sigma^2_{\text{scat}}(12,pr) & \cdots & \sigma^2_{\text{scat}}(1m,pr) \\ \sigma^2_{\text{scat}}(21,pr) & \sigma^2_{\text{scat}}(2o,pr) & \cdots & \sigma^2_{\text{scat}}(2m,pr) \\ \vdots & \vdots & \ddots & \vdots \\ \sigma^2_{\text{scat}}(m1,pr) & \sigma^2_{\text{scat}}(m2,pr) & \cdots & \sigma^2_{\text{scat}}(mo,pr) \end{bmatrix}, \tag{3.16}$$

where Q^p_{scat} is the VCM of $\underline{y}^p$ caused by scattering noises. Its element $\sigma^2_{\text{scat}}(ij,pr)$, with $i,j \in [1,m]$ can be written as: (Hanssen, 2001a; Samiei-Esfahany and Hanssen, 2013)

$$\begin{aligned}\sigma^2_{\text{scat}}(io,pr) &= 4\sigma^2_n \\ \sigma^2_{\text{scat}}(ij,pr) &= 2\sigma^2_n,\end{aligned} \tag{3.17}$$

where $\sigma^2_{\text{scat}}(io,pr)$ denotes the scattering noise variance of $\underline{y}^p_i$, and $\sigma^2_{\text{scat}}(ij,pr)$ is the covariance between two double difference observations $\underline{y}^p_i$ and $\underline{y}^p_j$.

3

- *Atmospheric noise* is one of the dominant error sources in InSAR data (Hanssen, 2001a). It is mainly caused by the heterogeneity of the wet component of atmosphere, which delays in the transition of radar signal. Previous studies (Hanssen and Klees, 1998; Emardson et al., 2003) show that the variability of atmospheric noise between two points increases with distance between the points, which can be described by a variogram model as in(Hanssen, 2001a; Liu, 2012)

$$z_i(l) = \sigma^2_{w_i} e^{(-\frac{l}{L_{w_i}})}, \tag{3.18}$$

where $z_i(l)$ represents the variogram of atmosphere delay between two points at the epoch t_i, with l the distance between the two points. The term $\sigma^2_{w_i}$ represents the atmosphere variance factor at the epoch t_i, and L_{w_i} the decorrelation distance at the epoch t_i. The two parameters of the variogram model, i.e. σ_{w_i} and L_{w_i} can be estimated from the atmospheric data, which can be acquired by atmosphere filtering in TInSAR processing. Considering the double differences, based on error propagation law, the atmosphere component in the full matrix VCM of $\underline{y}^p$ is

$$Q^p_{\text{atm}} = \begin{bmatrix} \sigma^2_{\text{atm}}(1o,pr) & \sigma^2_{\text{atm}}(12,pr) & \cdots & \sigma^2_{\text{atm}}(1m,pr) \\ \sigma^2_{\text{atm}}(21,pr) & \sigma^2_{\text{atm}}(2o,pr) & \cdots & \sigma^2_{\text{atm}}(2m,pr) \\ \vdots & \vdots & \ddots & \vdots \\ \sigma^2_{\text{atm}}(m1,pr) & \sigma^2_{\text{atm}}(m2,pr) & \cdots & \sigma^2_{\text{atm}}(mo,pr) \end{bmatrix}, \tag{3.19}$$

where Q^p_{atm} is the VCM of $\underline{y}^p$ caused by atmospheric noise. Its element $\sigma^2_{\text{atm}}(ij,pr)$, with $i,j \in [1,m]$ can be written as: (Samiei-Esfahany and Hanssen, 2013)

$$\begin{aligned}\sigma^2_{\text{atm}}(io,pr) &= 2\sigma^2_{w_i} + 2\sigma^2_{w_o} - 2\sigma^2_{w_i} e^{(-\frac{l_{pr}}{L_{w_i}})} - 2\sigma^2_{w_o} e^{(-\frac{l_{pr}}{L_{w_o}})} \\ \sigma^2_{\text{atm}}(ij,pr) &= 2\sigma^2_{w_j} - 2\sigma^2_{w_i} e^{(-\frac{l_{pr}}{L_{w_i}})},\end{aligned} \tag{3.20}$$

where $\sigma^2_{\text{atm}}(io,pr)$ denotes the variance of $\underline{y}^p_i$ caused by atmospheric noise, and $\sigma^2_{\text{atm}}(ij,pr)$ is the covariance between two double difference observations $\underline{y}^p_i$ and $\underline{y}^p_j$.

After Q^p_{scat} and Q^p_{atm} are acquired, we can use the sum of these two major component of the VCM of $\underline{y}^p$ to establish the apriori stochastic model

$$D\{\underline{y}^p\} = Q^p = Q^p_{\text{scat}} + Q^p_{\text{atm}}, \tag{3.21}$$

where Q^p is the VCM of the InSAR deformation time series $\underline{y}^p$. Note that in Eq. (3.21), some effects caused by the InSAR processing were not taken into account. For instance, applying atmospheric filtering will affect the spatial-temporal correlation. One way to improve the apriori stochastic model is to use a Monte Carlo approach to account for these effects(Samiei-Esfahany and Hanssen, 2013).

3.1.3. Point-wise multiple hypothesis testing

In Section 3.1.1 and 3.1.2 the functional model and stochastic model of the point-wise modeling are given. In order to determine a most probable deformation model behavior of a single InSAR measurement point p, Multiple Hypothesis Testing (MHT) (Chang et al., 2014) is applied per point.

Based on the combinations of canonical functions stated in Section 3.1.1, one can set a null hypothesis H_0 as the most likely deformation model of InSAR measurement point p. A set of alternative hypotheses H_j's are established besides H_0, which are the alternative deformation models of p. Without loss of generality, the mathematical expressions for H_0 and all H_j's, $\forall\, j$ are expressed as linear systems of observation equations (Chang et al., 2014)

$$\begin{aligned} H_0 &: E\{\underline{y}^p\} = A^p_0 x^p_0; & D\{\underline{y}^p\} &= Q^p \\ H_j &: E\{\underline{y}^p\} = A^p_0 x^p_0 + C^p_j \nabla^p_j; \quad \nabla_j \neq 0 & D\{\underline{y}^p\} &= Q^p, \end{aligned} \tag{3.22}$$

where H_0 and H_j are the null and alternative hypothesis, respectively. The matrix A^p_0 denotes the design matrix of the null hypothesis, and x^p_0 is the unknown parameter vector of the null hypothesis. A specification matrix C^p_j and an additional vector of unknown parameters ∇^p_j are introduced in the alternative hypothesis.

We use the "constant velocity model" as the null hypothesis H_0, as the deformation behavior of most InSAR measurement points can be described as a linear function of time (Teunissen, 2003a, 2006; Chang et al., 2014).

We follow a Detection-Identification-Adaption (DIA) procedure (Teunissen, 1990) to select the optimal deformation functional model of p, from the library of canonical functions. First, we determine whether the default model H_0 can be sustained. In case of H_0 is rejected, the most probable hypothesis H_b in all H_j's will be identified. The final decision on whether rejecting H_0 will be made by comparing H_0 with H_b. The rejection of H_0 directly leads to sustaining H_b.

An Overall Model Test (OMT) is first applied to the null hypothesis H_0. The OMT

follows a *test statistic* $\underline{T}_0^p$, which is (Teunissen et al., 2005)

$$\underline{T}_0^p = (\underline{\hat{e}}_0^p)^T (Q^p)^{-1} \underline{\hat{e}}_0^p \tag{3.23}$$

where $\underline{\hat{e}}_0^p = \underline{y}^p - A_0^p \underline{\hat{x}}_0^p$ is the residual between the functional model of the null hypothesis and the observations, and $\underline{\hat{x}}_0^p$ is the BLUE of x_0^p. The test statistic $\underline{T}_0^p$ follows a *Chi-squared* distribution $\underline{T}_0^p \sim \chi^2(q_0, \lambda_0)$, where q_0 is the degree of freedom applied in the OMT, which can be determined by the number of redundant observations, i.e. $q_0 = m - n_0$ where m is the number of observations and n_0 the number of unknown parameters in H_0. The term λ_0 is the level of non-centrality applied of the Chi-squared distribution of $\underline{T}_0^p$, and for H_0 we have $\lambda_0 = 0$ (Teunissen et al., 2005).

The decision of whether starting MHT is made by comparing $\underline{T}_0^p$ to a critical value:

$$K_0 = \chi^2_{\alpha_0}(q_0, 0), \tag{3.24}$$

where K_0 is the critical value of OMT. It is computed based on the Chi-squared distribution of $\underline{T}_0^p$, given level of significance α_0, which refers to the Type-I error: rejecting H_0 while it is true (Teunissen, 2003b). A smaller α_0 would result in a lower possibility of wrongly rejecting H_0. The choice of α_0 is dependent on the cost of making a Type-I error, and can be different in the application cases. Here we suggest setting α_0 based on the external source of information.

The MHT will start if $\underline{T}_0^p > K_0$, otherwise H_0 will be sustained. The test of every alternative hypothesis H_j follows a test statistics $\underline{T}_j^p$

$$\underline{T}_j^p = (\underline{\hat{e}}_0^p)^T (Q^p)^{-1} \underline{\hat{e}}_0^p - (\underline{\hat{e}}_j^p)^T (Q^p)^{-1} \underline{\hat{e}}_j^p, \tag{3.25}$$

where $\underline{\hat{e}}_j^p = \underline{y}^p - (A_0^p \underline{\hat{x}}_0^p + C_j^p \underline{\hat{\nabla}}_j^p)$ is the residual between the functional model of the alternative hypothesis and the observations, and $\underline{\hat{\nabla}}_j^p$ is the BLUE of ∇_j^p. In Eq. (3.25), the value of $\underline{T}_j^p$ is always non-negative, since the model will have a better fit to the observations when more additional parameters are added, making $(\underline{\hat{e}}_0^p)^T (Q^p)^{-1} \underline{\hat{e}}_0^p \geq (\underline{\hat{e}}_j^p)^T (Q^p)^{-1} \underline{\hat{e}}_j^p$. The test statistics of alternative hypotheses follow a Chi-squared distribution as $\underline{T}_j^p \sim \chi^2(q_j, \lambda_j), \forall j$, where the degree of freedom $q_j = n_j$, and n_j is the number of additional parameters of H_j. The term λ_i is the level of non-centrality, and $\lambda_j \neq 0, \forall j$.

The criterion of selecting the "optimal" alternative hypothesis H_b is based on comparing $\underline{T}_j^p$'s. However, when the alternative hypotheses have different degrees of freedom q_j, the distributions of $\underline{T}_j^p$'s are different, which makes it impossible to compare the $\underline{T}_j^p$'s directly. One way to normalize the test statistics is to divide it by its critical value $\chi^2_{\alpha_j}(q_j, \lambda_j)$, as

$$\underline{\mathbf{T}}_j^p = \frac{\underline{T}_j^p}{\chi^2_{\alpha_j}(q_j, \lambda_j)} \tag{3.26}$$

where $\underline{\mathbf{T}}_j^p$ is the *test ratio* of H_j. In Eq. (3.26), the critical value $\chi^2_{\alpha_j}(q_j, \lambda_j)$ relates to the level of significance α_j, the degree of freedom q_j, and the level of non-centrality λ_j. In MHT, the aim is to choose the optimal alternative hypothesis H_b among all H_j's. Therefore one should make sure that the probability of accepting each alternative hypothesis, knowing that it is true, is identical for all alternative hypotheses. This probability is referred to as the power of test, also called the *discriminatory power*, γ. We apply the same γ on the test of all alternative hypothesis. This testing method is known as the B-method of testing (Baarda, 1968), whose essence is to fix the discriminatory power and calculate the uniform non-centrality parameter, i.e. $\lambda_j = \lambda_0, \forall j$ (Teunissen et al., 2005)

$$\lambda_0 = \lambda(\gamma, \alpha_0, q_0), \tag{3.27}$$

where α_0 is the initial level of significance, and $q_0 = 1$ is the initial degree of freedom (Chang et al., 2014). Then λ_0 and γ are fixed. A loop runs over all H_j's, and for each alternative hypothesis a new α_j is computed as

$$\alpha_j = \alpha(\lambda_0, \gamma, q_j). \tag{3.28}$$

Then we can use Eq. (3.26) to compute the test ratio for all H_j's. The null hypothesis H_0 will be rejected if

$$\underline{\mathbf{T}}_a^p > 1 \quad \text{and} \quad \underline{\mathbf{T}}_a^p = \max\{\underline{\mathbf{T}}_j^p\}, \quad \forall j \tag{3.29}$$

where $\underline{\mathbf{T}}_a^p$ is the test ratio of the "optimal" hypothesis H_b from all H_j's. Note that when $\underline{\mathbf{T}}_a^p \leq 1$, the test statistic $\underline{\mathbf{T}}_j^p$ does not exceed the corresponding critical value $\chi^2_{\alpha_j}(q_j, \lambda_j)$, as the result the "optimal" alternative hypothesis H_b is not more probable than than the null hypothesis H_0, therefore H_0 will not be rejected and H_b will be discarded (Chang et al., 2014).

3.2. Cluster-wise deformation modeling

In the point-wise modeling, the deformation model of each InSAR measurement point has been determined separately, which means that until now we consider the deformation time series of all InSAR measurement points to be independent. However, in reality, the deformation time series of some InSAR measurement points show spatial smoothness in a certain degree, which results in the spatially correlation of the InSAR measurements. This spatial correlation shows in two aspects:

- The InSAR *noise* is spatially correlated. In Section 3.1.2 we built the stochastic model for point-wise deformation modeling, taking into account the temporal correlation caused by sharing the same reference epoch o. However, the spatial correlation of noise has not been included in the stochastic model. The InSAR noise can be spatially correlated due to: 1) the TInSAR processing produces InSAR deformation time series w.r.t. the same reference point r (van Leijen, 2014), and 2)

the atmospheric noise follows a "power law" in spatial domain (Hanssen, 2001a), therefore is spatially correlated (Samiei-Esfahany and Hanssen, 2013).

- The deformation *signal* between InSAR measurement points can be spatially correlated, because some InSAR measurement points are likely to be measuring the same deformation behavior, due to the same deformation mechanism (Ketelaar, 2009). In Section 3.1.1 and 3.1.3, we chose the optimal deformation model for every InSAR measurement point by applying MHT, based the library of canonical functions. However, the choice of deformation model for every InSAR measurement point is independent of other InSAR measurement points. In reality, some InSAR measurement points may measure the deformation caused by the same driving mechanism, e.g. they measure the deformation of the same civil construction, or the same deformation feature such as a deformation bowl. These measurements provide extra redundancy when estimating the deformation model which is driven by the same deformation mechanism.

Previous studies have been done on specifying the noise-related spatial correlations, by building up a full-matrix VCM as the stochastic model (Hanssen, 2001a; Samiei-Esfahany and Hanssen, 2013). On the other hand, to take into account the signal-related spatial correlation, the apriori spatial smoothness information is required. When the spatial correlation of deformation signal is properly considered, the deformation modeling results will be more physically realistic. To import the spatial correlation into deformation modeling, in this Section, we propose a method to group the InSAR measurement points and model their deformation based on the given information of the spatial smoothness of deformation signal. This group of InSAR measurement points is referred as a *cluster*, and we introduce the *cluster-wise* modeling method in this Section.

In Section 3.2.1, the definition of a cluster will be introduced. The functional and stochastic model of cluster-wise modeling will be introduced in Section 3.2.2 and Section 3.2.3, respectively. The model selection methodology for the cluster will be introduced in Section 3.2.4.

3.2.1. Definition of a cluster

To take into account the spatial correlation, mainly on the signal aspect, the InSAR measurement points will form the so-called "clusters", and the deformation behavior of each cluster in the area of interest will be modeled. The spatio-temporal correlation of the InSAR measurement points within each cluster will be taken into account. We define a cluster as:

A group of InSAR measurement points within a same pre-defined area, and their deformation behavior can be described by a single spatio-temporal deformation model.

Then two essential questions need to be answered when defining a cluster:

- **How to define the extent of a cluster?** The InSAR measurement points in a same cluster should be within the same pre-defined area. This criterion comes from the assumption that the deformation signal is only correlated within a certain spatial range. The extent of the area of a cluster should be defined based on this spatial correlation range. Therefore the area of the cluster should be defined from the spatial smoothness information of the deformation signal.
- **What deformation model should be applied to describe the deformation behavior of a cluster?** The InSAR measurement points in the same cluster should also follow the same deformation model. This criterion is based on the assumption that if the InSAR measurement points are spatially close and have the same deformation model, then they are likely to be measuring the same deformation behavior, therefore are spatially correlated on the signal aspect. The knowledge on the deformation behavior is then needed to answer this question.

Therefore, to define a cluster, one needs to have the apriori spatial smoothness information on two aspects: 1) To define the spatial extent of a cluster, the knowledge of the correlation range of deformation signal should be provided; 2) To determine the deformation model that all InSAR measurement points in a cluster follow, the knowledge on the deformation behavior of the area of interest is required. However, the above knowledge cannot be acquired from InSAR observations without any information from the external sources. To define a cluster, the contextual information is required, which can be provided by the following sources:

- **Expert knowledge or experience**. A relevant domain expert can provide knowledge on the background of deformation. For instance, the previous studies have been done using the InSAR observations to yield the parameters of the elastic Earth model (Vasco et al., 2010). In the study, the expert knowledge provides apriori knowledge on the spatial smoothness of the signal, as well as the deformation behavior in the area of interest.

- **Extra observations**. Extra observations can be InSAR observations from a different track/sensor (Ketelaar et al., 2007), or observations using other methods such as GPS or leveling (Odijk et al., 2003; Poland et al., 2006).

Due to the various sources and different forms of the contextual information, its utilization is usually case dependent. We propose a generic way to import the contextual information on the spatial smoothness of deformation signal into the functional model, by using it to define the cluster. More specifically, the information will define 1) the extent of a cluster; 2) the deformation model of a cluster.

The extent of a cluster

To define the extent of the area of a cluster, there are three options to extract the spatial smoothness information from the spatial smoothness information:

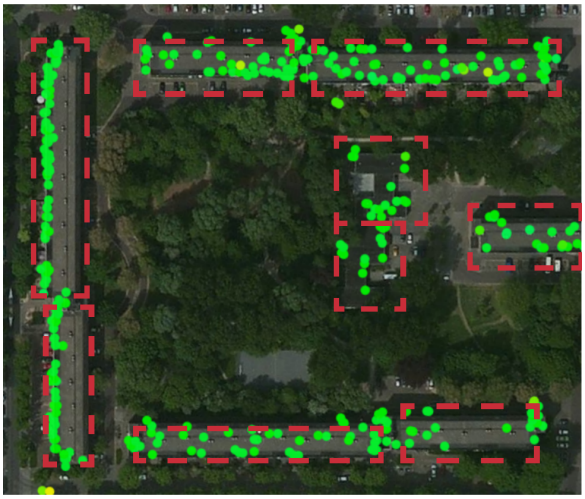

Figure 3.4: An example of the cluster defined using the Option 1. The coloured dots are the InSAR measurement points. Each red rectangle with dash lines is a cluster, which is defined based on the extent of the ground buildings. The base map provides information on the extent of the buildings, which is the contextual information in this case and directly defines the clusters. This definition is based on the expert knowledge and the experience that the same building has the same deformation driving mechanism.

Option 1. The knowledge on the extent of the ground targets is given externally. Then the extent of a cluster can be defined based on the extent of each ground target. This is based on the assumption that if the InSAR measurement points located on the same ground target, they will share the common deformation driving mechanism, and therefore be spatially correlated. As an example shown in Fig. 3.4, if the contextual information gives the extent of a building or a deformation bowl, the InSAR measurement points located on the same building or in the same deformation bowl can be grouped into the same cluster.

Option 2. An expert spatio-temporal variogram of deformation time series is given, as well as the maximum threshold of the variogram. We assume that if some InSAR measurement points are in a same cluster, the differences of their deformation should be smaller than the given threshold. Based on this assumption, we divide the area of interest into equal-size grid cells, and each grid cell is a cluster. As an example shown in Fig. 3.5, one can find the range r_{cls}

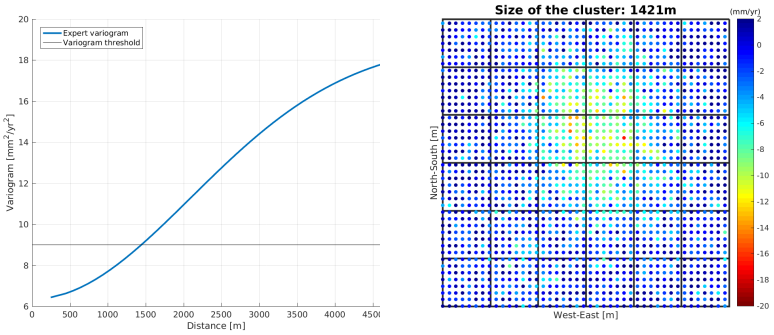

Figure 3.5: An example of the cluster defined using the Option 2. The right figure indicates the simulated 50×50 *InSAR measurement points which are evenly distributed in a* 10×10 *km area. All InSAR measurement points follow the constant velocity model. The left figure shows a given variogram of the deformation velocity. The black line in the left graph indicates the threshold of the variogram given by the contextual information, which corresponds to the spatial range* $r_{cls} = 1421$ *m. According to the information of the left figure, the right figure is divided into equal-size squared cells with the size of* 1421 *m with each squared cell is a cluster.*

corresponding to the maximum variogram threshold, and group all the InSAR measurement points in the area of interest into equal-size grid cells with the size of r_{cls}, and each grid cell will be a cluster.

Option 3. When the variogram in Option 2 is not given, but given the assumption that the deformation signal is the dominant component in InSAR observations, and the threshold of the variogram is given, then one can compute the spatio-temporal variogram of the deformation time series of all InSAR measurement points in the area of interest, and find the range r_{cls} corresponding to the maximum variogram threshold. Then we divide the area of interest into equal-size square grid cells with the length of r_{cls}, and each grid cell will be a cluster.

The extent of the cluster is defined using one of the above three options, all based on the given information on the spatial smoothness of the deformation signal. If the extent of the cluster cannot be defined using the above three options, then this means the available contextual information is not sufficient for the cluster-wise modeling. In this case, the deformation will be modeled point-wisely, as introduced in Section 3.1.

The deformation model of a cluster

There are two options to define the deformation model of a cluster, depends on the given information:

Option 1. The functional model, or several possible alternative models of a cluster, is given by the contextual information. If multiple possible models exist, the

multiple hypothesis testing method should be applied for the cluster, to select the optimal model.

Option 2. The knowledge is given that the deformation of the cluster can be described by the canonical functions introduced in Section 3.1.1. And the multiple hypothesis testing method should be applied to the cluster to select the optimal combination from the library.

The deformation model of the cluster should be given by one of the above two options. Otherwise, the cluster cannot be defined, and the deformation should be modeled pointwisely, as introduced in Section 3.1.

If the proper contextual information is given, the functional model and the stochastic model can be built for a cluster. This will be introduced in Section 3.2.2 and Section 3.2.3.

3.2.2. Functional model

Given a cluster $\mathbb{C}$, within which N InSAR measurement points $[p_1, p_2, \ldots, p_N]$ are situated, the deformation time series of all InSAR measurement points in $\mathbb{C}$ can be represented by a vector $\underline{y}$ [2], as in

$$\begin{aligned} \underline{y} &= [\underline{y}^{p_1}, \underline{y}^{p_2}, \ldots, \underline{y}^{p_N}]^T \\ &= [\underline{y}_1^{p_1}, \ldots, \underline{y}_m^{p_1}, \underline{y}_1^{p_2}, \ldots, \underline{y}_m^{p_2}, \ldots, \underline{y}_m^{p_N}]^T, \end{aligned} \tag{3.30}$$

where $\underline{y}_i^{p_j}$ with $i \in [1, m]$, $j \in [1, N]$ denotes the deformation of point p_j at the ith epoch, w.r.t. the reference epoch o and the reference point r. Here we narrow down Eq. (2.11) to the functional model of the deformation of cluster $\mathbb{C}$

$$E\{\underline{y}\} = Ax, \tag{3.31}$$

where A and x are the design matrix and unknown parameters, respectively. Eq. (3.31) is an generic expression of the functional model of the cluster $\mathbb{C}$. The structure of A and x is dependent on the definition of the cluster $\mathbb{C}$.

When pseudo observations on deformation is available, the constrained least-squares estimation (see Section 2.2.2) can be applied. Then Eq. (3.31) can be written into:

$$E\{\begin{bmatrix} \underline{y} \\ \underline{d} \end{bmatrix}\} = \begin{bmatrix} A \\ G \end{bmatrix} x, \tag{3.32}$$

where $\underline{d}$ is the vector of the pseudo observations, and G is the design matrix which defines the relation between the extra observations $\underline{d}$ and the deformation model parameters x. The extra observations d can either be the real observations from external source, or the pseudo observation defined by contextual information.

[2] In chapter 2, the vector $\underline{y}$ generally indicates the measurement vector. Here we narrow down its meaning to the deformation time series of one or more InSAR measurement points in the cluster.

The functional model, i.e. Eq. (3.31) or Eq. (3.32) defines the relation between the InSAR deformation time series and the deformation model parameters of the cluster $\mathbb{C}$. It describes the variation of deformation in both temporal and spatial domain. The structure of the functional model should be specified by the contextual information.

More than one alternative function may exist for this new functional model. This can happen when multiple possible deformation models for the cluster $\mathbb{C}$ are given, or given the knowledge that the deformation of the cluster can be described by the canonical functions introduced in Section 3.1.1. The optimal deformation model of $\mathbb{C}$ will be selected by cluster-wise MHT, which will be introduced in Section 3.2.4.

3.2.3. Stochastic model

Similar as point-wise modeling, the stochastic model of the cluster-wise modeling will also be divided into the scattering noise component and the atmospheric noise component. When building up the stochastic model for the cluster $\mathbb{C}$, the spatial correlation of noise needs to be taken into account.

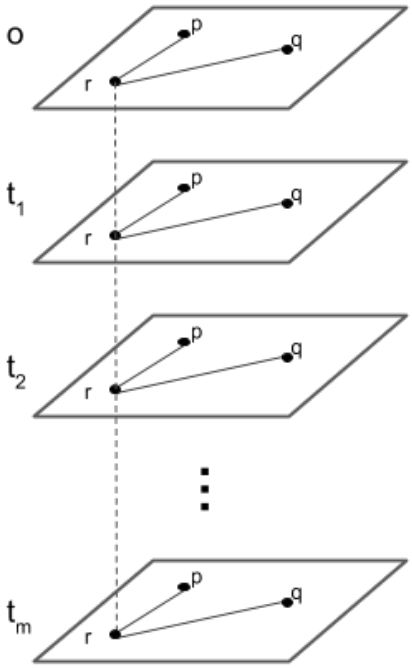

Figure 3.6: An illustration of the double difference. The InSAR deformation time series of two InSAR measurement points, i.e. p and q, are the double differences w.r.t. the same reference point r and the same reference epoch o. Due to sharing the same reference epoch/point, the noise in the deformation time series of point p and q is spatially correlated.

The definition of the spatio-temporal stochastic model of multiple InSAR measurement points has been studied(Samiei-Esfahany and Hanssen, 2013). Considering the double difference w.r.t. the reference epoch o and the reference point r, as shown in Fig. 3.6, the scattering noise component Q_{scat} is:

$$Q_{\text{scat}} = \begin{bmatrix} \sigma^2_{\text{scat}}(1o, p_1 r) & \dots & \sigma^2_{\text{scat}}(1m, p_1 p_N) \\ \vdots & \ddots & \vdots \\ \sigma^2_{\text{scat}}(m1, p_1 p_N) & \cdots & \sigma^2_{\text{scat}}(mo, p_N r) \end{bmatrix}, \tag{3.33}$$

where $\sigma^2_{\text{scat}}(ij, p_k p_l)$, $i, j \in [1, m]$ and $k, l \in [1, N]$ denotes the (co)variance of double difference caused by the scattering noise between the observation on the deformation time series of InSAR measurement points p_k at epoch i and p_l at the epochs j. The elements in Eq. (3.33) can be written into

$$\begin{aligned} \sigma^2_{\text{scat}}(io, p_k r) &= 4\sigma^2 \\ \sigma^2_{\text{scat}}(io, p_k p_l) &= 2\sigma^2 \\ \sigma^2_{\text{scat}}(ij, p_k r) &= 2\sigma^2 \\ \sigma^2_{\text{scat}}(ij, p_k p_l) &= \sigma^2 \end{aligned} . \tag{3.34}$$

Considering the double differences, the atmospheric noise component Q_{atm} is (Samiei-Esfahany and Hanssen, 2013)

$$Q_{\text{atm}} = \begin{bmatrix} \sigma^2_{\text{atm}}(1o, p_1 r) & \dots & \sigma^2_{\text{atm}}(1m, p_1 p_N) \\ \vdots & \ddots & \vdots \\ \sigma^2_{\text{atm}}(m1, p_1 p_N) & \cdots & \sigma^2_{\text{atm}}(mo, p_N r) \end{bmatrix}, \tag{3.35}$$

where $\sigma^2_{\text{atm}}(ij, p_k p_l)$, $i, j \in [1, m]$ and $k, l \in [1, N]$ denotes the (co)variance caused by the atmospheric noise. The covariance is between the InSAR observations on the deformation time series of two InSAR measurement points at two epochs: p_k at epoch i and p_l at the epochs j. The elements in Eq. (3.35) can be written into

$$\begin{aligned} \sigma^2_{\text{atm}}(io, p_k r) &= 2\sigma^2_{w_i} + 2\sigma^2_{w_o} - 2\sigma^2_{w_i} e^{(-\frac{l_{p_k r}}{L_{w_i}})} - 2\sigma^2_{w_o} e^{(-\frac{l_{p_k r}}{L_{w_o}})} \\ \sigma^2_{\text{atm}}(ij, p_k r) &= 2\sigma^2_{w_i} + 2\sigma^2_{w_j} - 2\sigma^2_{w_i} e^{(-\frac{l_{p_k r}}{L_{w_i}})} - 2\sigma^2_{w_j} e^{(-\frac{l_{p_k r}}{L_{w_j}})} \\ \sigma^2_{\text{atm}}(io, p_k p_l) &= \sigma^2_{w_i} + \sigma^2_{w_o} + \sigma^2_{w_i} e^{(-\frac{l_{p_k p_l}}{L_{w_i}})} + \sigma^2_{w_o} e^{(-\frac{l_{p_k p_l}}{L_{w_o}})} \\ &\quad - \sigma^2_{w_i} e^{(-\frac{l_{p_k r}}{L_{w_i}})} - \sigma^2_{w_o} e^{(-\frac{l_{p_k r}}{L_{w_o}})} - \sigma^2_{w_i} e^{(-\frac{l_{p_l r}}{L_{w_i}})} - \sigma^2_{w_o} e^{(-\frac{l_{p_l r}}{L_{w_o}})} \\ \sigma^2_{\text{atm}}(ij, p_k p_l) &= \sigma^2_{w_o} + \sigma^2_{w_o} e^{(-\frac{l_{p_k p_l}}{L_{w_o}})} - \sigma^2_{w_o} e^{(-\frac{l_{p_k r}}{L_{w_o}})} - \sigma^2_{w_o} e^{(-\frac{l_{p_l r}}{L_{w_o}})} \end{aligned} , \tag{3.36}$$

where $l_{p_k p_l}$ denotes the deformation between point p_k and p_l. The atmospheric decorrelation distance L_{w_i} and the variance $\sigma^2_{w_i}$ are derived from the variogram of the atmo-

spheric data at epoch i. This atmospheric data can be computed by atmospheric filtering algorithms when applying TInSAR processing (van Leijen, 2014; Samiei-Esfahany and Hanssen, 2013).

Then the stochastic model for the cluster $\mathbb{C}$ is computed by the sum of Q_{scat} and Q_{atm}

$$D\{\underline{y}\} = Q_{yy} = Q_{\text{scat}} + Q_{\text{atm}}. \tag{3.37}$$

Same as the VCM Q^p in Eq. (3.21), the effects caused by the InSAR processing on the spatial-temporal correlation are not taken into account in Q_{yy}. A Monte Carlo approach can be used to improve the apriori stochastic model (Samiei-Esfahany and Hanssen, 2013).

In this way, a spatio-temporal stochastic model for cluster $\mathbb{C}$ has been built. The spatial apriori information from InSAR data itself, i.e. the spatial correlation of noise, has been integrated into the deformation modeling.

3.2.4. Cluster-wise multiple hypothesis testing

As introduced in Section 3.2.2, based on apriori information, usually there will be more than one alternative functional model exists for the deformation of a cluster $\mathbb{C}$.Therefore one needs to select the optimal deformation model from all the alternative models. In this section, we introduce a way to select the optimal deformation model for cluster $\mathbb{C}$, using MHT method.

When the deformation of all InSAR measurement points in $\mathbb{C}$ can be represented by the same deformation model, one can use the model combinations from the library of the canonical functions to model deformation of $\mathbb{C}$, as introduced in Section 3.1.1. In this case, one can follow the point-wise MHT procedures to determine the optimal functional model.

When spatial variation exists in the deformation of $\mathbb{C}$, its functional model of deformation should be specified manually in advance, based on the apriori knowledge of the deformation properties of the area of interest. If several possible spatio-temporal deformation model exists, we use cluster-wise MHT to select the optimal model from all the potential models.

We follow the DIA procedure to perform the hypothesis testing. First we will attempt to model the deformation of $\mathbb{C}$ with the simplest deformation model. Therefore we set the the null hypothesis H_0 as a "steady state", i.e. the deformation time series of the the cluster $\mathbb{C}$ is a constant value. Several alternative hypotheses H_j's are established beside H_0, which are the predefined potential models. Without loss of generality, also considering the apriori information may also provide the knowledge on the pseudo observations, see Section 2.2.2, the mathematical expressions for H_0 and all H_j's, $\forall\, j$, are expressed as:

$$
\begin{aligned}
H_0 : E\{\begin{bmatrix} \underline{y} \\ \underline{d} \end{bmatrix}\} &= \begin{bmatrix} A_0 \\ G_0 \end{bmatrix} x_0; & D\{\begin{bmatrix} \underline{y} \\ \underline{d} \end{bmatrix}\} &= \begin{bmatrix} Q_{yy} & \\ & Q_{dd} \end{bmatrix} \\
H_j : E\{\begin{bmatrix} \underline{y} \\ \underline{d} \end{bmatrix}\} &= \begin{bmatrix} A_0 \\ G_0 \end{bmatrix} x_0 + \begin{bmatrix} C_j \\ G_j \end{bmatrix} \nabla_j; & D\{\begin{bmatrix} \underline{y} \\ \underline{d} \end{bmatrix}\} &= \begin{bmatrix} Q_{yy} & \\ & Q_{dd} \end{bmatrix},
\end{aligned} \tag{3.38}
$$

where the constant scalar x_0 indicates the constant value of deformation, and A_0 is the design matrix. A certain alternative hypothesis H_j is defined by a new design matrix C_j and a new vector of additional unknown parameters ∇_j. The stochastic model is given by the VCM Q_{yy}. The vector $\underline{d}$ is the vector of the pseudo observations. G_0 is the design matrix of the constraint for the null hypothesis H_0, and G_j is the design matrix of the constraint for an alternative hypothesis H_j. Q_{dd} is the VCM of $\underline{d}$. If the apriori information gives $\underline{d}$, it can be integrated into the cluster-wise MHT using constrained least-squares estimation introduced in Section 2.2.2.

Note that in Eq. 3.38, the vector of pseudo observations $\underline{d}$ may not always be given, since it is the information from the external sources. And $\underline{d}$ can be given only for the null hypothesis, or for some of the alternative hypothesis. E.g. if $\underline{d}$ is the velocity estimation given by external source, then it is only valid for the alternative hypotheses with a deformation velocity in ∇_j. If $\underline{d}$ is not given for H_0 or any of H_j's Eq. (3.38) can be written into its special case without constrained least-squares estimation, as

$$
\begin{aligned}
H_0 : E\{\underline{y}\} &= A_0 x_0; & D\{\underline{y}\} &= Q_{yy} \\
H_j : E\{\underline{y}\} &= A_0 x_0 + C_j \nabla_j; & D\{\underline{y}\} &= Q_{yy}.
\end{aligned} \tag{3.39}
$$

First we will apply the OMT to test whether the null hypothesis H_0 holds. The OMT follows the test statistic $\underline{T}_0$, which is

$$
\underline{T}_0 = (\underline{\hat{e}}_0)^T (Q_{yy})^{-1} \underline{\hat{e}}_0, \tag{3.40}
$$

where $\underline{\hat{e}}_0 = \underline{y} - A_0 \underline{\hat{x}}_0$ is the residual between the functional model of the null hypothesis and the observations, and $\underline{\hat{x}}_0$ is the BLUE of x_0. The decision of whether starting MHT is made by comparing $\underline{T}_0$ to a critical value:

$$
K_0 = \chi^2_{\alpha_0}(1, 0), \tag{3.41}
$$

where α_0 is the given the level of significance. Similar as the point-wise MHT, α_0 depends on the cost of making the type I error. This cost varies in different cases on the deformation modeling. In practice, we determine α_0 based on experience, or based on the given contextual information.

If H_0 is rejected, the cluster-wise MHT will be triggered to select the "optimal" model from H_j's.

To determine the optimal functional model for the spatio-temporal deformation of $\mathbb{C}$ by cluster-wise MHT, first we select out the most probable hypothesis H_b from all possible hypotheses (i.e. H_0 and H_j's).

The selection of H_b follows a test statistic $\underline{T}_j$, which is the test statistic of H_j, and computed as

$$\underline{T}_j = \underline{\hat{e}}_0^T (Q_{yy})^{-1} \underline{\hat{e}}_0 - (\underline{\hat{e}}_j)^T (Q_{yy})^{-1} \underline{\hat{e}}_j \tag{3.42}$$

where $\underline{T}_j \sim \chi^2(q_j, \lambda_j), \forall j$. The degree of freedom q_j equals to the dimension of H_j, and $\lambda_j = \lambda(\gamma, \alpha_j, q_j)$ is the degree of non-centrality of H_j. Following the conception of the B-method of testing, a uniform power of test γ is applied for all alternative hypothesis, and compute λ_j for all H_j, which is the B-method of testing introduced in Section 3.1.3.

The test statistics are normalized by dividing the corresponding critical value:

$$\underline{\mathbf{T}}_j = \frac{\underline{T}_j}{\chi^2_{\alpha_j}(q_j, \lambda_j)} \tag{3.43}$$

where $\underline{\mathbf{T}}_j$ is the test ratio of H_j. The optimal alternative hypothesis H_b is selected by the criterion

$$\underline{\mathbf{T}}_b > 1 \quad \text{and} \quad \underline{\mathbf{T}}_b = \max\{\underline{\mathbf{T}}_j\}, \forall j \tag{3.44}$$

where $\underline{\mathbf{T}}_b$ is the test ratio of H_b. When $\underline{\mathbf{T}}_b > 1$, H_b is more probable than H_0. In this way the most probable hypothesis H_b among all H_j's and H_0 are selected. When $\forall j, \underline{\mathbf{T}}_b < 1$, then no alternative hypothesis is more preferred than the null hypothesis.

3.3. Quality Control

We have presented the theory of spatio-temporal deformation modeling. After the results are required, one should also assess the quality of the estimated parameters for the validation of the results.

The quality of the estimated deformation model parameters are usually assessed by two aspects: the level of noise, and the imperfection of the model. The former is dependent on the existing noise in the InSAR measurements, while the latter relies on the selection of the deformation model we use to describe the deformation behavior. In this study, we use two indexes to assess the quality of the deformation modeling: the *precision* and the *reliability*.

3.3.1. Precision

The precision describes the consistency of the modeling results. It shows the noise influence on the final estimation of the model parameters. We can use the VCM as an indicator of the precision. According to the error propagation law, the precision of the estimated model parameters can be written as

$$Q_{\hat{x}\hat{x}} = (A^T Q_{yy}^{-1} A)^{-1}, \tag{3.45}$$

where the diagonal entries of $Q_{\hat{x}\hat{x}}$ denote the variances of the estimation of the model parameters, while the off-diagonal entries denote the covariances. A predefined threshold can be set for the variances of each parameter, and the quality of an estimation will be considered acceptable when the variance is smaller than the threshold value.

Once $Q_{\hat{x}\hat{x}}$ is derived, the precision of the adjusted deformation observations $\underline{\hat{y}} = A\underline{\hat{x}}$ reads

$$Q_{\hat{y}\hat{y}} = AQ_{\hat{x}\hat{x}}A^T \tag{3.46}$$

and the VCM of the estimations of residuals reads

$$Q_{\underline{\hat{e}}\underline{\hat{e}}} = Q_{yy} - Q_{\hat{y}\hat{y}} \tag{3.47}$$

where $\underline{\hat{e}} = y - \underline{\hat{y}}$ are the residuals.

3.3.2. Reliability

The precision only assesses the consistency of the estimated parameters, but it is not sensitive to the imperfection of the deformation model itself. The concept of reliability is introduced to describe the model misspecification, which can be detected with a discriminatory power γ. In this study, we introduce the *Minimal Detectable Value* (MDV) (Teunissen, 1998) as an indicator of the reliability.

The MDV specify an additional parameter that should be included in the functional model. Suppose we already decide to model the deformation of a cluster $\mathbb{C}$ with mathematical model model $H_0 : E\{\underline{y}\} = Ax,\ D\{\underline{y}\} = Q_{yy}$, then the alternative model is

$$H_j : \underset{mN\times 1}{E\{\underline{y}\}} = \underset{mN\times n}{A}\ \underset{n\times 1}{x} + \underset{mN\times q}{C}\ \underset{q\times 1}{\nabla} \qquad D\{\underline{y}\} = Q_{yy}, \tag{3.48}$$

where ∇ is a vector with dimension q, representing the additional parameters under the alternative hypothesis H_j, i.e. the imperfection of the model. To assess the imperfection of a given model specified by H_0, an important value to consider is the minimum value of the additional parameters ∇, which is detectable with a fixed discriminatory power γ. We refer to this minimal value as the *Minimal Detectable Value*, represented by ∇_{MDV}.

The MDV describes how significant a certain additional parameter in an alternative hypothesis is, under a certain discriminatory power γ. With a fixed discriminatory power γ, the true (but unknown) additional parameter is larger than ∇_{MDV}, we can state that this parameter is detectable with the discriminatory power γ.

From the perspective of γ, if we set γ to a high value, this means we only decide to accept the model imperfection only with a high certainty. As a result, we can only detect it when its value is high.

When the dimension of additional parameters $q = 1$, this means the design matrix C in Eq. (3.48) reduces to an $m \times 1$ vector c, and ∇ reduces to a scalar. Then the MDV can

be found as (Teunissen, 2000a)

$$|\nabla_{\underset{1\times1}{MDV}}| = \sqrt{\frac{\lambda(\gamma,\alpha,q)}{c^T Q_{yy}^{-1} Q_{\underline{\hat{e}}\underline{\hat{e}}} Q_{yy}^{-1} c}}, \tag{3.49}$$

where $|\nabla_{MDV}|$ is the MDV of ∇, The VCM $Q_{\underline{\hat{e}}\underline{\hat{e}}}$ is the VCM of the residuals as in Eq. (3.47). The operator λ derives the non-centrality parameter via a given discriminatory power γ, the level of significance α and the dimension q.

When $q > 1$, ∇ becomes a vector instead of a scalar. To derive the MDV, we can consider ∇ as an q dimension vector and re-parametrize ∇ as in (Teunissen, 2000a)

$$\underset{q\times1}{\nabla} = \underset{1\times1}{||\nabla||}\ \underset{q\times1}{d}, \tag{3.50}$$

where $||\nabla||$ is an scalar indicates the length (Euclidean norm) of vector ∇, with the unit vector d varying in all dimensions. Then the MDV of ∇ can be represented as:

$$||\nabla_{\underset{1\times1}{MDV}}|| = \sqrt{\frac{\lambda_0}{d^T C^T Q_{yy}^{-1} Q_{\underline{\hat{e}}\underline{\hat{e}}} Q_{yy}^{-1} C d}}, \tag{3.51}$$

where the vector d moves through a circle when $q = 2$, an sphere when $q = 3$, and a hypersphere when $q > 3$.

3.4. Procedures of spatio-temporal deformation modeling

To describe the deformation behavior of the area of interest, we proposed two methods to parameterize the deformation behavior with spatio-temporal deformation models, i.e. the point-wise deformation modeling, as introduced in Section 3.1 and the cluster-wise modeling, as introduced in Section 3.2. The former method models only the temporal deformation behavior per InSAR measurement point, the later method models the deformation behavior in both spatial and temporal domain. The choice between the two methods depends on the level of the spatial smoothness information. In Section 3.3 the quality control method has been introduced. In this section we introduce the generic procedures based on the theory introduced in Section 3.1-3.3 of spatio-temporal deformation modeling, see also Fig. 3.7.

Step 1. Based on the available InSAR deformation time series of all InSAR measurement points, and the available spatial smoothness information, define the cluster $\mathbb{C}$. To define $\mathbb{C}$, 1) the extent of $\mathbb{C}$ and 2) the deformation model(s) of $\mathbb{C}$ should be defined.

Step 2. Apply cluster-wise deformation modeling for all clusters, as introduced in Step 3-4. For the InSAR measurement points not in any cluster, apply point-wise deformation modeling per InSAR measurement point, as introduced in Step 5-6.

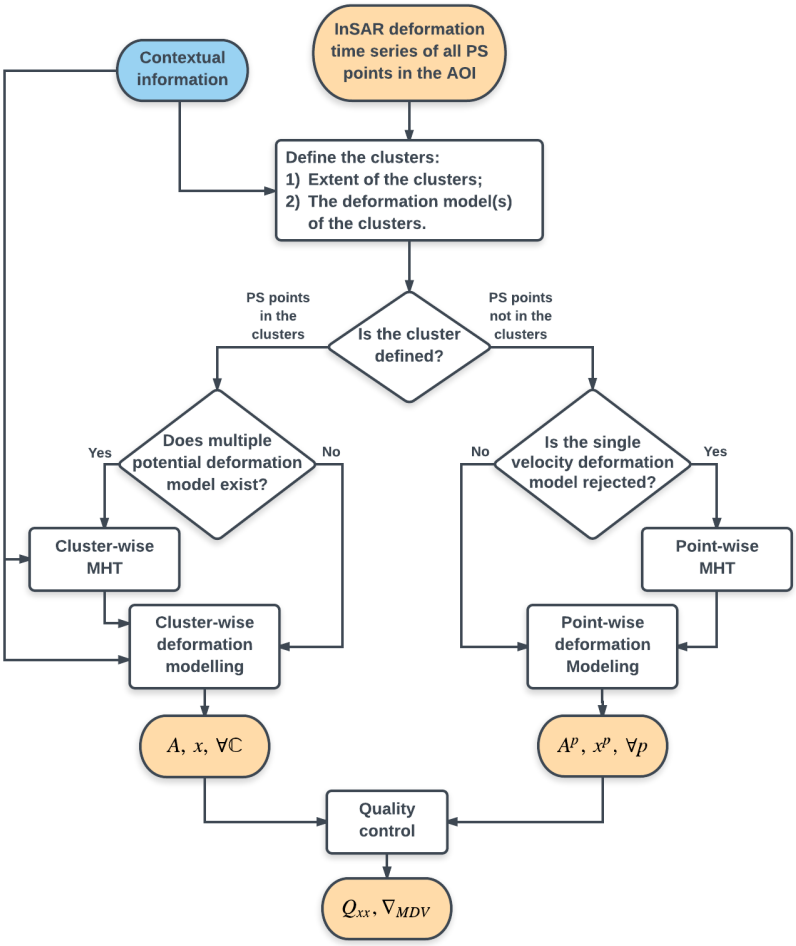

Figure 3.7: The flowchart of spatio-temporal deformation modeling.

Step 3. For each cluster $\mathbb{C}$, if multiple possible deformation models exist, the optimal deformation model should be selected using cluster-wise MHT, as introduced in Section 3.2.

Step 4. Build the functional model and stochastic model for each $\mathbb{C}$. Estimate the deformation model parameters x.

Step 5. For the InSAR measurement points not in any cluster, their deformation behavior will be modeled using point-wise deformation modeling method. For each InSAR measurement point p, first the OMT is applied to test the validity of the constant velocity model for each InSAR measurement point. If rejected,

then the optimal deformation model will be selected using point-wise MHT, from the combinations of the library of canonical functions.

Step 6. Build the functional model and stochastic model for each InSAR measurement point p. Estimate the deformation model parameters x^p.

Step 7. Assess the quality of the deformation modeling. Compute the VCM $Q_{\hat{x}\hat{x}}$ to assess the precision, and the minimal detectable value ∇_{MDV} to assess the reliability.

The spatial-temporal deformation behavior of the area of interest will either be described by the deformation model of the clusters, or the deformation model of every InSAR measurement point. The application of spatial-temporal deformation modeling on data will be presented in Chapter 4 and Chapter 5.

4

Application on Simulated Data

In this Chapter, we demonstrate the possibility of spatio-temporal deformation modeling using simulated InSAR deformation time series. We simulate the time-series InSAR measurements on a deformation bowl, polluted by simulated atmospheric noise and scattering noise. Both point-wise deformation modeling and cluster-wise deformation modeling are applied on the simulated data, see Section 3.1 and Section 3.2. Since the actual deformations are known in simulation, we compare the modeling results with actual deformation signal to assess the performance of deformation modeling.

Section 4.1 introduces the simulation of InSAR data used in this chapter. Section 4.2 presents the application of point-wise deformation modeling on the simulated data. Section 4.3 focuses on the application of cluster-wise deformation modeling, given different types of contextual information.

4.1. Description of simulated data

We simulate the InSAR deformation time series of 10^4 InSAR measurement points, uniformly distributed in an area with a size of 10×10 kilometers. For each point, we simulate the InSAR measurements on 49 acquisitions, with an 11-day repeat cycle. The deformation of the area of interest (AoI) shows a deformation bowl in space. such a spatial deformation pattern is often observed in an area where the deformation is driven by hydrocarbon production or ground water extraction (Yerkes and Castle, 1969; Ketelaar et al., 2007; Bell et al., 2008).

To simplify the problem, we assume the orbit error and topography component in the InSAR observations are already properly removed, and the phase unwrapping is properly performed. Also, we assume no atmospheric filtering is applied. Then we only consider three major components in the InSAR observations: deformation signal, scattering noise, and atmospheric noise (Hanssen, 2001a). We first simulate the three components on each acquisition. Then based on the simulated acquisitions, we compute the InSAR measurements over the AoI. Each acquisition has a size of 100×100 pixels. All pixels will be selected as InSAR measurement points.

The simulated deformation signal in all acquisitions is shown in Fig. 4.1. The center

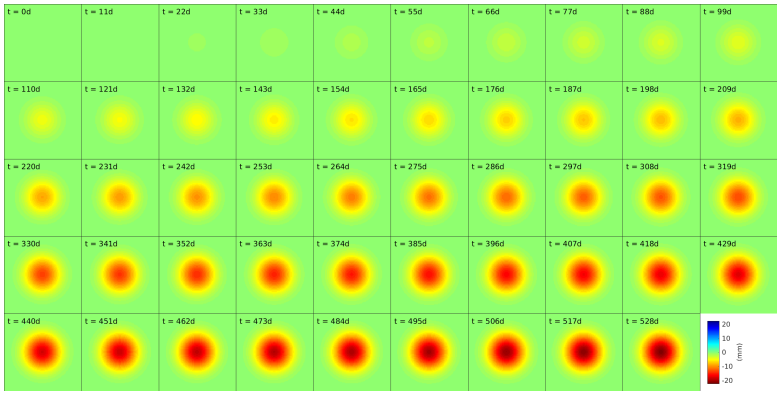

Figure 4.1: Simulated actual deformation 49 acquisitions over an 10×10 km AoI, with an 11-day temporal resolution. The deformation time series show as a deformation bowl. The center of this deformation bowl locates on the center of the AoI. The temporal and spatial behavior of the deformation are given in Eqs. (4.1) and (4.2). For the first acquisition in the stack we assume there is no deformation.

of deformation bowl locates at the center of the AoI. The deformation time series of the deformation bowl center follows

$$z(p_c, t_i) = v^{p_c} B_{t_i}, \tag{4.1}$$

where $z(p_c, t_i)$ is the deformation of p_c at epoch t_i. p_c is the center point of the deformation bowl. v^{p_c} is the deformation velocity of point p_c. B_{t_i} is the time at epoch t_i w.r.t. the first epoch, i.e. the temporal baseline. It is assumed no deformation exists at the first epoch t_0 and the subsidence bowl center p_c locates at the center of the AoI. We set $v^{p_c} = 15$ mm/yr.

In spatial domain, the actual deformation time series follows a Gaussian function as

$$z(p, t_i) = z(p_c, t_i) \exp(-\kappa \frac{d^2}{L^2}), \tag{4.2}$$

where $z(p, t_i)$ is the actual deformation time series of point p. The distance d is the distance between p and the deformation bowl center p_c, and L is the decorrelation range. The κ is the coefficient. Here $L = 2$ km and $\kappa = 0.8$.

For all points, their actual deformation time series have constant velocities. From the center to the edge of the AoI, the deformation velocities gradually decrease. This spatial decreasing follows a Gaussian function, which can be derived from Eqs. (4.1) and (4.2), as

$$v^p = v^{p_c} \exp(-\kappa \frac{d^2}{L^2}), \tag{4.3}$$

where v^p is the deformation velocity of point p.

The noise is simulated for every acquisition. Following Section 3.1.2 and Section 3.2.3, we assume that the scattering noise follows the normal distribution, as in

$$\underline{n}_{\text{scat}}(p, t_i) \sim N(0, \sigma_s^2), \tag{4.4}$$

where $\underline{n}_{\text{scat}}(p, t_i)$ represents the scattering noise p at epoch t_i, and σ_s is the standard deviation of the scattering noise. Then the simulated scattering noise is shown in Fig. 4.2.

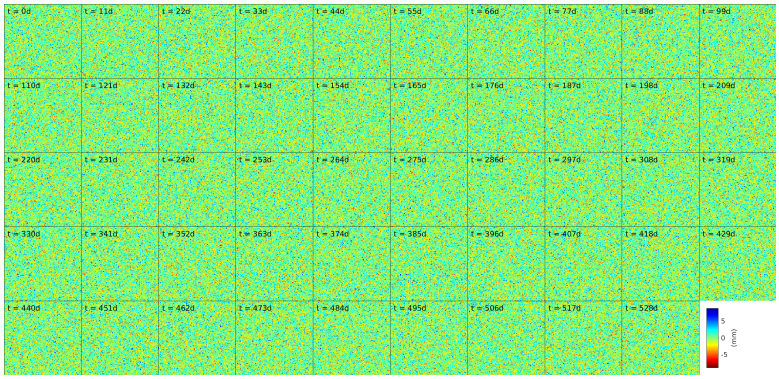

Figure 4.2: Simulated time series of the scattering noise of each acquisition. The scattering noise is assumed to follow a normal distribution as $\underline{n}_{scat}(p, t_i) \sim N(0, \sigma_s^2)$.

The atmospheric signal is simulated following the "power law" behavior (Goldstein, 1995; Ferretti et al., 1999b; Hanssen, 2001b). According to the power law, the 2-D power spectrum of the atmospheric signal can be described by three regimes, depending on the wavelength of the atmospheric signal, as in

$$\underline{P}_W^{t_i}(\lambda) = \begin{cases} \underline{P}_0^{t_i} \lambda^{\underline{\beta}_1} & \text{for } \lambda \geq 2 \text{ km} \\ \underline{P}_0^{t_i} \lambda^{\underline{\beta}_2} & \text{for } 0.5 \text{ km} \leq \lambda < 2 \text{ km} \\ \underline{P}_0^{t_i} \lambda^{\underline{\beta}_3} & \text{for } 0.01 \text{ km} \leq \lambda < 0.5 \text{ km}, \end{cases} \tag{4.5}$$

where $\underline{P}_W^{t_i}(\lambda)$ is the power density of the atmospheric. $\underline{P}_W^{t_i}(\lambda)$ is a function of the wavelength λ and $\underline{P}_0^{t_i}$ is the power density where the wavelength $\lambda = 1$ km. Three exponents $\underline{\beta}_1$, $\underline{\beta}_2$ and $\underline{\beta}_3$ respectively denote the steep power exponents of three regimes where $\lambda \geq 2$ km, $0.5 \text{ km} \leq \lambda < 2$ km and $0.01 \text{ km} \leq \lambda < 2$ km. The empirical values of the three steep power exponents are respectively suggested by InSAR observations as 8/3, 11/3 and 5/3 (Hanssen, 2001b). For a better representation of the reality, we set $\underline{P}_0^{t_i}$, $\underline{\beta}_1$, $\underline{\beta}_2$ and $\underline{\beta}_3$ to be stochastic instead of deterministic. The power density $\underline{P}_0^{t_i}$ follows a Gaussian distribution as

$$\begin{aligned} \underline{P}_0^{t_i} &\sim N(E\{\underline{P}_0^{t_i}\}, \sigma_{P_0}^2) \\ E\{\underline{P}_0^{t_i}\} &= 15 + 15 \cdot \sin(\frac{t_i}{365}\pi), \end{aligned} \tag{4.6}$$

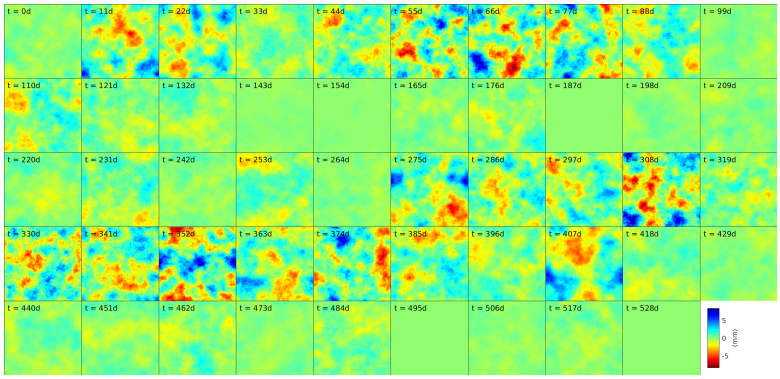

Figure 4.3: Simulated time series of atmospheric delay screens. In total 49 screens are simulated, following the three-regime power-law. The overall power of the simulated atmospheric signal shows a seasonal variation as in Eq. (4.6), with three power exponents following Gaussian distribution as in Eq. (4.7)

.

where the expectation of $\underline{P}_0^{t_i}$, i.e. $E\{\underline{P}_0^{t_i}\}$ is a sinusoid function of the time t_i. The unit of $E\{\underline{P}_0^{t_i}\}$ and t_i are respectively mm^2 and day. The variance of $\underline{P}_0^{t_i}$ is set to be 5 mm^2. Using Eq. (4.6) we give a seasonal variation of the scale of the atmospheric signal.

The steep power exponents $\underline{\beta}_1$, $\underline{\beta}_2$ and $\underline{\beta}_3$ of the three regimes follow a Gaussian distribution as:

$$\begin{aligned} \underline{\beta}_1 &\sim N(\frac{8}{3}, \frac{1}{6}) \\ \underline{\beta}_2 &\sim N(\frac{11}{3}, \frac{1}{6}) \\ \underline{\beta}_3 &\sim N(\frac{5}{3}, \frac{1}{6}). \end{aligned} \tag{4.7}$$

Using Eqs. (4.6) and (4.7), we simulate the power spectrum of the atmospheric signal for each acquisition, and compute the atmospheric signal using the inverse Fourier Transform, expressed as

$$\underline{n}_{\text{atm}}(t_i) = \mathscr{F}^{-1}(\underline{P}_W^{t_i}), \tag{4.8}$$

where $\mathscr{F}^{-1}(\cdot)$ indicates the inverse Fourier Transform operation. The atmospheric screen at epoch t_i, i.e. $\underline{n}_{\text{atm}}^{t_i}$ are shown in Fig. 4.3. In this way all atmospheric signal of 49 acquisitions are simulated. Then we select all pixels as InSAR measurement points. The sub-pixel positioning is not applied, and we simply use the center of the pixel as the position of InSAR measurements points. We select the first acquisition of the stack as the master image, and select the point at the up-left corner as the reference point. Then the

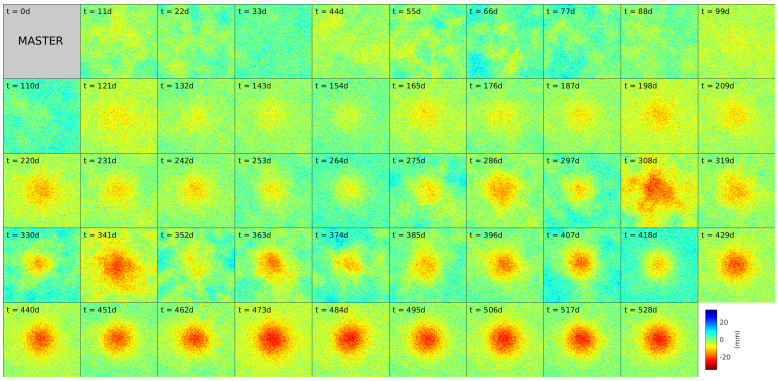

Figure 4.4: Simulated time series of InSAR deformation observations, with 100 × 100 InSAR measurement points evenly covering the 10 × 10 km area. The points are visualized as pixels here. In total 48 epochs are simulated from 49 acquisitions. All the deformation time series are the double differences w.r.t the first epoch and the InSAR measurement point at the up-left corner. No sub-pixel positioning is applied.

double-differenced InSAR deformation time series can be computed as

$$\begin{aligned}\underline{y}(p,t_i) =& [z(p,t_i) - z(p,t_0)] - [z(r,t_i) - z(r,t_0)] \\ &+ [\underline{n}_{\text{scat}}(p,t_i) - \underline{n}_{\text{scat}}(p,t_0)] - [\underline{n}_{\text{scat}}(r,t_i) - \underline{n}_{\text{scat}}(r,t_0)] \\ &+ [\underline{n}_{\text{atm}}(p,t_i) - \underline{n}_{\text{atm}}(p,t_0)] - [\underline{n}_{\text{atm}}(r,t_i) - -\underline{n}_{\text{atm}}(r,t_0)]\end{aligned} \tag{4.9}$$

where $\underline{y}(p,t_i)$ is the double-differenced InSAR observation of the InSAR measurement point p at epoch t_i, w.r.t the reference point r and the reference epoch t_0. Fig. 4.4 shows the simulated InSAR observations. In Section 4.2 and Section 4.3, we will apply point-wise and cluster-wise deformation modeling to the simulated data. Since the deformation and noise component are known, we can easily build up a stochastic model, and compare the modeling results with the actual deformation time series.

4.2. Point-wise deformation modeling

In this section we apply the point-wise deformation model to the simulated InSAR deformation time series.

By definition in Eqs. (4.1) and (4.1), the deformation of all InSAR measurement points is a linear function of time, i.e. they follow the constant velocity model. The actual deformation velocities of all InSAR measurement points can be computed by Eq. (4.3), shown in Fig. 4.5.

In this simulation, as introduced in Section 4.1, it is already known by definition that the actual deformation model of all InSAR measurement points are constant velocity model, therefore, when applying the point-wise modeling, we will not focus on select-

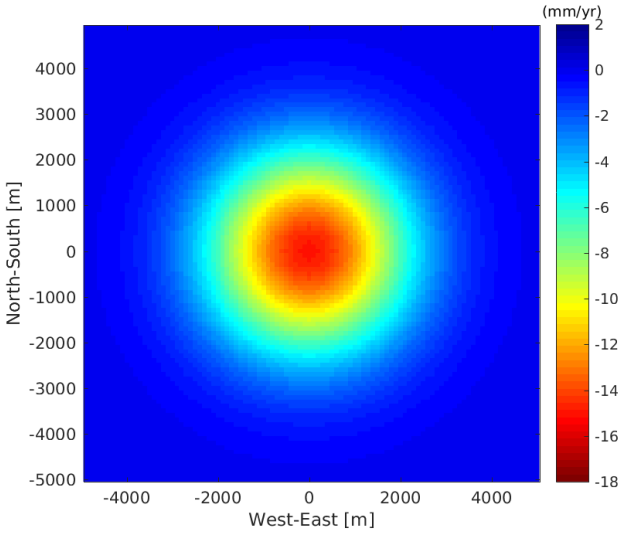

Figure 4.5: Velocity map of the actual deformation of all InSAR measurement points, computed following Eq. (4.3). By definition every InSAR measurement point in the simulation should follow a constant velocity deformation model.

ing the optimal model for each InSAR measurement point, but focus on assessing the accuracy of estimated velocity of each InSAR measurement point.

The functional model of the point-wise modeling can be built up following the approach in Section 3.1.1, with all InSAR measurement points following a constant velocity model.

We use two alternative ways to define the stochastic model, resulting in two scenarios of the results:

- **Scenario A**: Using Eq. (3.13), we consider all InSAR measurements of all points and all epochs to be independent from each other. Then we build the stochastic model with a cofactor matrix $R_{yy} = I$, and a variance of unit weight $\sigma^2_{\text{VUW}} = 36\ \text{mm}^2$.
- **Scenario B**: Using Eqs. (3.14) to (3.21), we take into account the (known) scattering noise and atmospheric noise, and build up the stochastic model. Also, we take into account the double-difference effect, therefore the temporal correlation exists between epochs due to sharing the same reference epoch. The spatial correlation will not be considered in point-wise deformation modeling.

Here we illustrate the structure of the stochastic model for the selected 6 points, see Fig. 4.6. In Scenario A, the stochastic model is a diagonal VCM, with all diagonal elements equal to the variance of unit weight, i.e. $\sigma^2_{\text{VUW}} = 36\ \text{mm}^2$. In Scenario B, the scattering noise and atmospheric noise is taken into account. Then the diagonal of the VCM

will not be the same value. The temporal correlation exists between epochs.

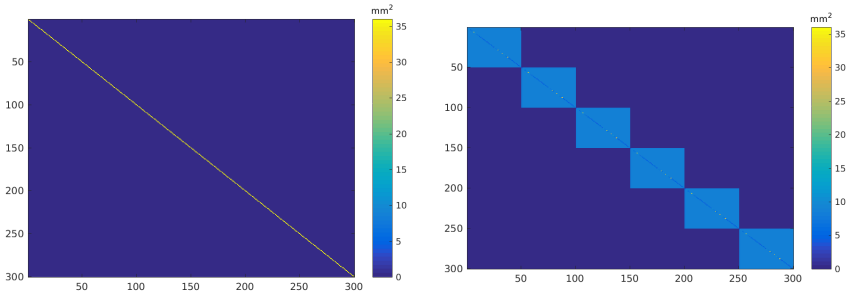

Figure 4.6: An visualization of VCMs of deformation time series of 6 *InSAR measurement points. Left: the VCM built up following Scenario A, where the VCM is a diagonal matrix, with all diagonal elements equal to* $\sigma^2_{VUW} = 36\ mm^2$*. Right: the VCM built up following Scenario B, where the off-diagonal matrix elements are not all zero. The diagonal elements are different, due to different atmospheric signal at each epoch. The temporal correlation exists between epochs of the same InSAR measurement point. The correlation between the InSAR measurement points are ignored in the point-wise deformation modeling.*

The estimated deformation velocities for Scenarios A and B are shown in Fig. 4.7.

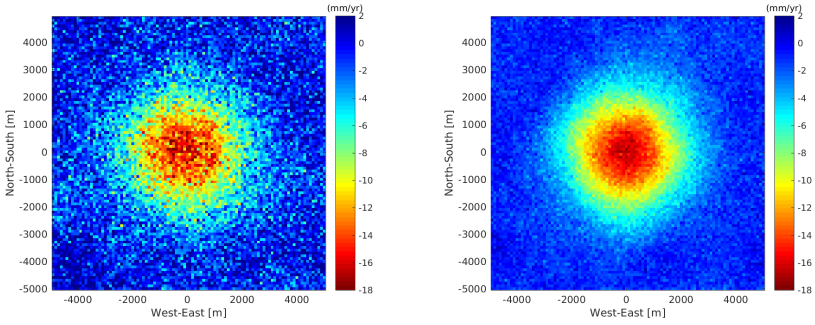

Figure 4.7: Estimated deformation velocity maps. Left: the estimated deformation velocity map for Scenario A, where a diagonal VCM with all diagonal element equal to $\sigma^2_{VUW} = 36\ mm^2$ *is used as the stochastic model. Right: the estimated deformation velocity map for Scenario B, where the atmospheric noise and scattering noise are taken into account.*

We assess the performance of the point-wise deformation modeling by comparing the estimated velocity map with the real velocity map in Fig. 4.5. Figs. 4.8a and 4.8b show the differences between the estimated deformation velocity maps and the actual deformation velocity map. The RMS values are 2.14 mm/yr and 1.16 mm/yr, respectively. Fig. 4.8b, i.e. the estimated velocities for Scenario B, have smaller differences than the results for Scenario A.

In Fig. 4.8b spatial patterns exist. These patterns are expected to be caused by the

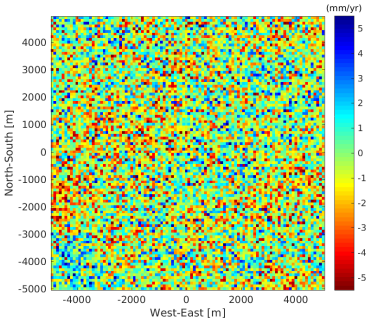

(a) Differences between Scenario A and the real velocity.

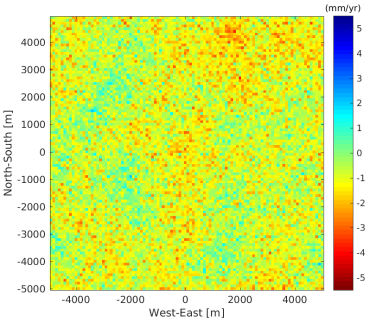

(b) Differences between Scenario B and the real velocity.

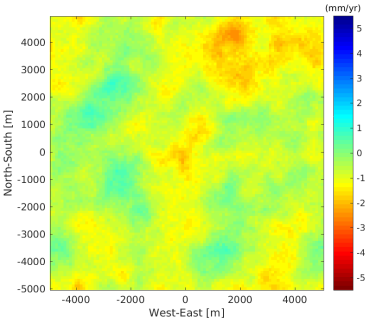

(c) Deformation velocity estimated from atmospheric double-differenced time series.

Figure 4.8: The differences of the estimated velocity map and the actual deformation signal. (a): the differences between the results for Scenario A and the actual deformation velocity map, with an RMS of 2.14 *mm/yr; (b): the differences between the results for Scenario B and the actual deformation velocity map, with an RMS of* 1.16 *mm/yr; (c): the deformation velocity estimated only from the atmospheric double-differenced time series. Figs. (b) and (c) have a correlation of* 0.46*;*

atmosphere residuals in the deformation velocity estimations, because the stochastic model in point-wise deformation modeling does not specify the correlation between the InSAR measurement points, while the atmospheric signal shows the spatial correlation. To investigate this, we compute the time series of the double-difference atmospheric signal based on the atmospheric delay time series shown in Fig. 4.3, w.r.t. the first epoch and the up-left point. Using this double-difference atmospheric signal, we estimate a linear velocity map purely from the double-differenced atmospheric signal, as shown in Fig. 4.8c. Then we compare Fig. 4.8b with Fig. 4.8c, and find a correlation of 0.46 between them. According to such a relatively high correlation, we conclude that the ignorance of spatial correlation in the stochastic model of the point-wise deformation modeling leads to the residuals of the atmospheric signal in the estimated deformation model parameters.

4.3. Cluster-wise deformation modeling

Following the instructions in Section 3.2, we apply the cluster-wise deformation modeling to the simulated deformation time series. Based on different levels of available information on the spatial smoothness of deformation signal, the cluster-wise deformation modeling is applied following two scenarios:

- **Scenario A**: the area is divided into four rings, as shown in Fig. 4.9, each ring is defined as a cluster. For each ring, a deformation velocity is given before hand. Then we use the constrained least-squares estimation as introduced in Section 2.2.2 to estimate the deformation velocities of each ring.

- **Scenario B**: the entire AoI is defined as a cluster, and provides four alternative models to describe the deformation. The cluster-wise MHT will be applied to select the optimal model from all the alternatives. This scenario simulates the scene that a domain expert has a request to describe the deformation of the AoI with a geological model, and offers the possible models.

The results for Scenario A will be presented in Section 4.3.1. The results for Scenario B will be presented in Section 4.3.2.

4.3.1. Scenario A: constrained least-squares estimation

In Scenario A of cluster-wise modeling, we assume that a domain expert provides the apriori estimation of the deformation velocity over the AoI. We build up this apriori knowledge base on the known actual deformation signal as shown in Fig. 4.1. Based on the given apriori knowledge, the AoI is divided into four rings, as shown in Fig. 4.9. All four rings are centered at the center of the AoI, i.e. the center of the deformation bowl. The properties of the four rings are listed below:

- Ring 1: with the distance to the center > 2000 m. The given deformation velocity from contextual information is 0 mm/yr, with a variance of 1.2 mm^2/yr^2.

- Ring 2: with the distance to the center from 1000 m to 2000 m. The given deformation velocity from contextual information is -6 mm/yr, with a variance of 24.3 mm^2/yr^2.

- Ring 3: with the distance to the center from 500 m to 1000 m. The given deformation velocity from contextual information is -12 mm/yr, with a variance of 7.1 mm^2/yr^2.

- Ring 4: with the distance to the center < 500 m. The given deformation velocity from contextual information is -14.4 mm/yr, with a variance of 0.8 mm^2/yr^2.

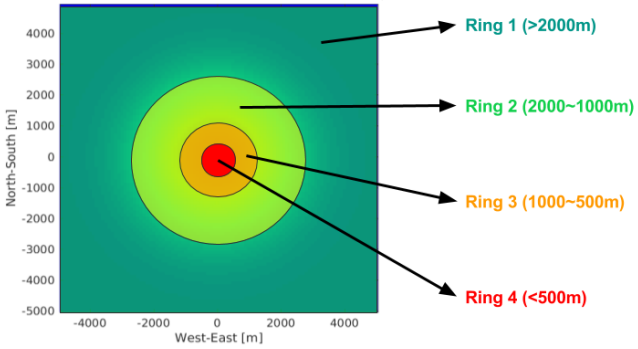

Figure 4.9: Four rings defined by the contextual information. All four rings are centered at the center of AoI. Four apriori estimated velocities are given to the four rings by contextual information, which are 0 mm/yr, −6 mm/yr, −12 mm/yr and −14.4 mm/yr respectively for Ring 1 to Ring 4. The variance of the four velocities are 1.2 mm^2/yr^2, 24.3 mm^2/yr^2, 7.1 mm^2/yr^2 and 0.8 mm^2/yr^2 respectively. The velocities are computed from the average real velocity of each ring, and the variances is derived from the variances of the real velocity of each ring.

The given apriori velocities are derived from the mean actual deformation velocities of each ring, which will be unknown in reality. The variances of the velocities are equal to the variance of actual velocities of each ring. Together they are introduced into the functional model and the stochastic model of the constraint part. Then for each ring, the functional model for the cluster-wise deformation modeling can be written as

$$E\{\begin{bmatrix}\underline{y}\\ \underline{d}\end{bmatrix}\} = \begin{bmatrix}A\\ G\end{bmatrix} x = \underbrace{\begin{bmatrix} B_{t_1} & & \\ B_{t_2} & & \\ \vdots & & \\ B_{t_{48}} & & \\ & \ddots & \\ & & B_{t_1} \\ & & \vdots \\ & & B_{t_{48}} \\ 1 & & \\ & \ddots & \\ & & 1 \end{bmatrix}}_{(49n_{\text{ring}})\times n_{\text{ring}}} \underbrace{\begin{bmatrix} v_1 \\ \vdots \\ v_{n_{\text{ring}}} \end{bmatrix}}_{n_{\text{ring}}\times 1}, \tag{4.10}$$

where the observation $\underline{y}$ is an $48n_{\text{ring}} \times 1$ vector denoting the InSAR deformation time series of all InSAR measurement points at all epochs, where n_{ring} is the number of InSAR measurement point in the ring. The pseudo observations $\underline{d}$ is an $n_{\text{ring}} \times 1$, with all elements equal to the apriori estimated velocity. B_{t_i} is the temporal baseline at epoch t_i,

w.r.t. the reference epoch. The unknown parameter vector $x = [v_1, v_2, \ldots, v_{n_{\text{ring}}}]$ are the deformation velocities of all InSAR measurement points in the ring, i.e. the cluster. In Eq. (4.10), each ring is defined as a cluster, and its deformation model is represented by the separated deformation velocities of all InSAR measurement points in the cluster.

The stochastic model is defined as

$$D\{\begin{bmatrix} \underline{y} \\ \underline{d} \end{bmatrix}\} = \begin{bmatrix} Q_{yy} & 0 \\ 0 & Q_{dd} \end{bmatrix}, \tag{4.11}$$

where Q_{dd} is the VCM of the pseudo observations, which is a diagonal matrix with the diagonal elements equal to the variance of the apriori estimated velocity. Q_{yy} is the VCM of the InSAR observations, which is defined following Section 3.2.3. We define the spatial correlation only exists within the distance of 1 km, c.f. Cuenca et al. (2011). We select 6 InSAR measurement points as shown in Fig. 4.7, and visualize the VCM of InSAR deformation time series of these InSAR measurement points, shown in Fig. 4.10

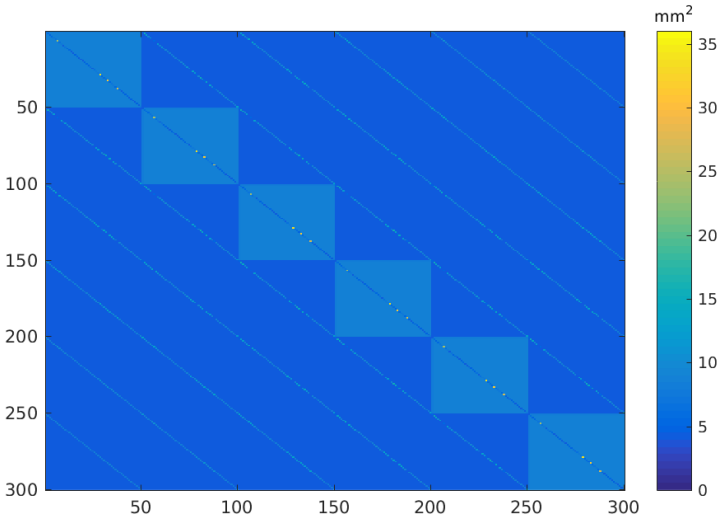

Figure 4.10: The VCM of the deformation time series of 6 *InSAR measurement points. Considering spatio-temporal correlation. To make the size of VCM manageable, we define the spatial correlation only exists within the distance of* 1 *km.*

Then for each ring, its deformation model parameters are estimated using Eq. (2.21). Then the cluster-wise modeling results into estimating the deformation velocities of all InSAR measurement points, but taking into account the spatio-temporal correlation. The results are shown in Fig. 4.11.

In Fig. 4.11b, traces of the four predefined rings can be found. This indicates that the given spatial smoothness information, which defines the extent and the deforma-

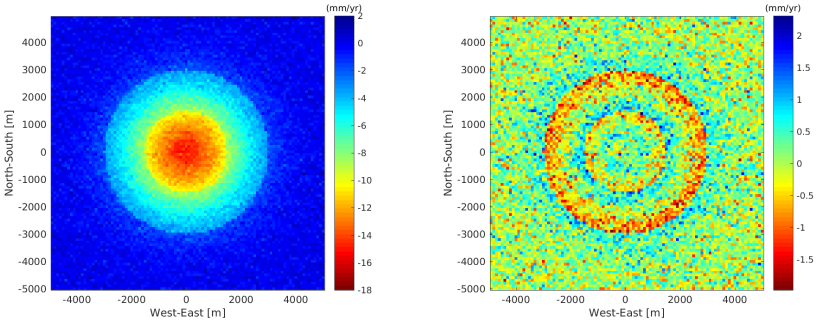

(a) Deformation velocity map estimated from Scenario A.

(b) Differences of estimated velocity map to the real velocity map.

Figure 4.11: The results of the cluster-wise deformation modeling for Scenario A. (a): the estimated deformation velocity map. (b) the differences of the estimated deformation velocity map and the actual deformation velocity map. The effect of the four pre-defined rings can be found in (b). The RMS of (b) is 0.76 mm/yr.

tion model of the four clusters, are stringent but not reliable. It constrains the deformation velocity of each ring to a single value, which may not be representative to all the InSAR measurement points in the cluster. As the result, the estimated velocity may be constrained to a value close to the real value, because the spatial smoothness is given based on the actual deformation map. However, the differences to the actual velocity map show the artificial traces due to the too stringent contextual information.

4.3.2. Scenario B: cluster-wise MHT

In Scenario B of the cluster-wise modeling, we assume that a domain expert proposes four possible deformation model to describe the spatio-temporal deformation in the AoI. The entire AoI is defined as a cluster, and the deformation model of the cluster is given, i.e. the four possible deformation models. Based on the simulated measurements, the optimal deformation model can be selected.

Following the instructions of Section 3.2.4, we use the cluster-wise MHT to select the optimal deformation model. The null hypothesis and four alternative hypotheses are established using Eq. (3.39), where $\underline{y}$ is the vector of the deformation time series of all InSAR measurement points in the AoI. The stochastic model Q_{yy} is built up following the instructions in Section 3.2.3. The alternative hypotheses H_j, $j \in [1,4]$ are alternative hypotheses given by the contextual information. No pseudo observations are given, therefore $\underline{d}$, G and Q_{dd} are empty.

The four alternative hypotheses give the functions describing the spatio-temporal deformation $\underline{y}(p,t_i)$, which represent the deformation of an InSAR measurement point p at epoch t_i. We assume the deformation of the AoI can be represented by a deformation bowl centered at the center of AoI for the four alternatives. The shapes of deformation bowls of the four alternatives are different. The four functions given by alternative

hypotheses are:

- **The Gaussian model:**

$$H_1 : \underline{y}(p,t_i) = v_c \exp(-\kappa \frac{d_p^2}{L_g^2}) B_{t_i}, \tag{4.12}$$

  which is the model that the actual deformation signal follows. d_p is the distance of the InSAR measurement point p to the center of the AoI, and B_{t_i} is the temporal baseline at the epoch t_i. The unknown parameters to be estimated are the center deformation velocity v_c, the exponent coefficient κ, and the correlation length L_g.

- **The exponential model:**

$$H_2 : \underline{y}(p,t_i) = v_c \exp(-\iota \frac{d_p^2}{L_e}) B_{t_i}, \tag{4.13}$$

  where the unknown parameters are the center deformation velocity v_c, the exponent coefficient ι, and the correlation length L_e.

- **The quadratic model:**

$$H_3 : \underline{y}(p,t_i) = a d_p^2 B_{t_i} + b d_p B_{t_i} + v_c B_{t_i}, \tag{4.14}$$

  where the unknown parameters are the polynomial coefficients a, b and the center deformation velocity v_c.

- **The linear model:**

$$H_4 : \underline{y}(p,t_i) = k d_p B_{t_i} + v_c B_{t_i}, \tag{4.15}$$

  where the unknown parameters are the gradient k and the center deformation velocity v_c.

Note that among all four alternative hypotheses, H_1 and H_2 are not linear. Therefore the linearization should first be applied based on Taylor's theorem (Taylor, 1717).

According to the test strategy, see Section 3.2.4, the OMT is first applied to test whether the null hypothesis H_0 holds. We use initially define the level significance α as 0.05. This is a relatively large α since we consider the quality of the simulated observation is high, and prefer the detection of anomalies in the null hypothesis.

In the OMT, The null hypothesis is rejected, and the cluster-wise MHT is applied to select the optimal model from all alternative models.

Following Section 3.2.4, we estimate the deformation model parameters of all four alternative hypotheses, compute the test ratio $\underline{\mathbf{T}}_j$ based on Eq. (3.43), and select the alternative hypothesis following Eq. (3.44), i.e. the test ratio is larger than 1 and is the largest among all four test ratios.

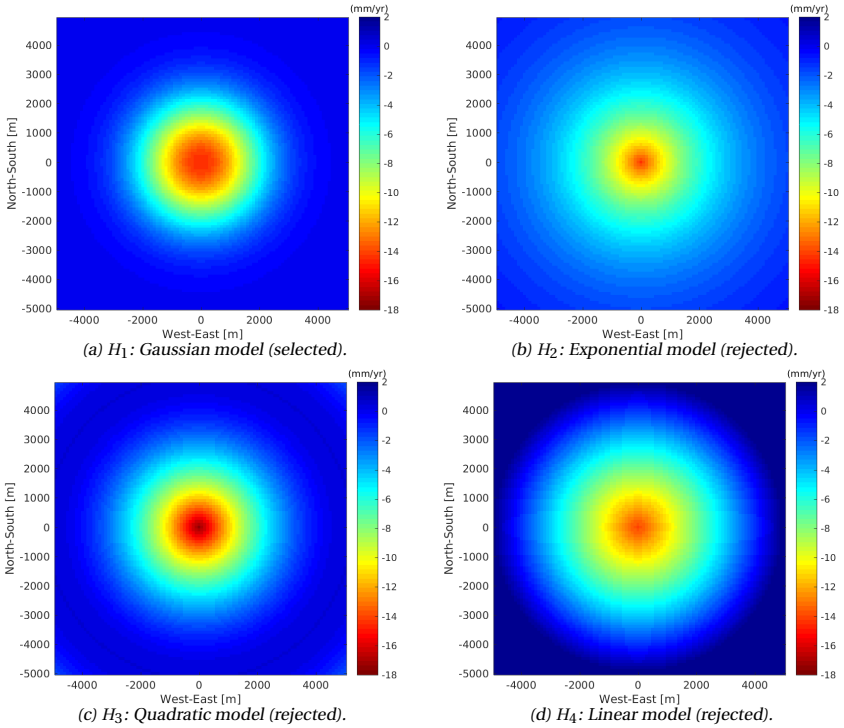

(a) H_1: Gaussian model (selected).

(b) H_2: Exponential model (rejected).

(c) H_3: Quadratic model (rejected).

(d) H_4: Linear model (rejected).

Figure 4.12: The deformation velocity map of the estimated deformation models of the four alternative hypothesis. The alternative hypothesis shown in (a), i.e. the Guassian model is selected as the optimal deformation model.

Table 4.1: The estimated deformation model parameters and the test ratios of the four alternative hypotheses.

Model	Estimated parameters	Test ratio $\mathbf{T}_j$
H_1: Gaussian model (accepted)	$\hat{\underline{v}}_c = -14.5$ mm/yr $\hat{\underline{\kappa}} = -0.7828$ $\hat{\underline{L}}_g = 1884$ m	3.7
H_2: exponential model (rejected)	$\hat{\underline{v}}_c = -14.3$ mm/yr $\hat{\underline{\iota}} = 0.55$ $\hat{\underline{L}} = 1309$ m	2.2
H_3: quadratic (rejected)	$\hat{\underline{a}} = -6.60 \times 10^{-13}$ mm^{-1}yr^{-1} $\hat{\underline{b}} = 6.9 \times 10^{-6}$ yr^{-1} $\hat{\underline{v}}_c = -18.0$ mm/yr	2.9
H_4: linear (rejected)	$\hat{\underline{k}} = 3.3 \times 10^{-6}$ yr^{-1} $\hat{\underline{v}}_c = -14.4$ mm/yr	2.1

The estimated deformation model of all four alternative hypotheses are shown in Fig. 4.12. Table 4.1 lists the values of estimated parameters and the test ratios.

The test ratios of all alternative models are higher than 1, which means that they are all more probable than the null hypothesis H_0.

Fig. 4.13 shows the west-east profiles of the estimated deformation models and the actual deformation signal. The Gaussian model, which is selected as the optimal deformation model, shown in red in the bottom figure of Fig. 4.13. The selected model is the same type of the actual deformation model. However, due to the influence of the noise, the values of model parameters are not the same as the actual deformation model.

In Scenario B, based on given spatial smoothness information, we define the extent of the cluster as well as the alternatives of the deformation model. This contextual information is not as stringent as Scenario A, which assigns a fixed value of the deformation velocity to the entire cluster, Scenario B gives fewer constraints to the deformation model of the cluster, and use the cluster-wise MHT to select the optimal model. When the correct model (Gaussian model) is within the alternative models, the cluster-wise MHT selects it. When this optimal model is not within the alternative models, the cluster-wise MHT will choose the model which fits the observation best.

Based on Scenario A and B of the cluster-wise deformation modeling, it can be concluded that the given spatial smoothness information plays an important role in the cluster-wise deformation modeling, as it defines the extent as well as the deformation model of a cluster. The stringent but unreliable contextual information brings a bias to the results of cluster-wise deformation modeling. The fact is that how to introducing the contextual information into the existed mathematical model is also of importance.

In this chapter, we apply spatio-temporal deformation modeling on simulated InSAR deformation time series. Its performance is assessed by comparing the modeling results with actual simulated deformation, given different types of available contextual information. In Chapter 5, we will apply spatio-temporal deformation modeling on real InSAR data, over the hydrocarbon production area.

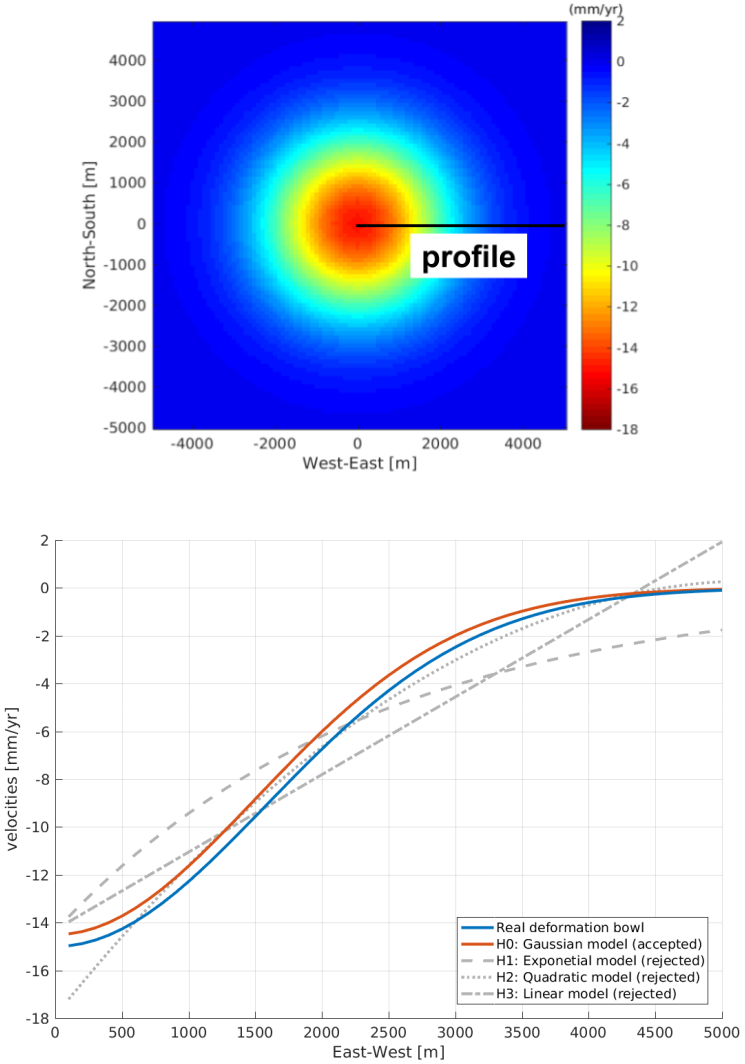

Figure 4.13: The profile of the deformation models of the four alternative hypotheses. The black line in the upper figure shows the range of the profile. In the lower graph, the profile of the actual deformation shows in blue, and the profile of Gaussian model, which is accepted as the optimal model, shows in red. The rejected alternative models show in grey.

5

Application on Real Data: Hydrocarbon Production Region Monitoring

This chapter demonstrates the feasibility of using Spatio-temporal deformation modeling to monitor the deformation in a hydrocarbon production region. We present a case study over the South Belridge hydrocarbon field, California, the USA, where the deformation in the area is found closely related to oil/gas production and steam/water injection activities (Bawden et al., 2003). In this case study, we use spatio-temporal deformation modeling to detect local instantaneous deformation, based on the InSAR deformation time series computed from TerraSAR-X data.

5.1. Introduction of the study area

South Belridge is a large hydrocarbon field in the west San Joaquin Valley, Kern County. It was discovered in 1911, and has more than 12000 active wells at the time of 2015 (DOGGER, 2016). Extraction of large volumes from shallow depths causes reduction in pore pressure and subsequent compaction in this region. Due to the production activities, surface subsidence is found to be a common occurrence in the field (Chase Jr et al., 1989; van der Kooij and Mayer, 2002). The ground surface subsidence may result in damage to civil infrastructure, mostly damage to hydrocarbon production facilities(De Rouffignac et al., 1995; Dale et al., 1996; Fredrich et al., 2000). Monitoring ground surface subsidence is important to manage the hydrocarbon production activities, and avoid geological disasters in this region.

Previous studies have been performed measuring the subsidence in this region using ERS-1 and ERS-2 InSAR observations (van der Kooij, 1997; Fielding et al., 1998). The results of these studies show that the maximum subsidence rates in this region can be more than 400mm/yr, in the period from 1992 to 1996. These results have been validated also by comparing them to GPS observations in this region (van der Kooij and Mayer, 2002).

Apart from the subsidence phenomena in the area, the deformation behavior at South Belridge field can also appear as uplift, due to local injection activities in the purpose of driving the underground hydrocarbon reservoir (Patzek et al., 1992). This uplift

has been observed by InSAR observations (Fielding et al., 1998) as well as GPS and surface tiltmeter observations (Wolhart et al., 2005). The uplift may cause the failures of injection wells. Monitoring the uplift is important to manage the injection activities in this region.

The deformation in this area, including both subsidence and uplift, may also show in the form of instantaneous change (Patzek et al., 1992), i.e. significant deformation may occur over a short time period, due to the sudden change of pore pressure and subsequent compaction.

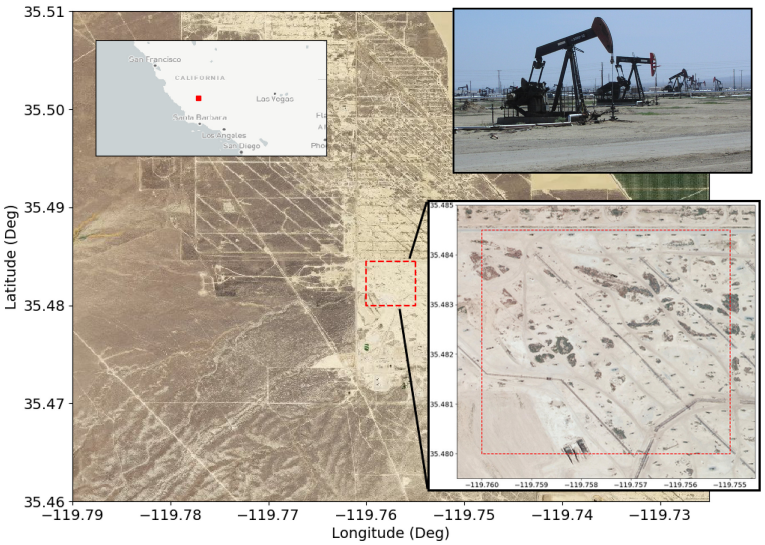

Figure 5.1: An overview of the study area. The area located in the California, USA, which is shown in the upper-left map. The red rectangle dashed indicates the extent of the chosen study area, with an approximate size of 500 × 500 *meters. The overall land cover type of the study area is dessert. The hydrocarbon production infrastructure, e.g. production wells and pipelines are visible in the satellite optical image over the study area.*

Therefore, due to the existence of both uplift and subsidence, and the existence of possible instantaneous deformation, the conventional steady state (constant velocity) model will not be sufficient to describe the deformation behavior of this area. In this study, we choose a hydrocarbon production region with an approximate size of 500 × 500 meters, see Fig. 5.1, and apply the proposed spatio-temporal deformation modeling method as introduced in Chapter 3 to parameterize the deformation behavior in this region.

5.2. Methods

We investigate the deformation behavior in the selected area using InSAR phase observations of coherent scatterers (Ferretti et al., 2000a, 2001) in the area. These phase observations are double-differenced to the same reference epoch and the same reference point. Then the differential deformation obtained by multiplication of the phase differences with the radar wavelength, correcting the for two-way travel of radar pulse (Hanssen, 2001a), see Section 2.1.1. The coherent scatterers in the study area are primarily selected from the targets which have high interferometric coherence. The temporal behavior of these selected coherent scatterers is represented as deformation time series, which is explored to study the deformation behavior of the study region.

5.2.1. Radar interferometry

We use an image stack of 22 TerraSAR-X SAR images, see Table 5.1, which are acquired between March 9, 2016 and November 17, 2016 (Track: 167, ascending track) to generate the interferograms, see Table 5.1. The radar aboard the TerraSAR-X satellite operates in X-band (31 mm wavelength), HH polarization mode.

We use an Equivalent Single Master method (Ferretti et al., 2011; Samiei Esfahany, 2017) to derive the deformation time series of the study area. We manually set the first acquisition of stack, i.e. the acquisition on March 9, 2016, as the reference epoch. We select temporally coherent InSAR measurement points in the study area. For each point, we derive its deformation time series w.r.t the epoch 20160309 and the reference point to represent the deformation of the area of interest.

We identify the temporally coherent points based on the interferometric coherence, which is estimated using a series of adaptive directional windows centered at a given point, over all interferograms, as (Touzi et al., 1999; Hanssen, 2001a)

$$\hat{\gamma}_{\text{intf}} = \left| \frac{\sum_{i=1}^{M}\sum_{j=1}^{N} C_{i,j}^{\text{master}} (C_{i,j}^{\text{slave}})^{*}}{\sqrt{\sum_{i=1}^{M}\sum_{j=1}^{N} C_{i,j}^{\text{master}} (C_{i,j}^{\text{master}})^{*} \; \sum_{i=1}^{M}\sum_{j=1}^{N} C_{i,j}^{\text{slave}} (C_{i,j}^{\text{slave}})^{*}}} \right|, \tag{5.1}$$

where $\hat{\gamma}_{\text{intf}}$ is the estimated interferometric coherence, $C_{i,j}^{\text{master}}$ and $C_{i,j}^{\text{slave}}$ are the complex values of the master and slave images respectively, at a given point and a given interferogram. The superscript {*} is the sign for the complex conjugate. M and N are respectively the number of interferograms and the number of points in the adaptive window.

In Eq. (5.1) we compute the estimated interferometric coherence $\hat{\gamma}_{\text{intf}}$ per interferogram (from 1 to M) and per point in the adaptive window (from 1 to N). It should be noted that not all possible interferograms between all SAR images are computed. For instance, if one interferogram is linearly correlated with other interferograms, it will not be computed. In this study, for each image, we compute 3 interferograms with other images. The computed interferograms should 1) not be linearly correlated with other in-

Table 5.1: Terrasar-X data sets used in this study (Track: 167, ascending track). The temporal baseline B_t and the perpendicular baseline $B_\perp$ are relative to the master image.

Nr.	Acquisition dates	$B_\perp$ [m]	B_t [days]
1	20160309 (master)	0	0
2	20160320	-162.40	11
3	20160331	-111.00	22
4	20160411	-159.20	33
5	20160503	-65.00	55
6	20160514	-122.70	66
7	20160525	-119.90	77
8	20160605	-81.10	88
9	20160616	-46.60	99
10	20160627	-132.50	110
11	20160708	-125.60	121
12	20160719	106.40	132
13	20160730	-40.30	143
14	20160810	-209.30	154
15	20160821	-273.10	165
16	20160901	-146.70	176
17	20160923	-234.80	198
18	20161004	155.10	209
19	20161015	355.00	220
20	20161026	79.50	231
21	20161106	52.80	242
22	20161117	235.60	253

terferograms; 2) have minimum unwrapping errors among all possible interferograms.

In the study of the deformation behavior in South Belridge hydrocarbon field, the instantaneous deformation may significantly reduce the estimated interferometric coherence, and result into underestimating the quality of the InSAR measurements and wrongly rejecting points. To maintain a sufficient number of measurements in the area of interest, we estimated the interferometric coherence value over the time period from March 9, 2016, to August 21, 2016, using in total 15 out of 22 acquisitions. We assume that in this time period, no instantaneous deformation occurs due to the production or injection activity. Then we select points with higher than 0.8 estimated interferometric coherence, and compute the deformation time series for these points. If the above assumption does not hold for an InSAR measurement point, i.e. instantaneous deformation occurs during the mentioned period, the consequence will be the underestimation of the quality and wrongly rejecting this point, but not wrongly including a point with

low quality.

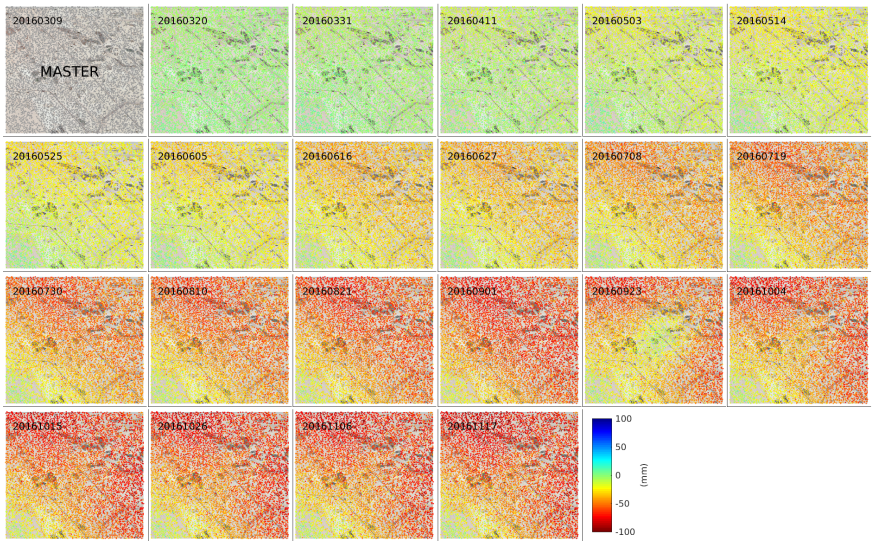

Figure 5.2: The deformation time series of the selected InSAR measurement points of the 500×500 *study area. In total* 6321 *InSAR measurement points have been selected to represent the temporal deformation behavior in the area of interest. All the deformations are double-differenced to the same reference epoch and the reference point. All estimated DEM phase, atmospheric phase and reference point noise are removed.*

After the temporal coherent points are identified, we follow the Equivalent Single Master method (Ferretti et al., 2011; Samiei Esfahany, 2017) to derive InSAR deformation time series of InSAR measurement points in the study area. The topographic phase is removed from the deformation time series based on a 30m resolution DEM (Shuttle Radar Topography Mission, SRTM) (van Zyl, 2001) and the precise orbit data. The atmospheric phase screen is estimated by using an Ordinary Kriging method (Wackernagel, 1995), and is subtracted from the deformation time series. The reference point noise (RPN) is estimated and subtracted from the deformation time series. Then the deformation time series of all temporally coherent points are obtained, see Fig. 5.2, and are explored to study the deformation of the area of interest.

5.2.2. Spatio-temporal deformation modeling

To investigate the deformation behavior in the area of interest, we parameterize the multi-epoch InSAR outputs, i.e. InSAR deformation time series with a deformation model. The conventional way is to model the deformation time series with the constant velocity (steady-state) model, as shown in Fig. 5.3.

Fig. 5.3 shows the deformation velocity map with a constant velocity of every InSAR

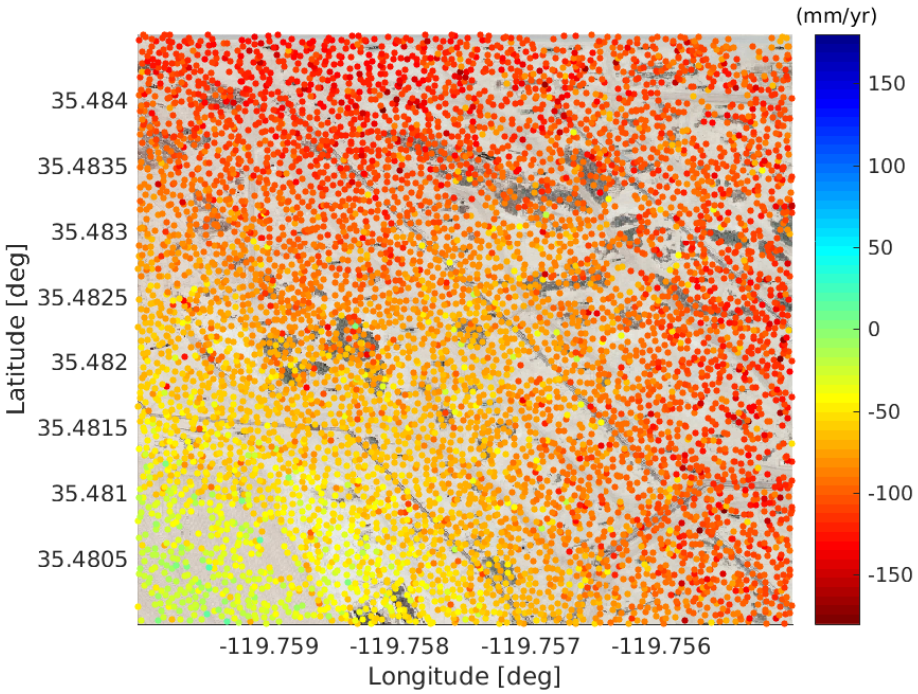

Figure 5.3: Deformation velocity map estimated from the deformation time series of the selected InSAR measurement points. All InSAR measurement points are considered to be independent, and all InSAR observations have the same weight.

measurement point. When the temporal deformation of each InSAR measurement point is a linear function of time, the velocity map can well describe the deformation behavior of the study area. However, this is not the case in the South Belridge hydrocarbon field because instantaneous deformation behavior is reported in this area. Therefore the deformation time series of the InSAR measurement points are unlikely to follow the constant velocity model. In Fig. 5.4, the daisy-chain deformation time series of the study area is presented, in which the deformation time series at each epoch is with reference to the previous epoch. Two significant instantaneous deformation events can be observed: 1) On 23 September 2016, a significant uplift is observed in the overall study area; 2) On 4 October 2016, a sudden subsidence is observed. These instantaneous deformation events can provide important information for the management of hydrocarbon production. Therefore they cannot be parameterized by a constant velocity model.

In order to choose the optimal deformation model to describe the deformation behavior, we apply spatio-temporal deformation modeling as introduced in Chapter 3. We will model the deformation both point-wisely and cluster-wisely to compare their re-

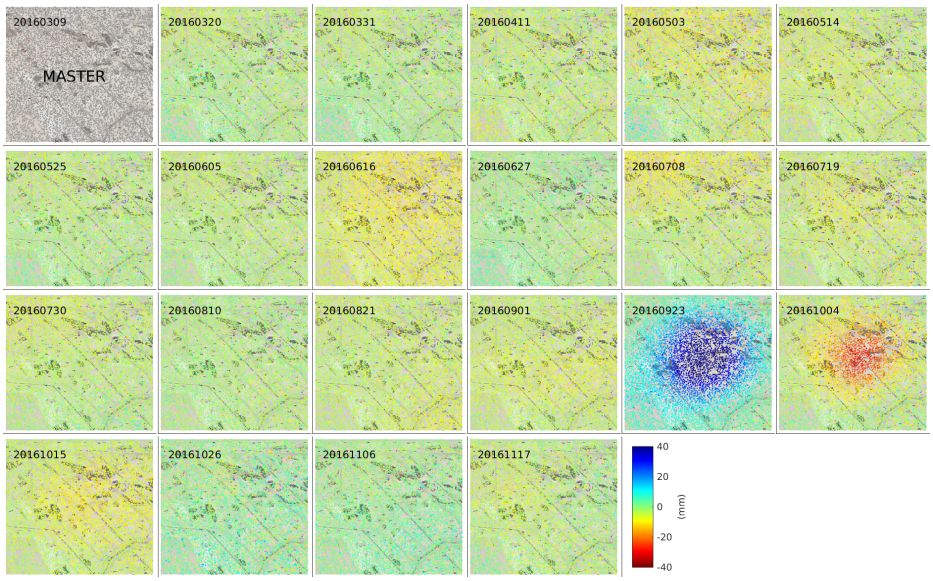

Figure 5.4: Daisy-chain deformation time series of the selected InSAR measurement points over the study area. The deformation time series are w.r.t. the previous epoch. Significant uplift can be observed on 23 September 2016, followed by an instantaneous subsidence on 4 October 2016.

sults.

5.2.3. Point-wise deformation modeling

For a single InSAR measurement point p in the study area, we use the combinations of deformation functions from the canonical function library (Chang and Hanssen, 2016) to model its deformation time series, as introduced in Section 3.1. To optimize the computational efficiency, and considering the deformation signature of interest is an instantaneous change in the temporal deformation behavior, we choose three canonical functions to build up the multiple hypotheses: 1) breakpoint model, 2) step model, 3) outlier model. To optimize the computational efficiency, we limit the maximum number of the breakpoints and the steps to be 3, to avoid testing a model with too many parameters. Considering all possible combinations, if the constant velocity model is rejected, the number of alternative hypotheses can be computed as:

$$N_{\text{model}} = (C_1^{20} + C_2^{20} + C_3^{20})^3 \approx 2.46 \times 10^9, \tag{5.2}$$

where the operator $C_k^a = \frac{a!}{k!(a-k)!}$ computes the number of combinations of choosing k elements from a elements. N_{model} is the number of possible combinations of deformation model.

The selection of the level of significance is related to the cost of making Type-I error: reject the null hypothesis while it is true, i.e. raise a "false alarm". In this study, we are more confident in the default model (steady state model) than the other models, therefore we initiate a relatively small level of significance as $\alpha = 0.02$.

When the null hypothesis is rejected, we follow the B-method of testing to choose the optimal deformation model for each point. For each alternative hypothesis, we stay neutral on whether accepting it or not. Therefore we use the power of test $\gamma = 0.5$.

The results of point-wise deformation modeling will be presented in Section 5.3.

5.2.4. Cluster-wise deformation modeling

We apply cluster-wise deformation modeling to take into account the spatio-temporal correlation between InSAR measurement points.

We define the extents of the clusters following Option 3 among the three options to define the extent of a cluster, as introduced in Section 3.2.1. By this option, we assume that the deformation signal is the dominant component of the InSAR observations, and compute the spatio-temporal variogram of InSAR observations to decide the size of clusters. The experience value of standard deviation of TerraSAR-X InSAR measurements is 3 mm, therefore we apply a predefined variogram threshold of 9 mm^2. Given the predefined threshold of the variogram, the corresponding correlation range $r_{cls} = 17.98$ m can be derived. Then we define the study area into equal sized square grid cells. Each grid is sized as $r_{cls} \times r_{cls}$, as shown in Fig. 5.5b. To utilize all InSAR measurement point in the area of interest, in this study we divide the area of interest into 30×30 equal sized grid cells, with the length of edge 16.67 m. We define each grid cell as a cluster.

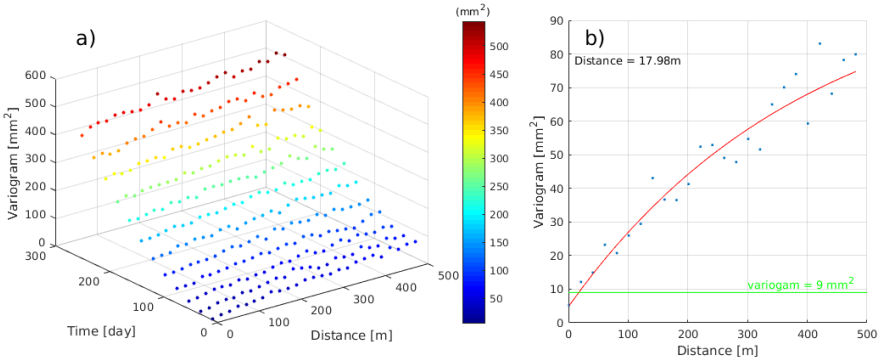

Figure 5.5: a): the spatio-temporal experimental variogram of the deformation time series of all InSAR measurement points locate in the study area. b): the variogram of deformation time series at zero time difference. The red line in the right figure indicates the fitted variogram function with exponential function. The green line indicates the variogram threshold (9 mm^2) we apply for the case study, which corresponds to the distance 17.98 m.

The definition of the deformation model within a cluster follows Option 2 among the two options introduced in Section 3.2.1, i.e. we assume that the deformation time series of each cluster can be described by a linear combination of functions from the canonical function library. Cluster-wise MHT is applied to choose the optimal deformation model. We stick to the level of significance $\alpha = 0.02$ as an initial value and the power of test $\gamma = 0.5$ for cluster-wise MHT, as the same as point-wise MHT.

The results of cluster-wise deformation modeling will be presented in Section 5.3.

5.3. Results and discussions

5.3.1. Point-wise deformation modeling

The hypothesis testing method is applied to select the optimal deformation model of every InSAR measurement point in the study area. For each InSAR measurement point, we first test the constant velocity function as the null hypothesis of the deformation model of the clusters. If the null hypothesis is rejected, we will apply MHT to select the optimal deformation model from the alternative hypotheses. Each alternative hypothesis is formed up by a combination of a breakpoint function, a step function, and an outlier function. For each InSAR measurement point, we assume that the maximum number of steps, breakpoints, and outliers should be 3.

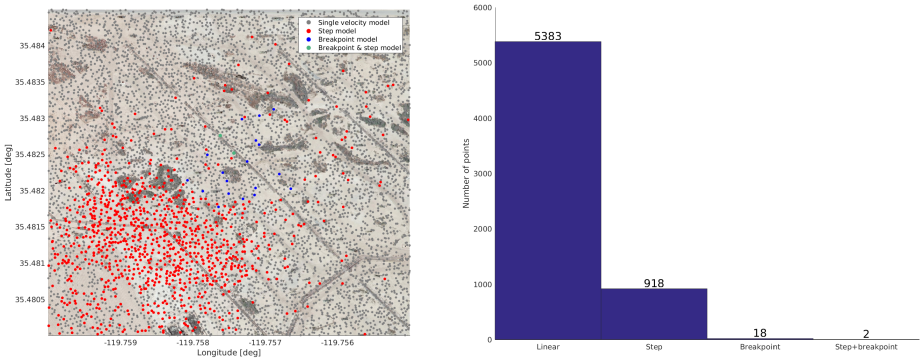

Figure 5.6: Left: the classification map of the deformation model of all InSAR measurement points in the study area. Right: the histogram of the number of point following each model. The constant velocity function is accepted for most of the InSAR measurement points. The step model is selected by point-wise MHT for most of InSAR measurement points which don't follow the linear model. For all InSAR measurement point, the maximum number of the breakpoints or steps in their deformation model is 1.

We classify the InSAR measurement points by their deformation models, as shown in Fig. 5.6. Most of the InSAR measurement points follow the constant velocity model, shown as grey points in Fig. 5.6. Among the points for which the constant velocity points are rejected, MHT selects the step model as the optimal model for many (918) of the

InSAR measurement points. Only 18 points follow the breakpoint model, and 2 points have both a step and a breakpoint in their deformation time series. Note that for all the points which do not follow the constant velocity model, the maximum number of steps and breakpoints is 1, as shown in Eq. (3.26).

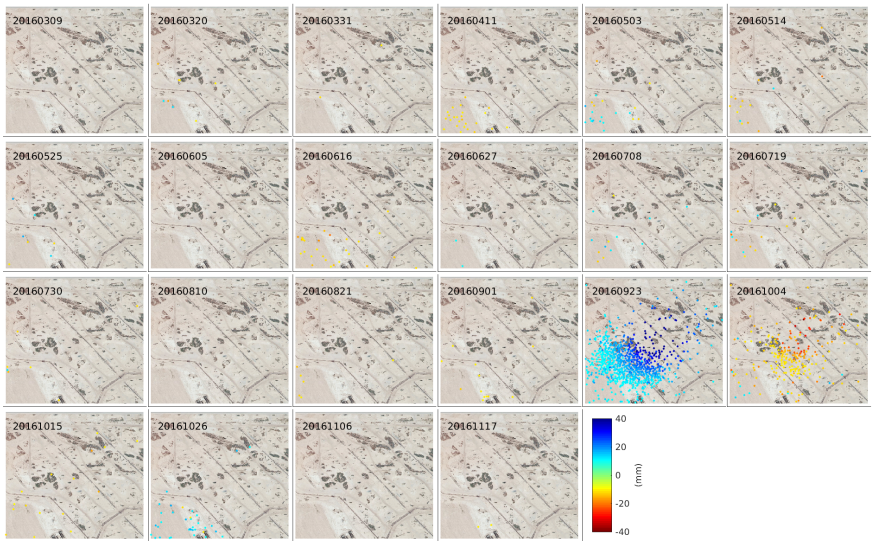

Figure 5.7: The time series of instantaneous deformation (steps) computed by point-wise MHT. Each epoch shows the instantaneous uplift or subsiding relative to the previous epoch. The positive numbers (shown in blue) indicate uplift, while the negative numbers (shown in red/yellow) indicate subsidence. On 23 September, 2016 a significant number of points are tested to have instantaneous uplift, while on 4 October, 2016 many InSAR measurement points show instantaneous subsidence.

Fig. 5.7 shows the step magnitude time series of all InSAR measurement points. Each epoch in the figure shows the magnitude of the step deformation relative to the previous epoch, where the positive numbers (shown in blue) indicate uplift, and the negative numbers (shown in red/yellow) indicate subsidence. The majority of the uplift steps occur on 23 September 2016, while the majority of subsiding occur on 4 October 2016.

Fig. 5.4, shows that on 23 September 2016, the uplift occurs in a round area which covers a large part of the area of interest. On 4 October 2016, a relatively smaller round region shows an instantaneous subsidence. The deformation shows significant spatial patterns on these two epochs. However, as shown in Fig. 5.7, on these two epochs, only the steps at the south-west region is accepted by MHT, for most of the points, the constant velocity model still holds.

In order to assess the performance of point-wise deformation modeling, we will compare the point-wise deformation modeling results with the results of cluster-wise modeling.

5.3.2. Cluster-wise deformation modeling

We divide the area into 30 × 30 equal sized grid cells, and define each grid cell as a cluster. The cluster-wise deformation modeling, as introduced in Section 3.2, is applied to each cluster. We assume the deformation behavior of each cluster can be represented by the combination of functions with steps, breakpoints, and outliers, and apply cluster-wise MHT to select the optimal deformation model for each cluster.

In total 546 out of 900 clusters have at least one step in their deformation time series, as a result of cluster-wise MHT. Fig. 5.8 shows the classification map of the deformation models of all clusters. The number of steps in the cluster ranges from 0 to 3 in the cluster. The maximum number of breakpoints is 1.

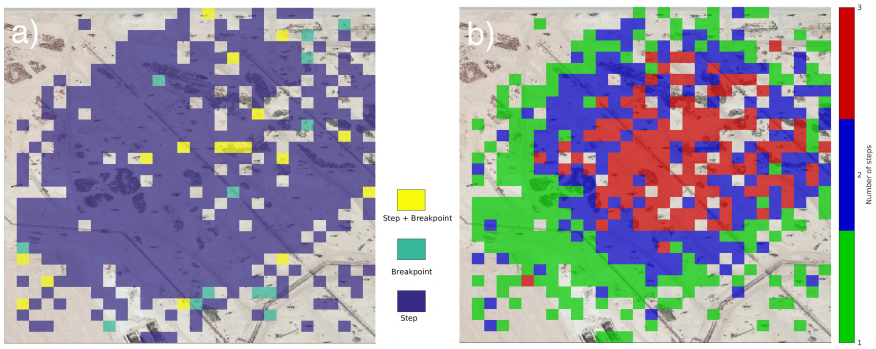

Figure 5.8: a): classification map of the deformation models of all clusters. b): the number of steps of each cluster. The number of steps of each cluster ranges from 1 to 3. The maximum number of breakpoints is 1. Clusters following the null hypothesis, i.e. the constant velocity model, are transparent in the two figures.

In Fig. 5.9 we show the step time series of all 900 clusters in the area of interest, where each epoch shows the magnitude of steps w.r.t. the previous epoch.

As shown in Fig. 5.9, 503 out of 900 clusters show an instantaneous uplift on 23 September 2016. On both 4 October 2016 and 15 October 2016, the number of clusters showing instantaneous subsiding are 306 out of 900 and 196 out of 900 respectively.

We select three typical clusters to illustrate the performance of cluster-wise deformation modeling, as shown in 5.10. The InSAR measurement points in all three clusters show similar temporal deformation behavior. Cluster 1 has a single-step deformation model, cluster 2 has a three-step and one-breakpoint deformation model. Cluster 3 has a two-step deformation model. The parameters of the deformation models of the three clusters are shown in table 5.2. In the cluster-wise deformation modeling, if the null hypothesis is rejected, the cluster-wise MHT is able to assign more than one steps to a cluster. For instance, the selected optimal functional model of Cluster 2 has three steps and one breakpoint, and has a good fit to the InSAR measurements

In Section 5.3.4, we will compare the difference between the results of point-wise modeling and cluster-wise deformation modeling, and assess their performance.

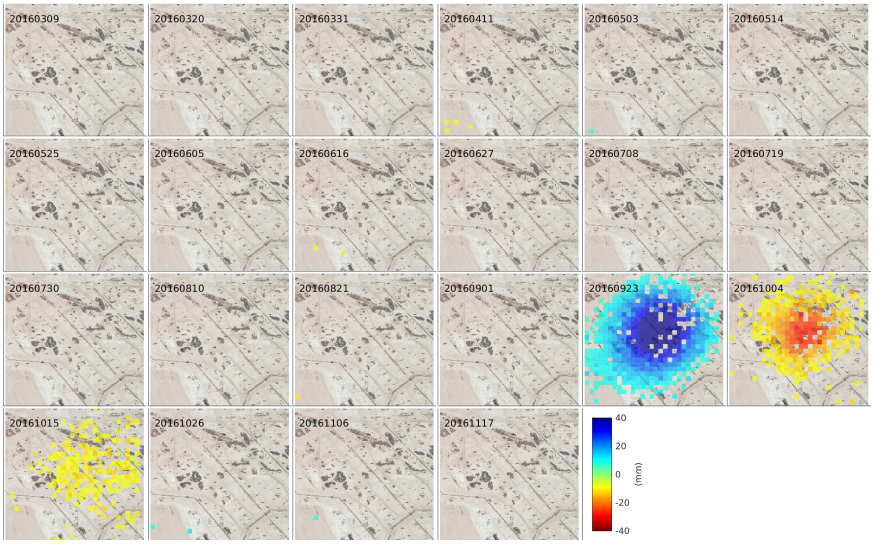

Figure 5.9: The time series of instantaneous deformation (steps) computed by cluster-wise MHT. The deformation time series of 900 clusters are modeled. Each epoch shows the magnitude of instantaneous uplift or subsiding relative to the previous epoch. The positive numbers (shown in blue) indicate uplift, and the negative numbers (shown in red/yellow) indicate subsidence.

Table 5.2: Deformation model parameters of the three selected clusters. The positions and the deformation time series of these clusters are shown in Fig. 5.10. The non-applicable parameters are indicated as "-".

Deformation model parameters	Cluster 1	Cluster 2	Cluster 3
Deformation velocity v [mm/yr]	−73.7	−141.6	−112.5
Step on 20160923 s_{0923} [mm]	14	50	37
Step on 20161004 s_{1004} [mm]	-	−20	−14
Step on 20161015 s_{1015} [mm]	-	−5	-
Velocity change on 20161015 δv_{1015} [mm/yr]	-	104.2	-

5.3.3. Quality control

The stochastic model in point-wise deformation modeling and cluster-wise deformation modeling is built up following the instructions of Section 3.1.2 and Section 3.2.3. Based

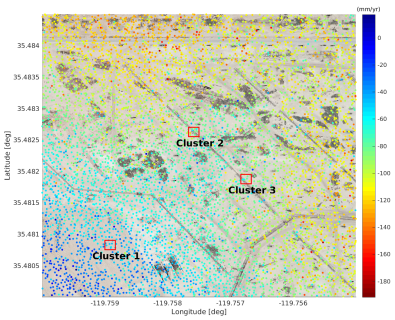

(a) Location of three clusters.

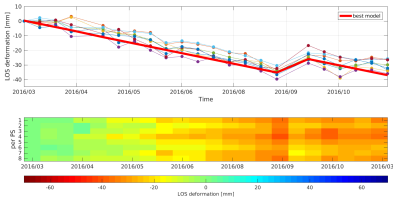

(b) Cluster 1. Single step model.

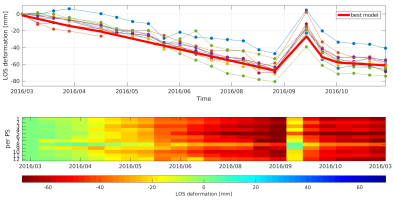

(c) Cluster 2. Two-step and one-breakpoint model.

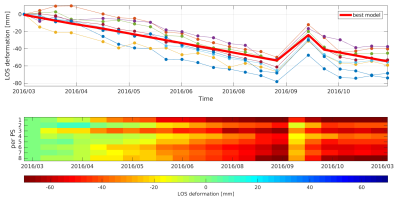

(d) Cluster 3. Two-step model.

Figure 5.10: Deformation time series of three typical clusters. (a): the location of the three clusters, with the velocity map Fig. 5.3 as base map. (b), (c) and (d): the deformation time series of Cluster 1, Cluster 2 and Cluster 3 respectively. The red solid line in Fig. (b), (c) and (d) indicates the posteriori deformation time series of the chosen optimal deformation model. The lower images in (b), (c) and (d) show temporal evolutions of the points in each cluster. The InSAR measurement points in the same cluster show similar temporal deformation behavior.

on error propagation law, we estimate the variance-covariance matrix of the deformation model parameters computed from point-wise deformation modeling and cluster-wise deformation modeling respectively, as an indicator of precision. The estimation of the precision follows Section 3.3. Fig. 5.11 shows the variance of three types of deformation parameters estimated using both point-wise deformation modeling and cluster-wise modeling method, for every point/cluster, if applicable: 1) deformation velocity; 2) step on epoch September 23, 2016; 3) step on epoch October 4, 2016.

In Section 5.3.4, we compare the precision of point-wise deformation modeling results and cluster-wise modeling results.

5.3.4. Discussion

The deformation time series of the InSAR measurement points are modeled by the point-wise deformation modeling method and the cluster-wise deformation modeling method. We compare the differences between the results from the two methods from the following aspects:

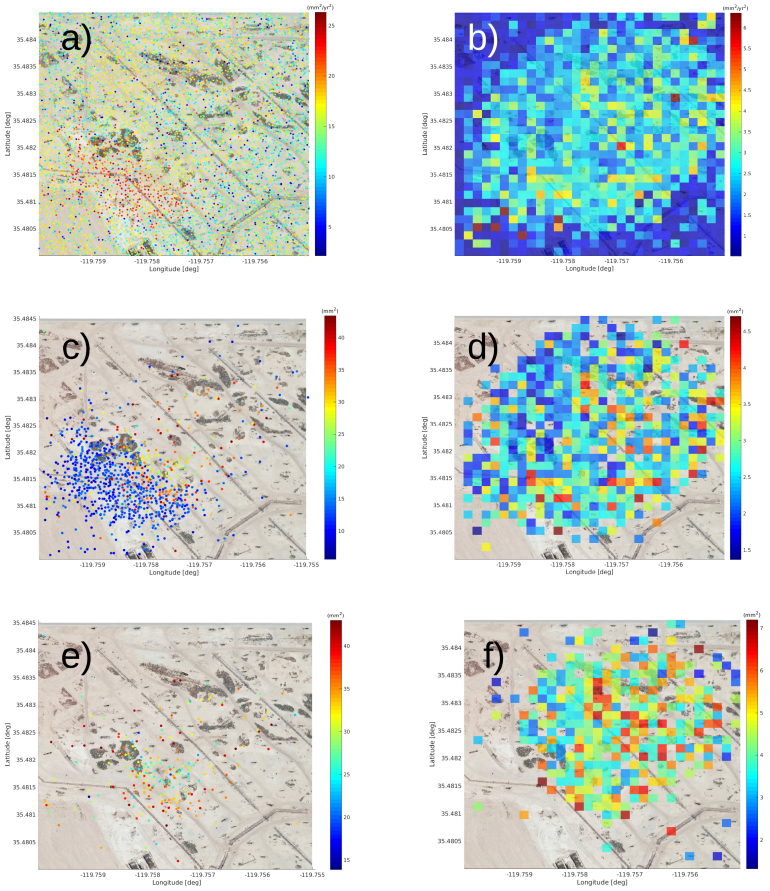

Figure 5.11: The variances of the estimated deformation model parameters. Fig. a), c) and e) are the variances of point-wise deformation modeling results. Fig. b), d) and f) are the variances of cluster-wise modeling results. a): variances of the deformation velocity of each InSAR measurement point. b): variances of deformation velocity of each cluster. c): variances of each InSAR measurement point, which has step on September 23, 2016. d): variances of each cluster, which has step on September 23, 2016. e): variances of each InSAR measurement point, which has step on October 4, 2016. f): variances of each cluster, which has step on October 4, 2016.

- **The correlation between the deformation time series of spatial close InSAR measurement points.** Based on apriori knowledge, the InSAR measurement points in the area of interest are assumed to share the same deformation driving mechanism, i.e. due to the shallow compaction caused by hydrocarbon production ac-

tivity. By definition, the cluster-wise modeling taking into account this contextual information by modeling the deformation per clusters rather than per point, and therefore its results shows more spatial consistency. If the apriori information is correct, i.e. the real deformation signal has spatial correlation due to the same driving mechanism in this area, then the point-wise deformation results will not be physically realistic, because point-wise deformation modeling does not take into account the spatial correlation information.

- **The dimension of deformation model.** The point-wise deformation modeling results contain no more than 1 step and 1 breakpoint, in the deformation model of each InSAR measurement point. On the other hand, the cluster-wise deformation modeling is able to model the deformation time series of a cluster using a deformation model with multiple steps. This is due to the property of the B-method of testing, which chooses the model with less parameter but fits the observations equally well. The point-wise deformation modeling use less observations than cluster-wise deformation modeling. Therefore, under the same level of significance and power of the test, point-wise modeling will tend to choose a model with fewer parameters, than having a good fit to the data. This prevents the modeling results from over-fitting the measurements. While in cluster-wise deformation modeling, more observations are taken into account, the misfit to the data will be more significant in the modeling. In this situation, a model with more parameters may be accepted.

- **The resolution of the output.** Point-wise modeling results describe the deformation behavior of the area of interest using the deformation time series of 6321 InSAR measurement points. The cluster-wise modeling divides the area of interest into 900 grid cells, and use the deformation grid cells to describe the deformation behavior of the area of interest, assuming the deformation behavior in each cluster can be represented by the same model. Therefore the cluster-wise deformation modeling sacrifices the resolution of the results for a more physically realistic result.

The case study on South Belridge hydrocarbon filed shows that, comparing to point-wise deformation modeling, the cluster-wise modeling is able to take into account the contextual information on the spatial correlation of deformation signal. Given the correct contextual information, InSAR measurement point can be grouped into clusters, and within each cluster on assuming all points follow the same deformation model. One can use the deformation models of clusters to represent the deformation of the area of interest. The advantage of the cluster-wise deformation modeling is that under the same level of significance and the power of test, based on the correct contextual information on spatial correlation, the deformation model of each cluster can have more parameters

than the deformation model of a single point, and modeling results show better spatial consistency, by definition of cluster-wise modeling. This is at the cost of resolution, i.e. by applying cluster-wise modeling, the InSAR observations of all InSAR measurement points within a same cluster will be used as the observations of the cluster. This may result in losing details describing the deformation behavior.

6

Conclusions and Recommendations

6.1. Conclusions

The main objective of this study is to develop and demonstrate methodologies to detect spatio-temporal patterns/changes in InSAR deformation time series. The key is to properly integrate the external knowledge, especially on spatial smoothness, into InSAR time series mathematical models. Hereby, the study focuses on the main research question:

How to optimally digest spatial smoothness information of the presumed deformation signal in the mathematical model, to estimate the spatio-temporal deformation of InSAR measurements points, and assess the quality of the results?

The estimation of the spatio-temporal deformation relies on the apriori information on the spatial smoothness of the deformation signal. The information presumes the similarities in the deformation behavior between adjacent InSAR measurement points. Based on it, one can extend the deformation modeling from a point-wise process to a cluster-wise process. The spatial smoothness information is a contextual information, which can come from two external sources, see Section 3.2.1, 1) *expert knowledge or experience* or, 2) *extra observations*. We developed methodologies based on spatial smoothness information to construct/improve the functional model and stochastic model of spatial-temporal deformation modeling.

The main research question is subdivided into three specific research questions, which we will discuss subsequently.

1. *What is the optimal functional model and stochastic model?*
   We define the "optimal model" as the best model which can be derived based on given InSAR observations and apriori knowledge. We derive the optimal functional model and stochastic model in two ways. 1) By default, we apply point-wise deformation modeling to every InSAR measurement point, and determine its most probable deformation model based on multiple hypothesis testing (MHT) and the B-method of testing, see Section 3.1. 2) When knowledge on the spatial smoothness of deformation is available, we apply cluster-wise deformation modeling, which groups a number of spatially correlated InSAR measurement points into a so-called "cluster" based on the given spatial smoothness information, see

Section 3.2. This method assumes that all points in the cluster have identical deformation models, i.e. they follow the same deformation model. The deformation model parameters of the cluster are estimated based on the deformation time series of all InSAR measurement points within the cluster.

The point-wise deformation modeling follows Chang et al. (2014); Chang and Hanssen (2016). The optimal functional model per point is selected using the MHT method, see Sections 3.1.1 and 3.1.3. The steady-state (constant velocity) function is used as the null hypothesis. If the null hypothesis is rejected, the optimal functional model will be chosen from the combinations of canonical deformation models (Chang and Hanssen, 2016), by applying MHT per point. We consider two major error sources in the InSAR measurements: the atmospheric noise and the scattering noise, and build up the stochastic model, see Section 3.1.2. The temporal correlation of noise, mainly due to the sharing of the same reference epoch, is taken into account in the stochastic model. Yet, the spatial correlation of the neighboring points have not been introduced into the functional and stochastic model, which makes it hard to detect the spatial patterns straightforwardly.

The application of cluster-wise deformation modeling are introduced in Section 3.2. Based on given knowledge on the spatial smoothness of deformation, the extend and thr deformation model of a cluster is defined see Sections 3.2.1 and 3.2.2. When multiple possible functional models exist, the cluster-wise MHT is applied to select the optimal model for the cluster. We built up the stochastic model in a similar way as point-wise modeling, i.e. we take into account the atmospheric noise and the scattering noise, but considering the spatial correlation of noise, see Section 3.2.3. Benefit from the cluster-wise deformation modeling, the spatio-temporal deformation patterns can be directly detected.

Note that both in point-wise and cluster-wise modeling, the selected "optimal" functional model is the optimal model from all pre-defined models. These pre-defined models stem either from the library of canonical functions (Chang and Hanssen, 2016) or from other contextual information, e.g. given alternative spatio-temporal deformation models of a deformation bowl, as in Section 4.3.2. This means if the actual optimal functional model is not pre-defined in the null and alternative hypotheses, it cannot be selected during the modeling process.

2. *How to digest spatial smoothness information?*
Spatial smoothness information is digested by importing it into the functional/stochastic model. Since it can be given by two sources, we proposed two ways to digest it respectively, listed below:

   - **Cluster-wise deformation modeling**. Spatial smoothness information from *the expert knowledge* or *experience* are introduced to conduct the cluster-wise

deformation modeling, see Section 3.2.1. We propose to define the extent and the deformation model of a cluster based on given spatial smoothness information. Introducing this contextual information results in affecting the structure of the design matrix A and the vector of unknown parameters x in the functional model.

The cluster-wise deformation modeling offers the possibility to import the external spatial smoothness information into the deformation modeling. This external information can describe the correlations between InSAR measurement points, and help to improve the functional model to describe the deformation in the area of interest.

- **Introducing pseudo observations**. The spatial smoothness information provided by *extra observations* can be integrated by treating them as *pseudo observations* of deformation modeling, i.e. it provides the pseudo observation $\underline{d}$ and its stochastic model Q_{dd}, see Eqs. (2.18) and (2.19) in Section 2.2.2. In Section 4.3.1, we demonstrate this approach by a simulation where the presumed velocities of the four rings of a deformation bowl are given. The given presumed velocities are treated as pseudo observations, and integrated into the deformation modeling. Therefore, introducing pseudo observations provides the possibility to integrate the extra observations in to deformation modeling, which is an improvement on both functional and stochastic model.

In the two ways, spatial smoothness information are digested and introduced to the spatio-temporal modeling, by importing them into the functional/stochastic model. Given correct spatial smoothness information, the precision and the reliability of the deformation modeling will be improved.

3. *How to assess the quality of the results?*
The quality of the spatio-temporal deformation modeling results are assessed from two aspects: 1) the misfitting of the model to the InSAR observations, and 2) the imperfection of deformation model itself. The former is related to the noise in the observations, and is represented by the *precision* of the estimated parameters. The latter is related to the misspecification of the deformation model parameters, which can be represented by the *reliability*.

   We introduced the Variance-covariance matrix (VCM) of the estimated parameters as a metric of the precision, see Section 3.3.1. The VCM can be computed using error propagation based on the apriori VCM of the observations.

   The misspecification of the model parameters is closely related to the choice of the deformation model. We introduced the *Minimal Detectable Value* (MDV) as a

metric of the reliability, see Section 3.3.2. The MDV is computed to a specific alternative hypothesis. Therefore MDV varies in terms of different degrees of freedom for alternative hypotheses. It should also be noted that the MHT is applied based on a predefined level of significance α and a power of test γ. The choice of α and γ are usually based on the cost of making Type-I and the detectability power of any alternative hypothesis, which is different between cases. The different choice of α and γ will also influence the value of MDV.

6.2. Contributions

The main contributions of this study are summarized as follows,

- We design and implement a spatio-temporal (cluster-wise) deformation modeling methodology to parameterize the InSAR deformation time series, based on multiple hypothesis testing (MHT) and B-method of testing in both temporal and spatial domain.
- We introduce a work flow to introduce apriori spatial smoothness information into InSAR time series mathematical model, by importing the apriori information into the functional/stochastic model of spatio-temporal deformation modeling.
- We demonstrate a methodology to apply the spatio-temporal deformation modeling on the deformation monitoring caused by hydrocarbon production activities, and assessed its performance.
- We detect the spatial uplifting and subsiding patterns over the hydrocarbon production area.

6.3. Recommendations

We propose four recommendations for further research,

- **Considering the temporal filtering effect in the stochastic model.** In this study, we constructed the stochastic model taking into account scattering noise and atmospheric noise. However, based on the assumption that the atmospheric noise is temporal uncorrelated (Hanssen, 2001a), it is common to apply a temporal low-pass filter to InSAR deformation time series during TInSAR processing (van Leijen, 2014; Samiei Esfahany, 2017), to mitigate atmospheric noise. The effect of this temporal filtering of InSAR deformation time series is ignored during the construction of the stochastic model. The temporal filtering may result in increasing temporal correlation between epochs (Hanssen, 2001a; Samiei Esfahany, 2017), and may also bring bias. When the temporal filtering is applied, this correlation is required to be introduced into the stochastic model.

- **Adding spatial parameters into the canonical deformation models.** The deformation model of the cluster is either directly given based on contextual information, or chosen from the combination from the canonical function library proposed by Chang and Hanssen (2016). However, this library only presents the functions for a single InSAR measurement point, therefore when selecting a deformation model for a cluster from this library, we should make the assumption that the deformation of the cluster does not vary spatially. This assumption may not hold in case a cluster covering a large area. On the other hand, we consider that the spatial deformation patterns, e.g. deformation bowls, can also be written into the combinations of several canonical functions. In future research, the possibility of building up such a library needs to be investigated.

- **Improving the computation efficiency.** When selecting the optimal deformation model from the library of canonical functions, the possible combinations for an InSAR measurement point or a cluster can increase exponentially as the dimension (i.e. the number of unknown parameters) of deformation model increase. As a result, the total amount of the models can easily reach to an enormous number. For example, for an InSAR deformation time series with 50 epochs, if it is assumed that only 1 breakpoint exists in the time series, the possible number of deformation models is 48 (considering the breakpoint does not occur on the first and the last epoch). If we assume two breakpoints and one step exist, the number of possible models will dramatically increase to: $(48 \times 47/2) \times 48 = 54114$. A smarter testing strategy is required to improve the computation efficiency.

- **Developing a quality metric for the contextual information.** The contextual information on the spatial smoothness of deformation signal plays an important role in the spatio-temporal deformation modeling. The quality of pseudo observations are specified by the VCM Q_{dd}. However, the contextual information given by *expert knowledge or experience* is applied based on the assumption that they are correct. A formal metric to asses the quality of contextual information is needed for selecting the input contextual information. The development of this metric requires further study.

Bibliography

Abidin, H. Z., Djaja, R., Andreas, H., Gamal, M., Hirose, K., Maruyama, Y., and Subarya, C. (2005). Land subsidence in Jakarta (Indonesia) as detected by leveling, GPS survey and InSAR techniques. In Agen, Z., Shiliang, G., Carbognin, L., and Johnson, A. I., editors, *Proceedings of the Seventh International Symposium on Land Subsidence (SISOLS 2005), Shanghai, China, 23-28 October 2005, IAHS Publication No. XXX*, volume 2, pages 469–479. Shanghai Scientific & Technical Publishers.

Adam, N., Kampes, B. M., Eineder, M., Worawattanamateekul, J., and Kircher, M. (2003). The development of a scientific permanent scatterer system. In *ISPRS Workshop High Resolution Mapping from Space, Hannover, Germany, 2003*, page 6 pp.

Amelung, F., Galloway, D. L., Bell, J. W., Zebker, H. A., and Laczniak, R. J. (1999). Sensing the ups and downs of Las Vegas: InSAR reveals structural control of land subsidence and aquifer-system deformation. *Geology*, 27(6):483–486.

Baarda, W. (1968). *A testing procedure for use in geodetic networks*, volume 5 of *Publications on Geodesy*. Netherlands Geodetic Commission, Delft, second edition.

Bamler, R. and Hartl, P. (1998). Synthetic aperture radar interferometry. *Inverse problems*, 14(4):R1–54.

Bamler, R. and Schättler, B. (1993). SAR data acquisition and image formation. In Schreier, G., editor, *SAR Geocoding: data and systems*, pages 53–102. Wichmann Verlag, Karlsruhe.

Bawden, G. W., Sneed, M., Stork, S. V., and Galloway, D. L. (2003). Measuring human-induced land subsidence from space. Technical report.

Bell, J. W., Amelung, F., Ferretti, A., Bianchi, M., and Novali, F. (2008). Permanent scatterer insar reveals seasonal and long-term aquifer-system response to groundwater pumping and artificial recharge. *Water Resources Research*, 44(2).

Berardino, P., Casu, F., Fornaro, G., Lanari, R., Manunta, M., Manzo, M., and Sansosti, E. (2004). A quantitative analysis of the SBAS algorithm performance. *International Geoscience and Remote Sensing Symposium, Anchorage, Alaska, 20–24 September 2004*, pages 3321–3324.

Berardino, P., Fornaro, G., Lanari, R., and Sansosti, E. (2002). A new algorithm for surface deformation monitoring based on small baseline differential SAR interferograms. *IEEE Transactions on Geoscience and Remote Sensing*, 40(11):2375–2383.

Brown, R. J. E. and Kupsch, W. O. (1974). *Permafrost terminology*. Number 111. National Research Council of Canada Associate Committee on Geotechnical Research. Ottawa.

Caro Cuenca, M. (2012). *Improving radar interferometry for monitoring fault-related surface deformation: Applications for the Roer valley graben and coal mine induced displacements in the southern Netherlands*. Number 81. Netherlands Geodetic Commission.

Caro Cuenca, M., Hooper, A. J., and Hanssen, R. F. (2013). Surface deformation induced by water influx in the abandoned coal mines in Limburg, the Netherlands observed by satellite radar interferometry. *Journal of Applied Geophysics*, 88:1–11.

Chang, L. (2015). *Monitoring civil infrastructure using satellite radar interferometry*. TU Delft, Delft University of Technology.

Chang, L., Dollevoet, R., and Hanssen, R. (2014). Railway infrastructure monitoring using satellite radar data. *International Journal of Railway Technology*, volume 3.

Chang, L. and Hanssen, R. (2015). Detection of permafrost sensitivity of the Qinghai–Tibet Railway using satellite radar interferometry. *International Journal of Remote Sensing*, 36(3):691–700.

Chang, L. and Hanssen, R. F. (2016). A probabilistic approach for insar time-series postprocessing. *IEEE transactions on geoscience and remote sensing*, 54(1):421–430.

Chase Jr, C., Dietrich, J., et al. (1989). Compaction within the south belridge diatomite. *SPE Reservoir Engineering*, 4(04):422–428.

Chen, F., Lin, H., Li, Z., Chen, Q., and Zhou, J. (2012). Interaction between permafrost and infrastructure along the Qinghai–Tibet Railway detected via jointly analysis of C-and L-band small baseline SAR interferometry. *Remote Sensing of Environment*, 123:532–540.

Cuenca, M. C., Hooper, A. J., and Hanssen, R. F. (2011). A new method for temporal phase unwrapping of persistent scatterers insar time series. *IEEE Transactions on Geoscience and Remote Sensing*, 49(11):4606–4615.

Cumming, I. and Wong, F. (2005). *Digital Processing Of Synthetic Aperture Radar Data: Algorithms And Implementation*. Artech House Publishers, New York. ISBN 1580530583.

Dale, B., Narahara, G., Stevens, R., et al. (1996). A case history of reservoir subsidence and wellbore damage management in the south belridge diatomite field. In *SPE Western Regional Meeting*. Society of Petroleum Engineers.

De Rouffignac, E., Bondor, P., Karanikas, J., Hara, S., et al. (1995). Subsidence and well failure in the south belridge diatomite field. In *SPE Western Regional Meeting*. Society of Petroleum Engineers.

Ding, X., Li, Z., Zhu, J., Feng, G., and Long, J. (2008). Atmospheric effects on insar measurements and their mitigation. *Sensors*, 8(9):5426–5448.

Dixon, T. H., Amelung, F., Ferretti, A., Novali, F., Rocca, F., Dokka, R., Sella, G., Kim, S.-W., Wdowinski, S., and Whitman, D. (2006). Space geodesy: Subsidence and flooding in New Orleans. *Nature*, 441:587–588.

DOGGER (2016). 2015 annual report of the state oil and gas supervisor. Technical report.

Emardson, T., Simons, M., and Webb, F. (2003). Neutral atmospheric delay in interferometric synthetic aperture radar applications: Statistical description and mitigation. *Journal of Geophysical Research*, 108(B5):2231.

Ferretti, A., Fumagalli, A., Novali, F., Prati, C., Rocca, F., and Rucci, A. (2011). A new algorithm for processing interferometric data-stacks: SqueeSAR. *IEEE Transactions on Geoscience and Remote Sensing*, 49(9):3460–3470.

Ferretti, A., Prati, C., and Rocca, F. (1999a). Multibaseline InSAR DEM reconstruction: The wavelet approach. *IEEE Transactions on Geoscience and Remote Sensing*, 37(2):705–715.

Ferretti, A., Prati, C., and Rocca, F. (1999b). Non-uniform motion monitoring using the permanent scatterers technique. In *Second International Workshop on ERS SAR Interferometry, 'FRINGE99', Liège, Belgium, 10–12 Nov 1999*, pages 1–6. ESA.

Ferretti, A., Prati, C., and Rocca, F. (2000a). Measuring subsidence with SAR interferometry: Applications of the permanent scatterers technique. In Carbognin, L., Gambolati, G., and Johnson, A. I., editors, *Land subsidence; Proceedings of the Sixth International Symposium on Land Subsidence*, volume 2, pages 67–79. CNR.

Ferretti, A., Prati, C., and Rocca, F. (2000b). Nonlinear subsidence rate estimation using permanent scatterers in differential SAR interferometry. *IEEE Transactions on Geoscience and Remote Sensing*, 38(5):2202–2212.

Ferretti, A., Prati, C., and Rocca, F. (2000c). Process for radar measurements of the movement of city areas and landsliding zones. International Application Published under the Patent Cooperation Treaty (PCT).

Ferretti, A., Prati, C., and Rocca, F. (2001). Permanent scatterers in SAR interferometry. *IEEE Transactions on Geoscience and Remote Sensing*, 39(1):8–20.

Ferretti, A., Savio, G., Barzaghi, R., Borghi, A., Musazzi, S., Novali, F., Prati, C., and Rocca, F. (2007). Submillimeter accuracy of InSAR time series: Experimental validation. *IEEE Transactions on Geoscience and Remote Sensing*, 45(5):1142–1153.

Fielding, E. J., Blom, R. G., and Goldstein, R. M. (1998). Rapid subsidence over oil fields measured by sar interferometry. *Geophysical Research Letters*, 25(17):3215–3218.

Fredrich, J. T., Arguello, J., Deitrick, G., De Rouffignac, E., et al. (2000). Geomechanical modeling of reservoir compaction, surface subsidence, and casing damage at the belridge diatomite field. *SPE Reservoir Evaluation & Engineering*, 3(04):348–359.

Gauss, C. F. (1809). *Theoria motus corporum coelestium in sectionibus conicis solem ambientium auctore Carolo Friderico Gauss*. sumtibus Frid. Perthes et IH Besser.

Glaser, P., Chanton, J., Morin, P., Rosenberry, D., Siegel, D., Ruud, O., Chasar, L., and Reeve, A. S. (2004). Surface deformations as indicators of deep ebullition fluxes in a large northern peatland. *Global Biogeochemical Cycles*, 18(1).

Goldstein, R. (1995). Atmospheric limitations to repeat-track radar interferometry. *Geophysical Research Letters*, 22(18):2517–2520.

Goldstein, R. M., Engelhardt, H., Kamp, B., and Frolich, R. M. (1993). Satellite radar interferometry for monitoring ice sheet motion: Application to an antarctic ice stream. *Science*, 262:1525–1530.

Goldstein, R. M., Zebker, H. A., and Werner, C. L. (1988). Satellite radar interferometry: Two-dimensional phase unwrapping. *Radio Science*, 23(4):713–720.

Gray, L., Mattar, K., and Short, N. (1999). Speckle tracking for 2-dimensional ice motion studies in polar regions: Influence of the ionosphere. In *Second International Workshop on ERS SAR Interferometry, 'FRINGE99', Liège, Belgium, 10–12 Nov 1999*, pages 1–8. ESA.

Hanssen, R. F. (2001a). *Radar Interferometry: Data Interpretation and Error Analysis*. Kluwer Academic Publishers, Dordrecht.

Hanssen, R. F. (2001b). *Radar interferometry: data interpretation and error analysis*, volume 2. Springer Science & Business Media.

Hanssen, R. F. and Klees, R. (1998). Applications of SAR interferometry in terrestrial and atmospheric mapping. In Ligthart, L. P., editor, *Workshop proceedings European Microwave Conference, Amsterdam, 9 October*, pages 43–50. European Microwave Conference, Miller Freeman.

Hanssen, R. F., van Leijen, F. J., van Zwieten, G. J., Dortland, S., Bremmer, C. N., and Kleuskens, M. (2008). Validation of PSI results of Alkmaar and Amsterdam within the Terrafirma validation experiment. In *Fifth International Workshop on ERS/Envisat SAR Interferometry, 'FRINGE07', Frascati, Italy, 26 Nov-30 Nov 2007*, page 6 pp.

Hooper, A. (2006). *Persistent Scatterer Radar Interferometry for Crustal Deformation Studies and Modeling of Volcanic Deformation.* PhD thesis, Stanford University.

Hooper, A. (2008). A multi-temporal InSAR method incorporating both persistent scatterer and small baseline approaches. *Geophysical Research Letters*, 35(16).

Hooper, A., Segall, P., and Zebker, H. (2007). Persistent scatterer interferometric synthetic aperture radar for crustal deformation analysis, with application to Volcán Alcedo, Galápagos. *Journal of Geophysical Research*, 112(B7):B07407.

Hooper, A., Zebker, H., Segall, P., and Kampes, B. (2004). A new method for measuring deformation on volcanoes and other non-urban areas using InSAR persistent scatterers. *Geophysical Research Letters*, 31:L23611, doi:10.1029/2004GL021737.

Jefferys, W. H. and Berger, J. O. (1992). Ockham's razor and Bayesian analysis. *American Scientist*, pages 64–72.

Kampes, B. (2005). *Displacement parameter estimation using permanent scatterer interferometry*. Forschungsbericht. DLR, Bibliotheks- und Informationswesen.

Kampes, B. and Usai, S. (1999). Doris: the Delft Object-oriented Radar Interferometric Software. In *2nd International Symposium on Operationalization of Remote Sensing, Enschede, The Netherlands, 16–20 August, 1999*.

Kampes, B. M. and Adam, N. (2004). Deformation parameter inversion using permanent scatterers in interferogram time series. In *European Conference on Synthetic Aperture Radar, Ulm, Germany, 25–27 May 2004*, pages 341–344.

Kampes, B. M. and Adam, N. (2006). The STUN algorithm for persistent scatterer interferometry. In *Fourth International Workshop on ERS/Envisat SAR Interferometry, 'FRINGE05', Frascati, Italy, 28 Nov-2 Dec 2005*.

Kampes, B. M. and Hanssen, R. F. (2004). Ambiguity resolution for permanent scatterer interferometry. *IEEE Transactions on Geoscience and Remote Sensing*, 42(11):2446–2453.

Kaplan, W. (1952). *Advanced calculus*, volume 4. Addison-Wesley Reading, MA.

Ketelaar, G., van Leijen, F., Marinkovic, P., and Hanssen, R. (2007). Multi-track PS-InSAR fusion. In *ESA ENVISAT Symposium, Montreux, Switzerland, 23–27 April 2007*, page Submitted xxx pp.

Ketelaar, V. B. H. (2009). *Satellite radar interferometry: Subsidence monitoring techniques*, volume 14. Springer Science & Business Media.

Krige, D. G. (1951). A statistical approach to some basic mine valuation problems on the witwatersrand. *Journal of the Southern African Institute of Mining and Metallurgy*, 52(6):119–139.

Lanari, R., Berardino, P., Bonano, M., Casu, F., Manconi, A., Manunta, M., Manzo, M., Pepe, A., Pepe, S., Sansosti, E., et al. (2010). Surface displacements associated with the L'Aquila 2009 Mw 6.3 earthquake (central Italy): New evidence from SBAS-DInSAR time series analysis. *Geophysical Research Letters*, 37(20).

Lanari, R., Mora, O., Manunta, M., Mallorquí, J. J., Berardino, P., and Sansosti, U. (2004). A small-baseline approach for investigating deformations on full-resolution differential SAR interferograms. *IEEE Transactions on Geoscience and Remote Sensing*, 42(7):1377–1386.

Lee, J. S., Hoppel, K. W., Mango, S. A., and Miller, A. R. (1994). Intensity and phase statistics of multilook polarimetric and interferometric sar imagery. *IEEE Transactions on Geoscience and Remote Sensing*, 30:1017.

Liu, S. (2012). *Satellite radar Interferometry: estimation of atmospheric delay*. PhD thesis, Delft University of Technology.

Lyons, S. and Sandwell, D. (2002). Fault creep along the southern San Andreas from InSAR, permanent scatterers, and stacking. *Journal of Geophysical Research*, 108(B1):24 pp.

Marinkovic, P., Ketelaar, G., van Leijen, F., and Hanssen, R. (2008). InSAR quality control: Analysis of five years of corner reflector time series. In *Fifth International Workshop on ERS/Envisat SAR Interferometry, 'FRINGE07', Frascati, Italy, 26 Nov-30 Nov 2007*, page 8 pp.

Markoff, A. A. (1912). Wahrscheinlichkeitsrechnung.

Massonnet, D. (1994). Validation of ERS-1 interferometry at CNES. In *Second ERS-1 Symposium—Space at the Service of our Environment, Hamburg, Germany, 11–14 October 1993*, ESA SP-361, pages 703–709.

Massonnet, D. and Feigl, K. L. (1998). Radar interferometry and its application to changes in the earth's surface. *Reviews of Geophysics*, 36(4):441–500.

Massonnet, D., Rossi, M., Carmona, C., Adagna, F., Peltzer, G., Feigl, K., and Rabaute, T. (1993). The displacement field of the Landers earthquake mapped by radar interferometry. *Nature*, 364(8):138–142.

Massonnet, D. and Souyris, J.-C. (2008). *Imaging with synthetic aperture radar*. CRC Press.

Montgomery, D. R., Sullivan, K., and Greenberg, H. M. (1998). Regional test of a model for shallow landsliding. *Hydrological Processes*, 12(6):943–955.

Mora, O., Mallorqui, J. J., and Broquetas, A. (2003). Linear and nonlinear terrain deformation maps from a reduced set of interferometric SAR images. *IEEE Transactions on Geoscience and Remote Sensing*, 41(10):2243–2253.

Odijk, D., Kenselaar, F., and Hanssen, R. (2003). Integration of leveling and InSAR data for land subsidence monitoring. In 11^{th} *FIG International Symposium on Deformation Measurements, Santorini, Greece, 23–28 May, 2003*, pages cdrom, p.8.

Papoutsis, I., Papanikolaou, X., Floyd, M., Ji, K., Kontoes, C., Paradissis, D., and Zacharis, V. (2013). Mapping inflation at santorini volcano, greece, using gps and insar. *Geophysical Research Letters*, 40(2):267–272.

Patzek, T. et al. (1992). Surveillance of south belridge diatomite. In *SPE Western Regional Meeting*. Society of Petroleum Engineers.

Poland, M., Bürgmann, R., Dzurisin, D., Lisowski, M., Masterlark, T., Owen, S., and Fink, J. (2006). Constraints on the mechanism of long-term, steady subsidence at medicine lake volcano, northern california, from gps, leveling, and insar. *Journal of Volcanology and Geothermal Research*, 150(1):55–78.

Rott, H., Schechl, B., Siegel, A., and Grasemann, B. (1999). Monitoring very slow slope movements by means of SAR interferometry: A case study from a mass waste above a reservoir in the ötztal Alps, Austria. *Geophysical Research Letters*, 26(11):1629–1632.

Samiei Esfahany, S. (2017). Exploitation of distributed scatterers in synthetic aperture radar interferometry.

Samiei-Esfahany, S. and Hanssen, R. F. (2013). New algorithm for insar stack phase triangulation using integer least squares estimation. In *Geoscience and Remote Sensing Symposium (IGARSS), 2013 IEEE International*, pages 884–887. IEEE.

Sandwell, D., Mellors, R., Tong, X., Wei, M., and Wessel, P. (2011). Open radar interferometry software for mapping surface deformation. *Eos, Transactions American Geophysical Union*, 92(28):234–234.

Sandwell, D. T. and Price, E. J. (1998). Phase gradient approach to stacking interferograms. *Journal of Geophysical Research*, 103(B12):30183–30204.

Savage, J., Svarc, J., and Prescott, W. (2003). Near-field postseismic deformation associated with the 1992 Landers and 1999 Hector Mine, California, earthquakes. *Journal of Geophysical Research: Solid Earth (1978–2012)*, 108(B9).

Sinclair, W. C. (1982). *Sinkhole development resulting from ground-water withdrawal in the Tampa area, Florida*. US Geological Survey, Water Resources Division.

Tarantola, A. (2005). *Inverse problem theory and methods for model parameter estimation*. siam.

Taylor, B. (1717). *Methodus incrementorum directa & inversa*. Inny.

Teunissen, P. (1998). Minimal detectable biases of gps data. *Journal of Geodesy*, 72(4):236–244.

Teunissen, P. J. G. (1989). Estimation in nonlinear models. In *II Hotine-Marussi Symposium on Mathematical Geodesy, Pisa, Italy, June 5–8 1989*.

Teunissen, P. J. G. (1990). An integrity and quality control procedure for use in multi sensor integration. In *ION-GPS Annual Meeting, Colorado Springs, 19–21 Sep 1990*, pages 513–522.

Teunissen, P. J. G. (2000a). *Adjustment theory; an introduction*. Delft University Press, Delft, 1 edition.

Teunissen, P. J. G. (2000b). *Testing theory; an introduction*. Delft University Press, Delft, first edition.

Teunissen, P. J. G. (2003a). A carrier phase ambiguity estimator with easy to evaluate fail-rate. *Artificial Satellites*, 38(3):89–96.

Teunissen, P. J. G. (2003b). Integer aperture GNSS ambiguity resolution. *Artificial Satellites*, 38(3):79–88.

Teunissen, P. J. G. (2006). On InSAR ambiguity resolution for deformation monitoring. *Artificial Satellites*, 41(1):17–22.

Teunissen, P. J. G., Simons, D. G., and Tiberius, C. C. J. M. (2005). *Probability and observation theory*. Delft Institute of Earth Observation and Space Systems (DEOS), Delft University of Technology, The Netherlands.

Tikhonov, A. N. (1963). Regularization of incorrectly posed problems. SOVIET MATHEMATICS DOKLADY.

Tikhonov, A. N., Arsenin, V. I., and John, F. (1977). *Solutions of ill-posed problems*, volume 14. Winston Washington, DC.

Touzi, R., Lopes, A., Bruniquel, J., and Vachon, P. W. (1999). Coherence estimation for SAR imagery. *IEEE Transactions on Geoscience and Remote Sensing*, 37(1):135–149.

Usai, S. (1997). The use of man-made features for long time scale insar. In *International Geoscience and Remote Sensing Symposium, Singapore, 3–8 Aug 1997*, pages 1542–1544.

Usai, S. and Hanssen, R. (1997). Long time scale INSAR by means of high coherence features. In *Third ERS Symposium—Space at the Service of our Environment, Florence, Italy, 17–21 March 1997*, pages 225–228.

Usai, S., Sansosti, E., Tampellini, L., Borgstrom, S., Ricciardi, G., Spaans, J., Pepe, A., Guarino, S., Maddalena, V., van Persie, M., Berardino, P., Lanari, R., Fornaro, G., and Seifer, F. M. (2003). MINERVA: an INSAR monitoring system for volcanic hazard. *International Geoscience and Remote Sensing Symposium, Toulouse, France, 21–25 July 2003*, pages 2433–2436.

van der Kooij, M. (1997). Land subsidence measurements at the belridge oil fields from ers insar data (int). In *Third ERS Symposium on Space at the service of our Environment*, volume 414, page 1853.

van der Kooij, M. and Mayer, D. (2002). The application of satellite radar interferometry to subsidence monitoring in the belridge and lost hills fields, california. In *Geoscience and Remote Sensing Symposium, 2002. IGARSS'02. 2002 IEEE International*, volume 1, pages 201–202. IEEE.

van Leijen, F. J. (2014). *Persistent Scatterer Interferometry based on geodetic estimation theory*. Number 86. Netherlands Geodetic Commission.

van Leijen, F. J. and Hanssen, R. F. (2008). Ground water management and its consequences in Delft, the Netherlands as observed by persistent scatterer interferometry. 9e Nederlands Aardwetenschappelijk Congres 18-19 March, 2008, Veldhoven.

van Zyl, J. J. (2001). The Shuttle Radar Topography Mission (SRTM): a breakthrough in remote sensing of topography. *Acta Astronautica*, 48(5):559–565.

Vasco, D., Rucci, A., Ferretti, A., Novali, F., Bissell, R., Ringrose, P., Mathieson, A., and Wright, I. (2010). Satellite-based measurements of surface deformation reveal fluid flow associated with the geological storage of carbon dioxide. *Geophysical Research Letters*, 37(3).

Verruijt, A. and Van Baars, S. (2007). *Soil mechanics*. VSSD.

Wackernagel, H. (1995). *Multivariate Geostatistics: An Introduction with Applications*. Springer-Verlag, Berlin.

Weisstein, E. W. (2008). Heaviside step function. *From MathWorld–A Wolfram Web Resource. http://mathworld. wolfram. com/HeavisideStepFunction. html*.

Wolhart, S., Davis, E., Roadarmel, W., and Wright, C. (2005). Reservoir deformation monitoring to enhance reservoir characterization and management. In *SEG Technical Program Expanded Abstracts 2005*, pages 2512–2515. Society of Exploration Geophysicists.

Wright, T., Parsons, B., and Fielding, E. (2001). Measurement of interseismic strain accumulation across the North Anatolian Fault by satellite radar interferometry. *Geophysical Research Letters*, 28(10):2117–2120.

Wu, Q., Liu, Y., Zhang, J., and Tong, C. (2002). A review of recent frozen soil engineering in permafrost regions along Qinghai-Tibet Highway, China. *Permafrost and Periglacial Processes*, 13(3):199–205.

Yerkes, R. and Castle, R. (1969). Surface deformation associated with oil and gas field operations in the united states. *Land subsidence*, 1:55–64.

Zebker, H. A. and Goldstein, R. M. (1986). Topographic mapping from interferometric synthetic aperture radar observations. *Journal of Geophysical Research*, 91(B5):4993–4999.

Zebker, H. A., Rosen, P. A., and Hensley, S. (1997). Atmospheric effects in interferometric synthetic aperture radar surface deformation and topographic maps. *Journal of Geophysical Research*, 102(B4):7547–7563.

Zebker, H. A. and Villasenor, J. (1992). Decorrelation in interferometric radar echoes. *IEEE Transactions on Geoscience and Remote Sensing*, 30(5):950–959.

Zeni, G., Bonano, M., Casu, F., Manunta, M., Manzo, M., Marsella, M., Pepe, A., and Lanari, R. (2011). Long-term deformation analysis of historical buildings through the advanced SBAS-DInSAR technique: the case study of the city of rome, italy. *Journal of Geophysics and Engineering*, 8(3):S1.